Structural and geochemical ore-forming processes in deformed gold deposits: towards a multi-scale and -method approach

Julien Perret, Anne-Sylvie André-Mayer, Aurélien Eglinger, Julien Feneyrol, Alexandre Voinot, Christophe Morlot, Fabrice Barou, Yoram Teitler, Diego Seira, Rémi Bosc

Structural and geochemical ore-forming processes in deformed gold deposits: towards a multiscale and -method approach

Julien Perret[1,2,*], Anne-Sylvie André-Mayer[2], Aurélien Eglinger[2], Julien Feneyrol[1], Alexandre Voinot[3,4], Christophe Morlot[2], Fabrice Barou[3], Yoram Teitler[2], Diego Seira[2], Rémi Bosc[1]

Published in "*Recent Advances in Understanding Gold Deposits: From Orogeny to Alluvium*", *Geological Society of London Special Publication, SP516,* https://doi.org/ 10.1144/SP516-2021-37.

[1] Arethuse Geology EURL, BP 80017, Latitude Arbois, 1060 rue René Descartes, 13290 Les Milles, France

[2] GeoRessources, Université de Lorraine, CNRS, 54000 Nancy, France

[3] Department of Geological Sciences and Geological Engineering, Queen's University, K7L 3N6 Kingston, Canada

[4] MacDonald Institute, Canadian Particle Astrophysics Research Centre, Stirling Hall, Department of Physics, Engineering Physics & Astronomy, Queen's University, 64 Bader lane, Kingston, ON, Canada

[5] Géosciences Montpellier, Université de Montpellier, CNRS, 34000 Montpellier, France

Abstract

Integrating structural control on mineralisation and geochemical ore-forming processes is crucial when studying deformed ore deposits. Yet, structural and geochemical data are rarely acquired at the same scale: structural control on mineralisation is typically investigated from the district to the deposit and macroscopic scales whereas geochemical ore processes are described at the microscopic scale. The deciphering of a deformation-mineralisation history valid at every scale thus remains challenging.

This study proposes a multiscale approach that enables the reconciliation of structural and geochemical information collected at every scale, applied to the example of the Galat Sufar South gold deposit, Nubian shield, northeastern Sudan. It gathers field and laboratory information by coupling a classical petrological-structural study with high-resolution X-ray computed tomography, electron back-scattered diffraction and laser ablation inductively-coupled plasma mass spectrometry on mineralised sulphide mineral assemblages.

This approach demonstrates that there is a linear control on mineralisation expressed from the district to microscopic scales at the Galat Sufar South gold deposit. We highlight the relationships between Atmur-Delgo suturing tectonics, micro-deformation of sulphide minerals, syn-pyrite recrystallisation metal remobilisation, gold liberation and ore upgrading. Our contribution therefore represents another step forward a holistic field-to-laboratory approach for the study of any other sulphide-bearing, structurally controlled ore deposit type.

1. Introduction

There is extensive literature on the role of deformation in the onset of hydrothermal mineralising fluid systems (e.g. McCaffrey et al., 1999; Cox et al., 2001; Richards and Tosdal, 2001; Chauvet, 2019; Blenkinsop et al., 2020a, 2020b; Rowland and Rhys, 2020), which is particularly well characterised for deformed lode gold or gold-bearing vein deposits such as orogenic gold (e.g. Sibson, 1990, 2001, 2020a, 2020b; Ridley, 1993; Robert and Poulsen, 2001; Faleiros et al., 2007; Weatherley and Henley, 2013; Peterson and Mavrogenes, 2014; Cox, 2016). In addition, numerous microstructural, geochemical and thermodynamic studies provide information on deformation-assisted geochemical processes leading to gold mineralisation in structurally controlled gold deposits at the microscopic scale (e.g. Tomkins and Mavrogenes, 2001; Weatherley and Henley, 2013; Fougerouse et al., 2016a; Finch and Tomkins, 2017; Petrella et al., 2020a, b; Gaboury and Oré Sanchez, 2020; Voisey et al., 2020). Sulphide minerals, most commonly pyrite and arsenopyrite, can host a variable amount of the gold stock in such deposits, either as free gold inclusions or fracture infilling, nano-inclusions and invisible-refractory gold structurally bound in the sulphide lattice or segregated along crystal defects during sulphide plastic deformation (e.g. Cook and Chryssoulis, 1990; Reich et al., 2005; Hough et al., 2011; Deditius et al., 2014; Pokrovski et al., 2019; Fougerouse et al., 2021). In a given deposit, sulphide mineral texture and geochemical signature may thus indicate gold input and crystallisation-remobilisation stages (e.g. Velasquez et al., 2014; Fougerouse et al., 2017; Pearce et al., 2018; Gourcerol et al., 2018a, 2018b, 2020; Kontak et al., 2018; Large and Maslennikov, 2020; Combes et al., 2021) and could be used as pathfinders for high-grade gold ore (e.g. Kadel-Harder et al., 2020).

However, the scale of investigation required typically differs when it comes to structural control on mineralisation or geochemical mineralisation processes. On one hand, structural control on mineralisation is documented from the district (tens to a hundred km) to the deposit (<1 km), outcrop (up to tens of m) and hand sample (up to

tens of cm) scales, relying on field observations, structural measurements and conventional petrological-structural description of mineralised structures (e.g. Allibone et al., 2002, 2018; Ashley and Craw, 2004; Blenkinsop and Doyle, 2014; Masurel et al., 2017; Yang et al., 2018; Hronsky, 2020; Combes et al., 2021). These field-based data can be further processed by geostatistical and modelling techniques (e.g. Monteiro et al., 2004; Upton and Craw, 2014; Cowan, 2020). Zooming in structural data at the microscopic scale remains however difficult, as loss of information can occur when switching from 3D view of outcrops and drill cores to 2D view of sample slabs and thin sections, even in oriented samples.

On the other hand, the statistical analysis of extensive whole rock geochemical and lithological datasets provide knowledge about elemental mobility induced by alteration and mineralisation processes which is of strong interest for ore targeting at the deposit to macroscopic scales (e.g. Gaillard et al., 2020; Meng et al., 2020). When zooming at the microscopic scale, unravelling geochemical ore processes requires the study of the micro-textural evolution of ore-bearing mineral assemblages together with their *in situ* geochemical signature (e.g. Reich et al., 2017; Román et al., 2019). Analytical techniques such as laser ablation inductively-coupled plasma mass spectrometry (LA-ICP-MS) enable the *in situ* measurement down to a few µm-scale of minor and trace element concentrations in ore-related minerals, in relationship with micro-textural observations (e.g. Román et al., 2019). This approach has been widely used to study sulphide trace element geochemistry within individual deposits (e.g. Large et al., 2007, 2009; Cook et al., 2013; Hazarika et al., 2013; Velasquez et al., 2014; Gourcerol et al., 2018a, 2018b, 2020; Augustin and Gaboury, 2019; Li et al., 2019; Wu et al., 2019a; Kadel-Harder et al., 2020; Combes et al., 2021). When coupled to the microstructural and -textural characterisation of ore-bearing mineral assemblages, such geochemical datasets allow to reassess ore genetic models (e.g. Velasquez et al., 2014; Gourcerol et al., 2018a, 2020; Pearce et al., 2018) and integrate micro-deformation-induced geochemical ore-forming

processes into the deposit- and district-scale deformation history (e.g. Dubosq et al., 2018; Sayab et al., 2020).

In support of conventional field and microscopy work, the analysis of microstructures and/or mineral geochemistry *via* laboratory analytical techniques is therefore critical to the understanding of orebodies as it offers information on structural-geochemical ore relationships (Pearce et al., 2018). Through the example of the Galat Sufar South (GSS) gold deposit, northeastern Sudan, we show how the coupling of a classical field- and microscopy-based petrological-structural approach to laboratory 3D micro-imagery (high-resolution X-ray computed tomography, HRXCT), microstructural analysis (electron back-scattered diffraction, EBSD) and *in situ* geochemical investigation of the gold-bearing sulphide assemblage (laser ablation inductively-couple plasma mass spectrometry on pyrite, LA-ICP-MS) helps (i) zooming in structural control on mineralisation from the district and deposit-scales to the microscopic scale and (ii) bringing knowledge about deformation-induced geochemical gold mineralisation processes.

2. Current insights from HRXCT, EBSD and LA-ICP-MS into ore geology

Pearce et al. (2018) reviewed principles and applications of numerous laboratory techniques, including HRXCT, EBSD and LA-ICP-MS used in this study, enabling the micro-characterisation of metallic ore systems from the tens of cm- to the nm-scales. As the reader may consult the latter reference for further information, this section briefly reviews the insights of these three techniques into geoscience and more especially into ore geology.

2.1. High-resolution X-ray computed tomography

HRXCT uses 3D volume reconstruction and further geometrical analysis to provide information useful for (i) petrophysical characterisation of rocks (e.g. Galkin et al., 2015 and references therein), (ii) magmatic or metamorphic petrofabric studies (e.g. Sayab et al., 2015; Kahl et al., 2017), (iii) fluid and melt inclusion petrography, volumetric and thermodynamic conditions reconstruction (e.g. Richard et al., 2019), (iv) unravelling deformation mechanics (e.g. Thiele et al., 2015), (v) morphological characterisation of fossils (e.g. Vasseur et al., 2019), (vi) gemmology (e.g. Morlot et al., 2016), and (vii) planetary science (e.g. Hanna and Ketcham, 2017). Regarding ore geology, HRXCT and other tomography or X-ray methods (e.g. 3D neutron tomography, integrated absorption, diffraction and fluorescence tomography, X-ray microscopy) are mostly used for (i) ore processing optimisation (e.g. Miller et al., 2003; Dhawan et al., 2012), (ii) qualitative and quantitative characterisation of ore texture and grain distribution (e.g. Kyle and Ketcham, 2003; Godel et al., 2010; Godel, 2013; Chisambi et al., 2020), (iii) ore mineral grain shape and texture characterisation (Sayab et al., 2016; Prichard et al., 2018; Suuronen and Sayab, 2018; Masson et al., 2020; Spinks et al., 2021a), (iv) the study of mineral growth mechanisms (e.g. Prichard et al., 2018; Y. Yao et al., 2020), (v) unravelling ore-forming processes (e.g. Godel et al., 2013; Kyle and Ketcham, 2015; Voisey et al., 2020) and zooming out microscopic-scale structural control on ore formation to the regional scale (e.g. Sayab et al., 2020).

2.2. Electron back-scattered diffraction

Up to now, EBSD has mostly been used in geoscience for (i) rock deformation processes and kinematics characterisation (e.g. Bukovská et al., 2016; Cavalcante et al., 2018; Goswami et al., 2018), (ii) seismic implications (Vonlanthen et al., 2006), (iii) magmatic (e.g. Žák et al., 2008) or metamorphic (e.g. Rehman et al., 2016) process unravelling, (iv) experimental microstructural studies (e.g. Piazolo et al., 2004), and (v) characterising synthetic or natural mineral grain-scale deformation and transformation

mechanism (e.g. Rosière et al., 2001; Barrie et al., 2010a; Wallis et al., 2019; X. Yao et al., 2020). When it comes to ore geology, EBSD is mostly used for (i) the crystallographic characterisation of ore minerals (e.g. Halfpenny et al., 2013; Grimshaw et al., 2017), (ii) the textural investigation of the ore and integration to the regional metamorphism-deformation history (e.g. Boyle et al., 2004; Barrie et al., 2010b; Sayab et al., 2020) as well as (iii) the study of ore formation and remobilisation processes related to micro-deformation (e.g. Kolb et al., 2003; Mateen et al., 2013; Reddy and Hough, 2013; Rosière et al., 2013; Vukmanovic et al., 2013; Fougerouse et al., 2016a; Dubosq et al., 2018; Cugerone et al., 2020; Spinks et al., 2021b).

2.3. Laser ablation inductively-coupled plasma mass spectrometry

In situ analytical methods, such as electron microprobe (EMPA), SIMS, nanoSIMS or LA-ICP-MS, allow to couple major, minor and trace element geochemistry of sulphide minerals with their textural evolution at the µm-scale (Reich et al., 2017; Fougerouse et al., 2016b, 2021; Román et al., 2019). Recent advances in atom probe tomography even enable the study of mineral geochemistry at the sub-nanometric atomic scale (e.g. Fougerouse et al., 2016c, 2021; Gamal El Dien et al., 2019; Wu et al., 2019b; Reddy et al., 2020).

The study of trace element signatures in sulphide minerals (e.g. pyrite, sphalerite and chalcopyrite) *via* LA-ICP-MS is widely used to (i) characterise sulphide-bearing deposit types (e.g. Ye et al., 2011; Winderbaum et al., 2012; Belissont et al., 2014; Belousov et al., 2016; Frenzel et al., 2016), (ii) track temporal changes in ore hydrothermal systems (e.g. Huston et al., 1995; Maslennikov et al., 2009; Wohlgemuth-Ueberwasser et al., 2015; Bonnet et al., 2016; Gill et al., 2016; Soltani Dehnavi et al., 2018; Wang et al., 2017) and (iii) better constrain element precipitation models leading to ore formation (e.g. Butler and Nesbitt, 1999; George et al., 2018). The geochemical signature of pyrite in gold deposits is commonly used to track its thermodynamic

stability, characterise boiling associated with fault rupture events, as well as the partitioning of gold and other metals and metalloids in evolving, sulphur-rich, hydrothermal systems (e.g. Reich et al., 2005; Deditius et al., 2009, 2014; Keith et al., 2016, 2018; Finch and Tomkins, 2017; Tardani et al., 2017; Pokrovski et al., 2019; Román et al., 2019; Wu et al., 2019b; Xing et al., 2019). The microscopic scale investigation of trace elements in pyrite also documents the crystal growth mechanisms, e.g. kinetics, the source(s) of ore-forming fluids (e.g. Augustin and Gaboury, 2019; Voute et al., 2019; Adam et al., 2020), and its potential contribution as a gold source (e.g. Large et al., 2007, 2011). The trace element signature of sulphide minerals may also record syn-metamorphic metal remobilisation (e.g. Morey et al., 2008; Dakota Conn et al., 2019).

3. Case study: the Galat Sufar South gold deposit, northeastern Sudan

Our study focuses on the Galat Sufar South (GSS) gold deposit, northeastern Sudan, owned by Orca Gold Inc. (indicated resources of 75.6 Mt @ 1.27 g/t Au for a total of 3.08 Moz Au with a 0.6 g/t Au cut-off; Duckworth, 2018). GSS is a polyphase, sulphide-dominated, vein-type gold deposit. Mineralisation expression and relationships with deformation events have already been well-constrained from the tens of km-scale to the µm-scale by satellite imagery analysis, field and conventional microscopy work (Perret et al., 2020). Samples of interest analysed in this study have been collected along several diamond drill cores within the East Zone of the GSS gold deposit (Fig. 1b).

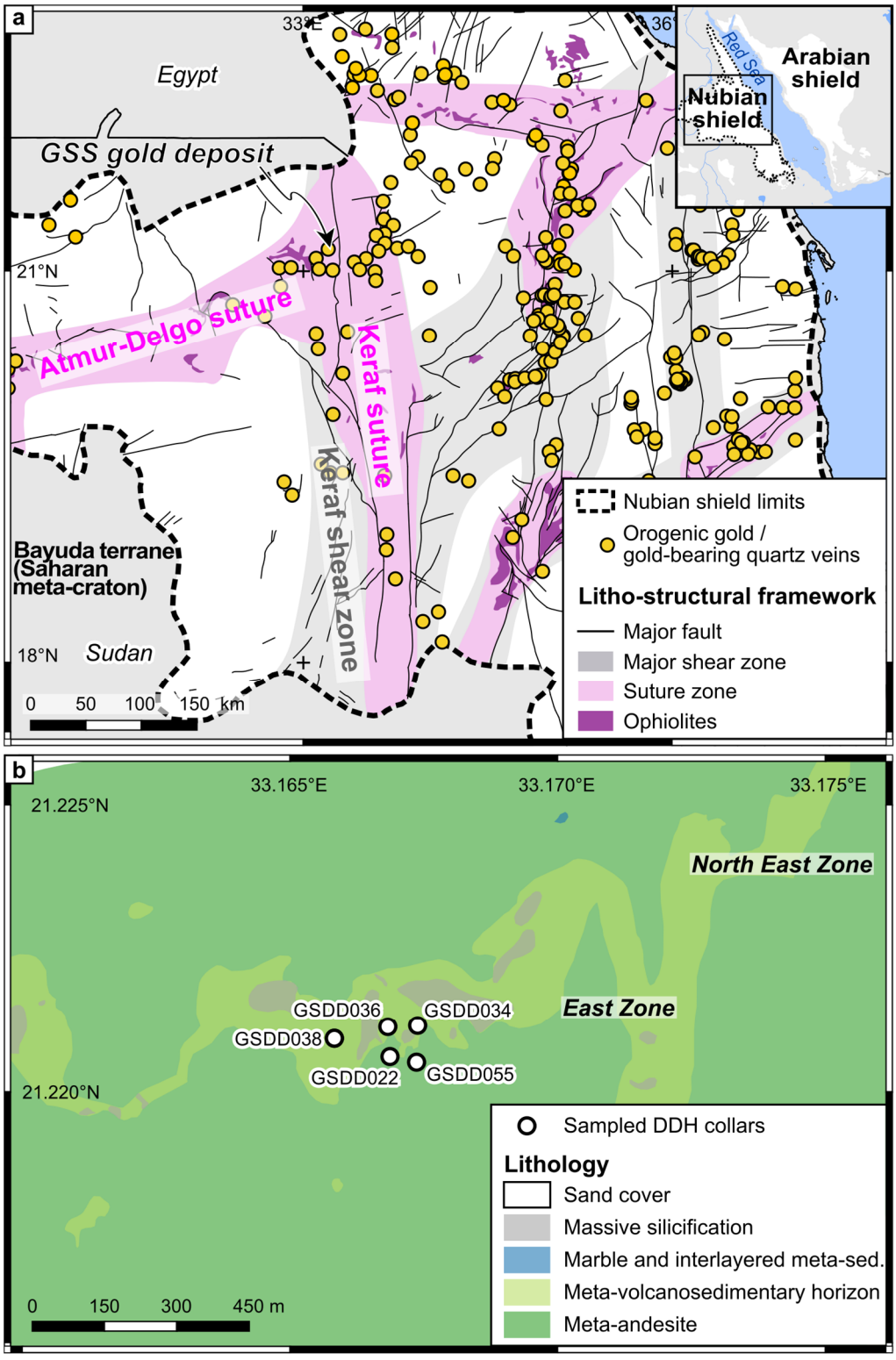

Figure 1: Geological setting of the Galat Sufar South (GSS) gold deposit, adapted after Perret et al. (2020). **a** Structural framework of the Nubian shield, simplified after Johnson et al. (2011) and references therein. Gold occurrences are from the Arethuse Geology GIS compilation database. **b** Lithological framework of the GSS gold deposit. The collar location of sampled diamond drill holes (DDHs) for this study is indicated. Geographic coordinates are reported according to the WGS 84 coordinate system.

The GSS deposit is located within the western portion of the Arabian-Nubian shield (ANS; Fig. 1a) which represents the northern part of the East African-Antarctic Orogeny (Stern, 1994; Johnson and Woldehaimanot, 2003; Kusky et al., 2003; Fritz et al., 2013; Grenholm, 2019). The Arabian-Nubian shield formed during a ~ 850-550 Ma "Supercontinent Cycle" (Stern and Johnson, 2010; Johnson et al., 2011) and results from the amalgamation and collision between terranes that accreted onto the Saharan meta-craton (Fig. 1a; Johnson and Woldehaimanot, 2003; Johnson et al., 2011 and references therein). The terranes are formed by juvenile magmatic arc and ophiolite assemblages remnants of the subduction and obduction processes that completely consumed the Mozambique ocean in the northern part of the East African-Antarctic Orogen (e.g. Burke and Sengör, 1986; Johnson et al., 2011; Fritz et al., 2013 and references therein).

The east-striking Atmur-Delgo and north-striking Keraf sutures record the collision of the Arabian-Nubian shield with the Saharan meta-craton (Fig. 1a; Almond and Ahmed, 1987; Stern, 1994; Abdelsalam et al., 1995, 1998; Bailo et al., 2003). The Atmur-Delgo suture results from the closure of an aulacogenic oceanic re-entrant associated with the Mozambique ocean into the Saharan meta-craton (Burke and Sengör, 1986; Abdelrahman, 1993; Denkler et al., 1993; Harms et al., 1994; Schandelmeier et al., 1994; Abdelsalam et al., 1998), while the Keraf suture results from the evolution of the Keraf island arc prior to arc-continent collision (Perret, 2021) and amalgamation of terranes forming the Arabian-Nubian shield over the Saharan meta-craton (Fig. 1a; Vearncombe, 1983; Burke and Sengör, 1986; Frisch and Pohl, 1986; Berhe, 1990; Abdelsalam and Dawoud, 1991; Ries et al., 1992; Mosley, 1993; Abdelsalam et al., 1998; Fritz et al., 2013). During the late collision period, the Keraf suture has been overprinted by a sinistral transpression resulting in the Keraf shear zone (Fig. 1a; Abdelsalam et al., 1995, 1998; Abdelsalam and Stern, 1996a, 1996b; Perret et al., 2021).

The GSS gold deposit is encompassed within a complexly deformed zone at the junction between the Atmur-Delgo and Keraf sutures (Fig. 1a), both structures hosting

gold occurrences (Johnson et al., 2017; Gaboury et al., 2020; Perret et al., 2020, 2021). It is hosted by a strongly deformed, interleaved andesitic meta-volcanosedimentary horizon enclosed within a thick andesitic meta-volcanic sequence composed of lava flows, pyroclastic horizons and primary volcanic breccia (Fig. 1b; Perret et al., 2020). This assemblage is surrounded by meta-pelites interlayered with marbles. The deposit-scale structural framework is complex and dominated by subvertical linear fabrics, including several km- to dm-scale sheath folds inferred from satellite imagery and outcrop structural analysis (Perret et al., 2020). The GSS gold deposit recorded a complex deformation history related to several veining and alteration events. The simplified mineral paragenesis related to the deformation events is summarised in Figure 2 (for more details, please refer to Perret et al., 2020). It started with an early, ductile-dominated, progressive D_{1GSS}-D_{2GSS}-(D_{3GSS}) deformation episode associated with the main gold event. It ended with a minor, late, brittle D_{4GSS} veining episode related to a minor mineralisation event (Figs. 2 and 3).

The ductile D_{1GSS} deformation stage is characterised by the D_{1aGSS}-related S_1 foliation, F_1 folding and a change from carbonate-dominant with minor quartz and pyrite to D_{1bGSS}-related quartz-pyrite-dominant with minor carbonate veining and disseminated pyrite grains (Fig. 3a to d). The increase in pyritisation from D_{1aGSS} to D_{1bGSS} veining is correlated with an increase in gold grades (from < 0.1 g/t to ~ 1 g/t Au; fire assays data from Orca Gold Inc.'s database are given for studied samples in Table 1) and is thought to represent the first gold input into the system (Perret et al., 2020).

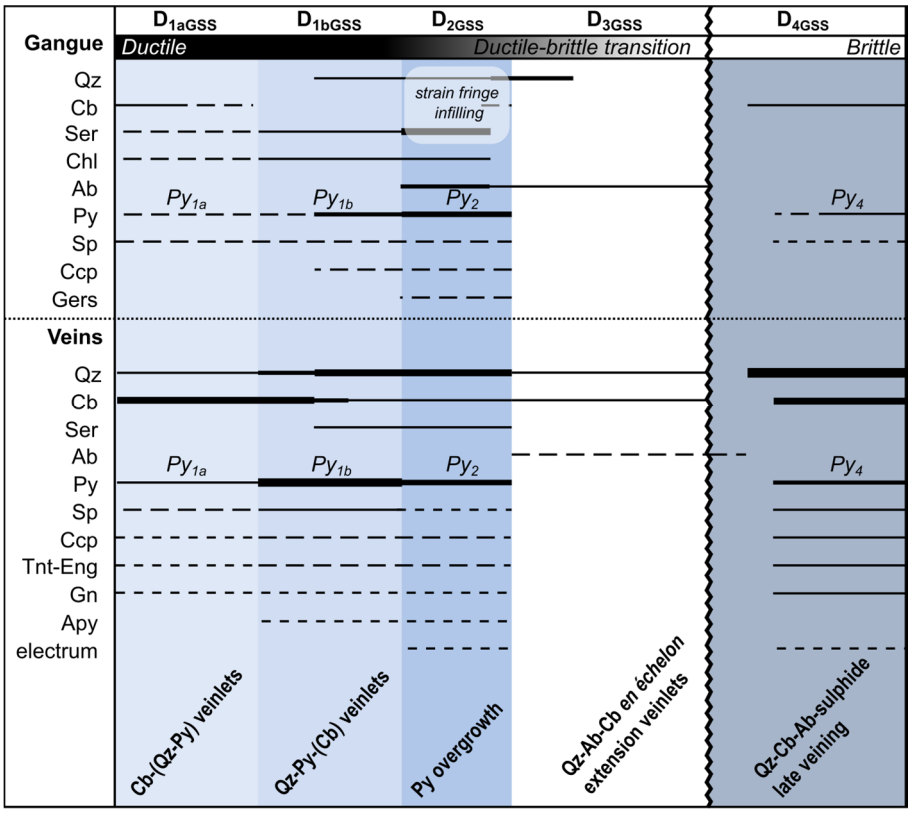

Figure 2: Simplified mineral paragenesis of the Galat Sufar gold deposit, modified after Perret et al. (2020). The broken line separates the D_{1GSS}-D_{2GSS}-(D_{3GSS}) progressive deformation stages from the late D_{4GSS} deformation event. Mineral abbreviations for Figures 2 to 7, 9, 10 and 12 and Table 1 are Qz, quartz; Cb, carbonate; Ser, sericite; Chl, chlorite; Ab, albite; Py, pyrite; Sp, sphalerite; Ccp, chalcopyrite; Tnt-Eng, sulphosalt (tennantite-enargite); Gn, galena; Apy, arsenopyrite; Gers, gersdorffite. Pyrite generations are indexed regarding the deformation stage they relate to (see details in Perret et al., 2020).

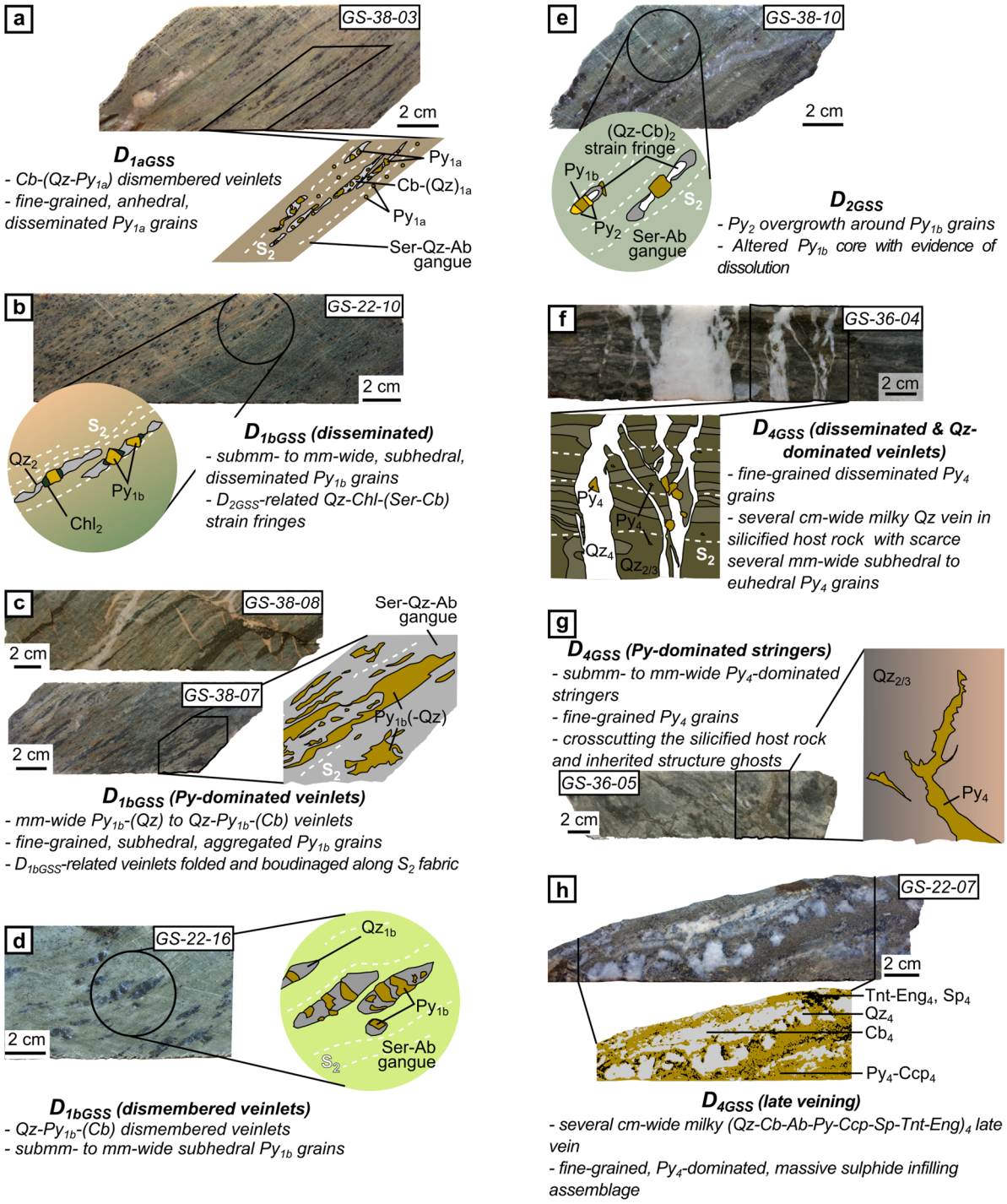

Figure 3: Macroscopic scale features of pyrite generations identified at the Galat Sufar South gold deposit. Mineral abbreviations are the same as in Figure 2. Mineral generations are indexed based on the deformation stage they relate to (see details in Perret et al., 2020). **a** D_{1aGSS}-related pyrite. **b** D_{1bGSS}-related, disseminated pyrite with asymmetrical D_{2GSS}-related quartz-chlorite-(sericite-carbonate) strain fringes. **c** D_{1bGSS}-related pyrite in folded pyrite-dominated veinlets. **d** D_{1bGSS}-related pyrite in quartz-pyrite-(carbonate) veinlets. **e** D_{2GSS}-related pyrite as overgrowth around Py_{1b} grains. **f** D_{4GSS}-related pyrite disseminated in silicified intervals and enclosed in a crosscutting milky quartz veinlet. **g** D_{4GSS}-related pyrite-dominated stringers crosscutting highly silicified host rock intervals. **h** D_{4GSS}-pyrite in quartz-carbonate-albite-polymetallic sulfide assemblage late veins.

The ductile D_{2GSS} deformation stage controls the GSS structural framework from the tens of km- to the µm-scales. It is mostly characterised by subvertical, linear, ductile structures such as a L_2 stretching lineation. The C/S_2 penetrative shear band cleavage, simplified into S_2 in illustrations and below, is the main planar fabric but remains less expressed than linear features. D_{1GSS}-related veins are boudinaged, folded and dismembered along the S_2 fabric (Fig. 3a, c and d) and pyrite overgrowth and strain fringes are developed around D_{1GSS}-related pyrite grains (Fig. 3e). These microstructures form ore shoots (>1 g/t Au, up to >15 g/t Au; Table 1) contributing to the main gold mineralisation at the GSS gold deposit.

The ductile-brittle D_{3GSS} transition is portrayed by kink bands affecting the sericite-rich gangue, quartz-albite-carbonate *en échelon* extension veins. No mineralisation formed during this deformation stage. Meanwhile, a pervasive silicification event locally affected the meta-volcanosedimentary host rock during the D_{2GSS}-D_{3GSS} ductile to ductile-brittle deformation.

The late, brittle D_{4GSS} veining extent is limited to these silicified host rock intervals, as a response to rheological contrast with less competent, non-silicified, sericite-rich host rocks. It remains unclear whether if the vein system forms a stockwork with a preferential orientation or not. The vein mineral assemblage ranges from barren quartz-carbonate-albite to highly mineralised (up to >10 g/t Au; Table 1) polymetallic sulphide assemblage (Fig. 3f, g and h). This episode formed very local high-grade ore shoots with a minor contribution to the overall GSS gold endowment.

The gold input or remobilisation nature of each mineralisation event remains uncertain from the petrological-structural data available up to now (Perret et al., 2020).

4. Analytical procedures

4.1. Petrography

Samples illustrated in Figures 3-8 are listed in Table 1. Thin sections and one-inch epoxy mounts have been prepared for these samples. Optical microscopy and additional analyses using a scanning electron microscope in back-scattered electron mode (BSE-SEM) were carried out for petrography work at the GeoRessources laboratory (Université de Lorraine-CNRS, Nancy, France).

		Results presented in this study			
Sample ID*	**Grade (g/t Au)**	*Petrography* *(Figs. 3, 4)*	*HRXCT* *(Fig. 5, ESM 1)*	*EBSD* *(Figs. 6, 7)*	*LA-ICP-MS* *(Figs. 8-10, Table 2, ESM 2)*
GS-22-06	0.08	x			x
GS-22-07	3.56	x			x
GS-22-08	0.28	x		x	x
GS-22-10	0.19	x			x
GS-22-16	2.07	x			
GS-34-05	6.45	x		x	x
GS-34-07	3.89	x	x		
GS-36-04	0.08	x			x
GS-36-05	0.12	x			x
GS-38-03	0.51	x			
GS-38-05	15.2	x			x
GS-38-07	3.14	x		*x*	
GS-38-08	1.06	x		*x*	x
GS-38-09	1.79	x	*x*		
GS-38-10	8.64	x			
GS-38-12	7.70	x			x
GS-55-02	0.02	x			x

** Samples are named after the ID of the diamond drill hole they have been sampled from and are organised by increasing depth. Fire assay results of the corresponding 1 m-large drill core interval have been communicated by Orca Gold Inc. All samples have been described at the macroscopic and microscopic scales, but samples GS-34-05 and GS-34-07 are not illustrated in Figures 3 and 4. In italics: samples analysed through HRXCT and EBSD which are not illustrated in this study.*

Table 1: List of samples from this study, along with the corresponding analyses that they underwent.

4.2. High-resolution X-ray computed tomography

HRXCT analyses were performed to reconstruct the 3D geometry of sulphide-rich mineralised D_{2GSS} microstructures which orientation cannot be measured using conventional methods. HRXCT scans of billets GS-34-07 and GS-38-09 (Table 1) were acquired at the GeoRessources laboratory (University of Lorraine, Nancy, France) with a Phoenix Nanotom S scanner, using a CCD Hamamatsu detector, with 2300×2300 pixels resolution. Analytical conditions were set to 75 mA current and 112 kV acceleration voltage with a 85-mm source-sample distance. Fifteen hundred projections were carried out, leading to a total scan time of 120 min. The spatial resolution was 17 µm/pixel (i.e. 4913 μm^3/voxel). Data visualisation was carried out using the Avizo® 9.2.0. software.

These two samples were chosen as they are the only mineralised samples showing every structure attributed to the D_{2GSS} deformation phase at the macroscopic scale. In the following section, we have decided to only describe HRXCT results for sample GS-34-07, as it is similar to sample GS-38-09 but offers a better visibility of sulphide microstructures due to fewer disseminated sulphides blurring the 3D internal reconstruction.

4.3. Electron back-scattered diffraction

EBSD analyses were performed to characterise the microstructures of mineralised sulphide assemblage in four samples containing D_{2GSS}-related mineralised microstructures (Table 1). These samples have been chosen for EBSD analysis after a careful preliminary petrographic work to ensure they were representative of D_{2GSS} deformation-mineralisation relationships expressed at the GSS gold deposit. Simultaneous energy-dispersive spectrometry (EDS) and EBSD mapping were carried out at the University of Montpellier (France) using a Camscan Crystal Probe X500FE scanning microscope with

EBSD Symmetry and EDS UltimMax 100 detectors. Probe current, acceleration voltage and chamber pressure were set to 5 nA approximately, 20 kV and 2 Pa in low-vacuum mode, respectively, with a 25-mm working distance. Step size was set to 1.2 µm (e.g. GS-22-08) and 1 µm (e.g. GS-34-05). Data collection monitoring and data processing were carried out using the AZtecHKL and HKLChannel5 Project Manager softwares, respectively. In the following, we have decided to only describe EBSD results for sample GS-22-08 and GS-34-05, as they are the most representative of D_{2GSS}-related mineralised microstructures (disseminated or quartz vein-hosted pyrite with Py_2 overgrowth, respectively). Besides GS-38-07 and GS-38-08 samples provided similar results to GS-34-05, but with no visible gold.

4.4. Laser ablation inductively-coupled plasma mass spectrometry on pyrite

LA-ICP-MS data on the different pyrite generations separated at the GSS gold deposit were collected at the Queen's Facility for Isotope Research (Queen's University, Ontario, Canada) using a ThermoScientific X Series 2® quadrupole ICP-MS coupled to a NewWave/ESI 193-nm ArF Excimer laser system. Samples for which laser ablation analyses were carried out are listed in Table 1. The isotopes measured were ^{29}Si, ^{34}S, ^{51}V, ^{52}Cr, ^{55}Mn, ^{57}Fe, ^{59}Co, ^{60}Ni, ^{65}Cu, ^{66}Zn, ^{71}Ga, ^{75}As, ^{77}Se, ^{95}Mo, ^{107}Ag, ^{111}Cd, ^{115}In, ^{118}Sn, ^{121}Sb, ^{125}Te, ^{182}W, ^{197}Au, ^{205}Tl, ^{208}Pb and ^{209}Bi, with a dwell time of 10 ms.

Spot analyses were performed to closely match the observed micro-textures in pyrite grains with their specific trace element signatures. Care was taken in selecting spot positions, especially in Py_{1b} altered cores, to minimise the ablation of any visible mineral inclusion, as well as during subsequent data processing and signal integration to remove the signal of any sulphide or metal alloy mineral inclusion and focus solely on the lattice-bound trace element composition of pyrite minerals. Prior to each analysis, the background signal, or gas blank, was measured for a duration of 25 s. The beam diameter

was set to 50 μm for all samples and reference materials, with a pulse frequency of 10 Hz.

Elemental maps were also produced to (i) better understand the spatial distribution of the trace elements present in the different types of pyrite, (ii) complement the data derived from spot analyses and (iii) match areas that were mapped through EBSD to better constrain micro-deformation influence on elemental mobility in sulphide mineral assemblages. The set up used for laser mapping was the same as above. Similarly to spot analyses, a 25 s gas blank was measured prior to each ablation line. Beam size was set to 15 μm, to allow for a minimum of 40 horizontal lines per map for better image resolution. The laser scan speed was set to 8 μm/s and the pulse frequency to 10 Hz. The fluence for both spot and map analyses was about 8.0 J/cm^2.

The LA-ICP-MS data were reduced with Iolite 3.65 (Paton et al., 2011). Spot analyses comprise blocks of 30 spots on samples bracketed by a series of 3 spots on each of the 6 certified reference materials. Similarly, for map analyses, three standard lines were analysed for each standard at the beginning and end of the analytical run to account for analytical drift and allow semi-quantification.

The reference standards were USGS GSE-1G (Jochum et al., 2005), MASS-1 (Wilson et al., 2002), as well as FeS-4, FeS-5, PTC-1b and CCU-1e sulphide reference materials from Université du Québec à Chicoutimi, Canada (CCRM, CANMET). FeS-5 was used for trace element quantification in pyrite spot analyses and correction for variations in ablation efficiency. Limits of detection (LOD) were calculated following the Howell's method (see references in Howell and Blakey, 2013). LA-ICP-MS elemental maps were edited using the Monocle add-on to determine trace element compositions of specific areas and textures of the grains of interest (Petrus et al., 2017).

5. Results and integration to previous petrological-structural field observations

5.1. Petrological-structural description of the mineralised sulphide assemblages

From the mineral paragenesis established for the GSS gold deposit by Perret et al. (2020) (Fig. 2), four pyrite generations have been described and are labelled from Py_{1a} to Py_4, each referring to the deformation stage they relate to (D_{1aGSS} to D_{4GSS}). The same labelling scheme is used for the other mineral phases illustrated in the figures below. The macroscopic and microscopic textural and structural characteristics of each pyrite generation are documented below and illustrated in Figures 3 and 4, respectively.

5.1.1. Py_{1a}

Py_{1a} occurs as disseminated grains in the sericite-rich gangue. They are wrapped by the S_2 penetrative cleavage (Figs. 3a, 4a).

There are also rare, fine-grained (<100 µm), anhedral Py_{1a} grains in D_{1aGSS}-related carbonate-dominated veinlets dismembered along the S_2 fabric (Figs. 3a, 4a). Within these veinlets, Py_{1a} is associated with scarce chalcopyrite, sphalerite and sulphosalt (Fig. 4a).

5.1.2. Py_{1b}

Py_{1b} is characterised by disseminated grains, affected by the S_2 penetrative cleavage, similarly to Py_{1a} grains. These grains are coarser than disseminated Py_{1a} grains (up to 500 µm), subhedral and display C_2 simple shearing-related asymmetrical quartz-chlorite-(sericite-carbonate) strain fringes, formed during the subsequent D_{2GSS} deformation stage (Figs. 3b, 4b).

Py_{1b} is also visible in D_{1bGSS}-related veinlets. The increase in pyrite modal proportion from about 30 to >50 vol% from D_{1aGSS} to D_{2bGSS} veining stages is correlated with the switch from carbonate-dominated to quartz- and/or pyrite-dominated veinlets. Pyrite-dominated veinlets may be F_2-folded, transposed and dismembered along the S_2

penetrative cleavage (Fig. 3c). In these veinlets, Py_{1b} is fine-grained and displays 120°-triple junction grain boundaries, i.e. annealing during recrystallisation, and interstitial polymetallic sulphide minerals (sphalerite, sulphosalt in Figure 4c). Dismembered quartz-dominated veinlets (Fig. 3d) host coarser (up to about 300 µm), subhedral Py_{1b} grains intergrown with the same sulphide mineral phases (Fig. 4d). If no Py2 overgrows Py1b grains, they look unaltered and do not host any mineral inclusion.

5.1.3. Py_2

Py_2 overgrows disseminated Py_{1b} grains displaying strain fringes, resulting on Py_{1b}/Py_2 grains preferentially elongated along the S_2 fabric (Fig. 3e). At the macroscopic scale, the distinction between core and rims is sometimes possible. At both the macroscopic and microscopic scales, the Py_{1b} core shows an altered aspect with evidence of dissolution when overgrown by Py_2 (Figs. 3e, 4e). Py_2 overgrowth is also visible around Py_{1b} grains in dismembered quartz-dominated veinlets (Fig. 4f). Where Py_2 is observed, Py_{1b} cores systematically enclose inclusions of silicate, phosphate (apatite in Figure 4e), sulphide minerals (chalcopyrite in Figure 4e, arsenopyrite and sulphosalt in Figure 4f) and electrum (Fig. 4f). Rare cogenetic gersdorffite occurs as a thin coating around the rim of Py_2 (Fig. 4e). This generation of pyrite is interpreted to be coeval with the S_2 main penetrative cleavage and L_2 stretching lineation which control the ore shoot distribution at the deposit scale (Perret et al., 2020).

5.1.4. Py_4

The late, brittle D_{4GSS} veining encompasses all veins from non-mineralised quartz-carbonate-albite ones to polymetallic sulphide assemblage-dominated ones. Several Py_4 facies can be distinguished depending on pyrite relative abundance and textural association with other sulphide mineral phases.

Firstly, rare, coarse, subhedral Py_4 grains (Fig. 3f) occur with traces of intergrown sphalerite (Fig. 4g) in almost pyrite-free milky quartz-dominated veins. Very fine-grained

disseminated Py_4 grains overprint the silicified mineral gangue at the selvages of these veins (Fig. 4g). These veins are non-mineralised (<0.1 g/t Au; Table 1).

Secondly, Py_4-dominated stringers also cut across the silicified host rock intervals (Fig. 3g) and are formed by aggregated subhedral to anhedral Py_4 grains of variable size with minor interstitial sphalerite (Fig. 4h). Disseminated Py_4 is still visible at the selvages of the pyrite stringers and seems to expand from its margins (Fig. 4h). These stringers are weakly mineralised (about 0.1 g/t Au; Table 1).

Thirdly, wider polymetallic sulphide-dominated late veins locally cut across the silicified host rock (Fig. 3h). Where the soft sulphide minerals, such as chalcopyrite and minor sulphosalts (Fig. 4i), are more abundant than pyrite, Py_4 occurs as coarse, rounded, grains embedded in the soft sulphide mineral matrix (Fig. 4i). Conversely, where pyrite is dominant, Py_4 aggregates are largely fractured and soft sulphide minerals infill fractures (Fig. 4j). Such Py_4 grains may host electrum micro-inclusions (Fig. 4k). These veins are mineralised (7.7 g/t Au; Table 1).

While all pyrite generations were investigated for trace element signature through LA-ICP-MS analyses, HRXCT and EBSD analyses were only applied to $Py_{1a/b}$ and Py_2 generations. Indeed, $Py_{1a/b}$ and Py_2 generations relate to the regional progressive D_{1GSS}-D_{2GSS} deformation event coeval to the main gold mineralisation event defined at the GSS deposit, whereas the regional interpretation of D_{4GSS} remains unknown and associated gold mineralisation is limited (Perret et al., 2020).

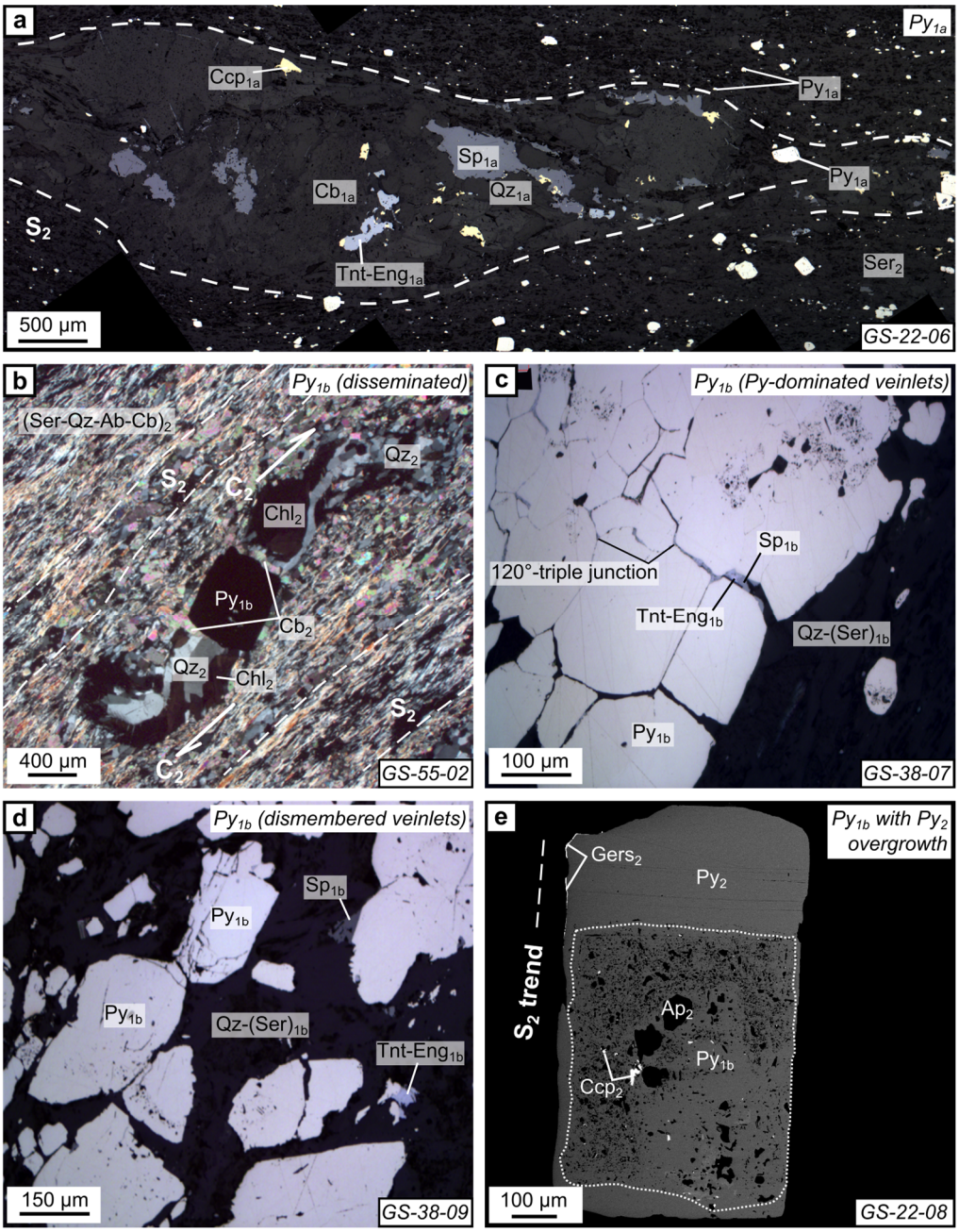

Figure 4: Microscopic scale features of pyrite generations identified at the Galat Sufar South gold deposit. Mineral abbreviations are the same as in Figure 2. **a**, **b**, **e, f**, **j** and **k** photographs are from Perret et al. (2020). **a** D_{1a}-related pyrite associated with scarce chalcopyrite, sphalerite and sulphosalt in carbonate-dominated veinlets (reflected light). **b** Disseminated Py_{1b} grains are associated with quartz-chlorite-carbonate asymmetrical strain fringes related to E block-to-the-top C_2 shearing (cross-polarised, transmitted light). **c** Interstitial sulphosalt-sphalerite assemblage infilling 120°-triple junction grain boundaries in Py_{1b}-dominated veinlets (reflected light). **d** Rare sphalerite and sulphosalt associated with coarse Py_{1b} grains in quartz-pyrite-dominated dismembered veinlets (reflected light). **e** Py_2 overgrowth occurs around disseminated Py_{1b} grain with evidence of dissolution and enclosing a lot of mineral inclusions (back-scattered electron mode in scanning electron microscopy, BSE-SEM).

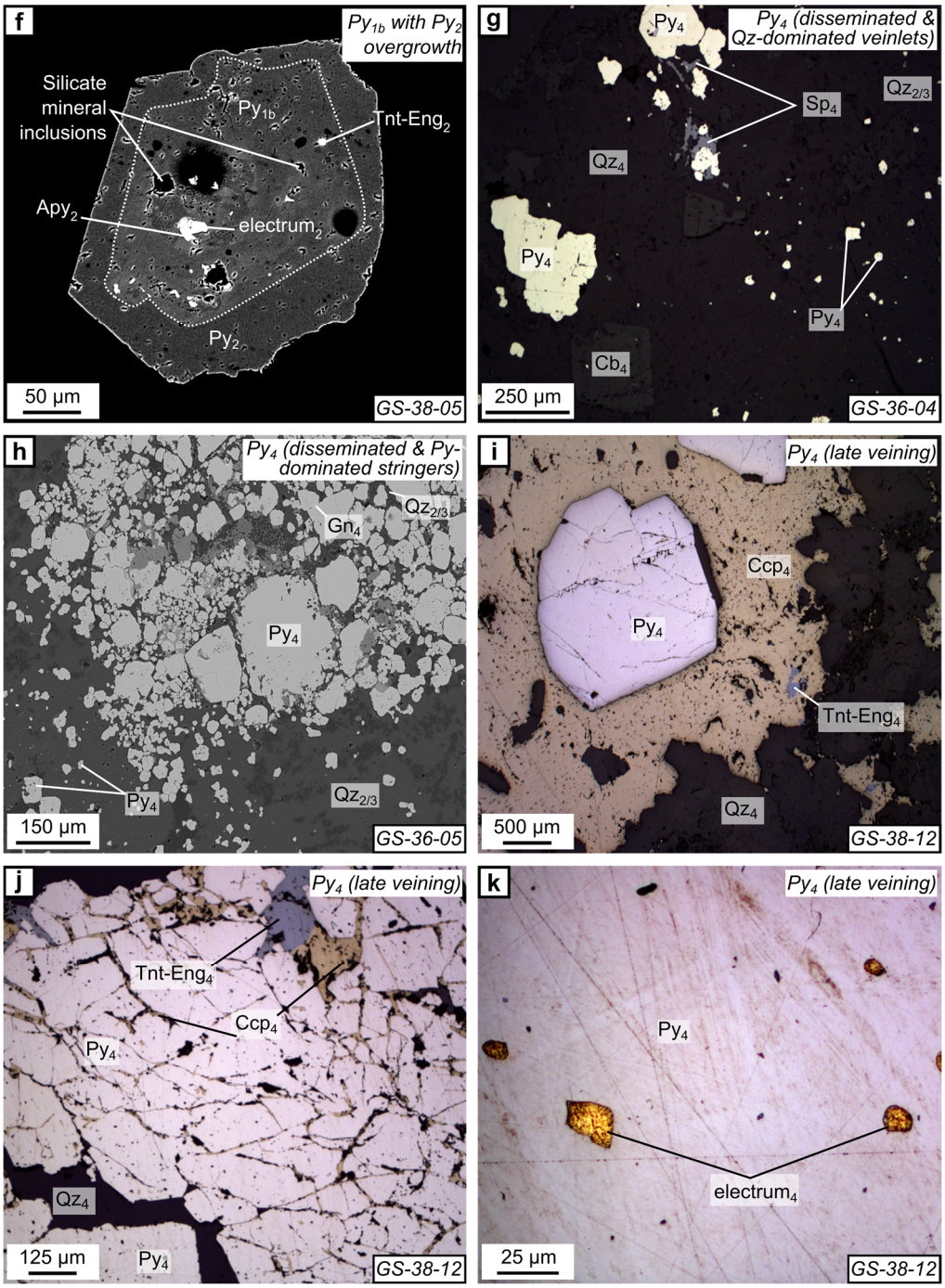

Figure 4 (continued): Microscopic scale features of pyrite generations identified at the Galat Sufar South gold deposit. Mineral abbreviations are the same as in Figure 2. **a**, **b**, **e, f**, **j** and **k** photographs are from Perret et al. (2020). **f** Py_2 overgrowth around Py_{1b} grains in quartz-pyrite-dominated dismembered veinlets, presence of silicate, sulfide and electrum inclusions in the pyrite core (BSE-SEM). **g** Disseminated Py_4 spatially associated with crosscutting quartz-carbonate veinlet hosting rare, coarser Py_4 grains (reflected light). **h** Rare sphalerite is interstitial to aggregated pyrite grains in a Py_4-dominated stringer. Fine-grained, disseminated Py_4 facies expands from the margins of the stringer (BSE-SEM). **i** Coarse, rounded Py_4 grains embedded in a chalcopyrite-(sulphosalt) assemblage in quartz-carbonate-albite-sulfide late veins (reflected light). **j** Py_4 with sulphosalt-chalcopyrite assemblage infilling in pyrite grain joints and cracks in a Py_4-dominated late vein (reflected light). **k** Fine-grained electrum inclusions in Py_4 grains (reflected light).

5.2. High-resolution X-ray computed tomography: 3D geometry of mineralised microstructures

Sample GS-34-07 is a 5 cm-long slab that has been cut along a half core sample. It displays a schistose texture dominated by the subvertical S_2 cleavage along which carbonate- and sericite-rich bands alternate (Fig. 5a). The S_2 orientation is N080°E-84°N (Fig. 5a). A F_2-folded D_{1GSS}-related veinlet transposed along the S_2 cleavage is visible on this sample (Fig. 5a).

The fold axis orientation could not be measured directly on the drill core due to the small size of the microstructure. An oriented billet has been cut to prepare an oriented thin section centered on this micro-fold (Fig. 5a and b). At the microscopic scale, the folding and individually-fragmented boudinaged structure of the D_{1aGSS}-related carbonate-dominated veinlet are clearly visible (Fig. 5b). However, switching from the macroscopic 3D sample and drill core observations to the microscopic 2D thin section-scale only provides a partial view of the folded veinlet.

The oriented billet remaining from the preparation of this thin section was scanned by HRXCT. The 3D reconstruction shows that D_{1aGSS}-related sulphide-rich veinlets are transposed and folded along the S_2 planar fabric, well characterised in the sericite-rich gangue (Fig. 5c). A subhorizontal section shows that F_2 folding is similar and tight, with S_2 being the related axial planar cleavage (Fig. 5c and d). Sulphide-rich fold hinges are more or less dismembered, which leads to the formation of linear sulphide micro-ore shoots (Fig. 5c and d). These linear mineralised microstructures are parallel to the F_2 fold axis and steeply plunge westwards, which is consistent with the deposit-scale L_2 stretching lineation orientation (Perret et al., 2020). HRXCT thus illustrates that F_2 micro-hinges form L_2-parallel micro-ore shoots consistent with (i) the deposit-scale F_2 fold axis orientation and (ii) the deposit-scale ore shoot orientation that is controlled by the regional L_2 stretching lineation (Perret et al., 2020). This demonstrates the 3D continuity of the structural control on GSS gold mineralisation from the district to the

microscopic scales and strengthen conclusions suggested from conventional field and microscopy work. The complete 3D data are available in Supplementary Material 1.

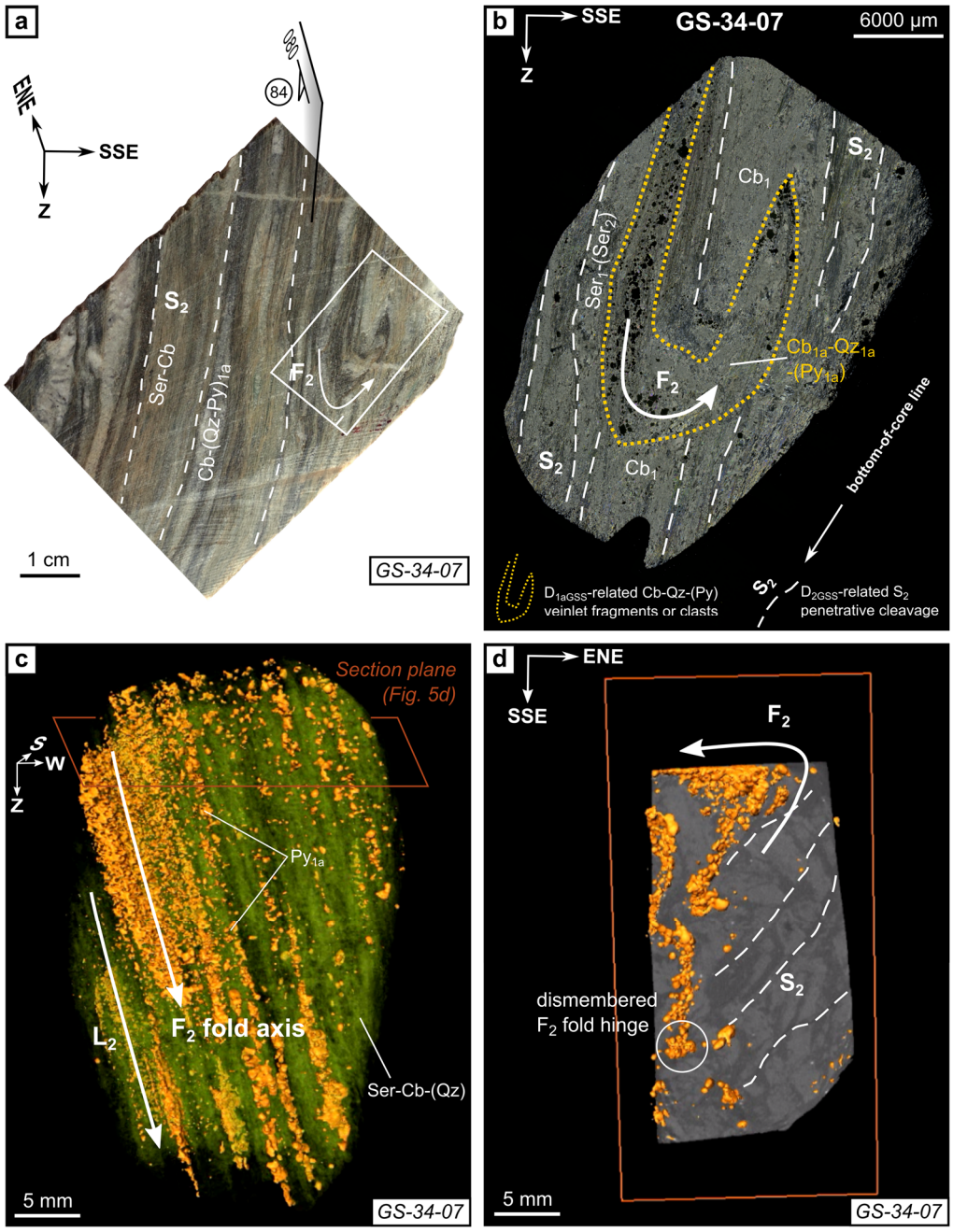

Figure 5: High-resolution X-ray computed tomography (HRXCT) results for the sample billet GS-34-07. Mineral abbreviations are the same as in Figure 2. **a** View of the half core slab of sample GS-34-07. The white rectangle corresponds to the oriented billet cut for thin section preparation, centered on a F_2-folded carbonate-(quartz-pyrite) veinlet. **b** Scan of the GS-34-07 thin section (cross-polarised, transmitted light). **c** CT scan of the billet GS-34-07. Green color corresponds to gangue minerals affected by the S_2 fabric whereas orange color refers to sulfide minerals. The CT scan has been reoriented according to the orientation of the sample block. **d** Subhorizontal section across the billet GS-34-07. Gangue and sulfide minerals are in grey and orange colors, respectively.

5.3. Electron back-scattered diffraction: intra-crystalline deformation of mineralised sulphide assemblages

5.3.1. $Py_{1b/2}$ grain (GS-22-08)

We investigated a disseminated pyrite grain composed of a Py_{1b} core and a Py_2 rim (referred to as $Py_{1b/2}$ grain hereafter) in the low-grade sample GS-22-08 (0.28 g/t Au; Table 1; Fig. 6). The Py_{1b} core encloses numerous silicate, phosphate and sulphide inclusions where the Py_2 rim is observed (Fig. 6a). The latter preferentially grows along S_2 main fabric trend and displays a very thin gersdorffite fringe (Fig. 6b). Both pyrite and gersdorffite crystallise in the isometric system, with close unit cell parameters (Bayliss, 1968, 1977). One electron back-scattered pattern (EBSP) was acquired for each mineral phase (datapoint 1 for gersdorffite and 2 for pyrite, respectively, in Fig. 6b close-up) to compare their respective crystallographic orientation. The 3D reconstruction of the unit cell corresponding to the EBSPs highlights the similar crystallographic orientations of the pyrite overgrowth and the gersdorffite coating. Such similarities in unit cell parameters suggest that these two mineral phases formed as a continuous crystallographic unit.

The entire pyrite grain was mapped with EBSD. Data processing allowed to isolate the coarse, disseminated pyrite grain of interest, as well as quartz grains, mostly occurring in subvertical C_2-related asymmetrical strain fringes (Fig. 6c). The crystallographic orientation deviation angle is mostly $<1°$ and does not exceed 5° within the $Py_{1b/2}$ core-rim grain. The textural core-rim limit is not showing any deviation in the crystallographic orientation (Fig. 6d). However, the entire core-rim pyrite grain is divided into two distinct parts with a $<10°$-misorientation, which geometries match the subvertical C2 simple shearing kinematics locally inferred from strain fringes asymmetry (Fig. 6d). We also observe the presence of a $>30°$ misorientation grain boundary corresponding to a

single anhedral pyrite subgrain. This subgrain could have formed prior or after the D_{2GSS} deformation stage, and no evidence can help determining when this occurred.

The pyrite {100} crystallographic axis orientation is roughly consistent across the whole $Py_{1b/2}$ grain, except for the previously discussed potentially recrystallised subgrain (Fig. 6d). The Py_2 rim seems to have preferentially grown or recrystallised along the z axis (Fig. 6c). It is confirmed by the steeply north-northwest-plunging preferential orientation of the {100} axis for the $Py_{1b/2}$ grain in the pole figure (Fig. 6d).

In summary, the absence of subgrain boundary misorientation between the Py_{1b} core and the Py_2 rim (Fig. 6c) suggests that either (i) the Py_{1b} grain has been transposed along the L_2 fabric before the Py_2 overgrowth formed, through recrystallisation or a new fluid event, or (ii) the formation of Py_{1b} core is immediately followed by its destabilisation concomitant with *in situ* recrystallisation of the Py_2 rim. The preferential growth of Py_2 rim around Py_{1b} core along the L_2 stretching lineation confirms that its formation is coeval with the progressive D_{2GSS} deformation stage (Fig. 6d). The crystallographic continuity between the Py_2 overgrowth and the gersdorffite coating (Fig. 6b) supports their cogenetic precipitation. The EBSD analysis of sample GS-22-08 therefore confirms (i) the progressive nature of the D_{2GSS} deformation stage, (ii) the mineral paragenesis previously established from macroscopic and thin section observations and (iii) that the structural control on the GSS gold deposit by the L_2 fabric is visible up to the microscopic scale (Perret et al., 2020).

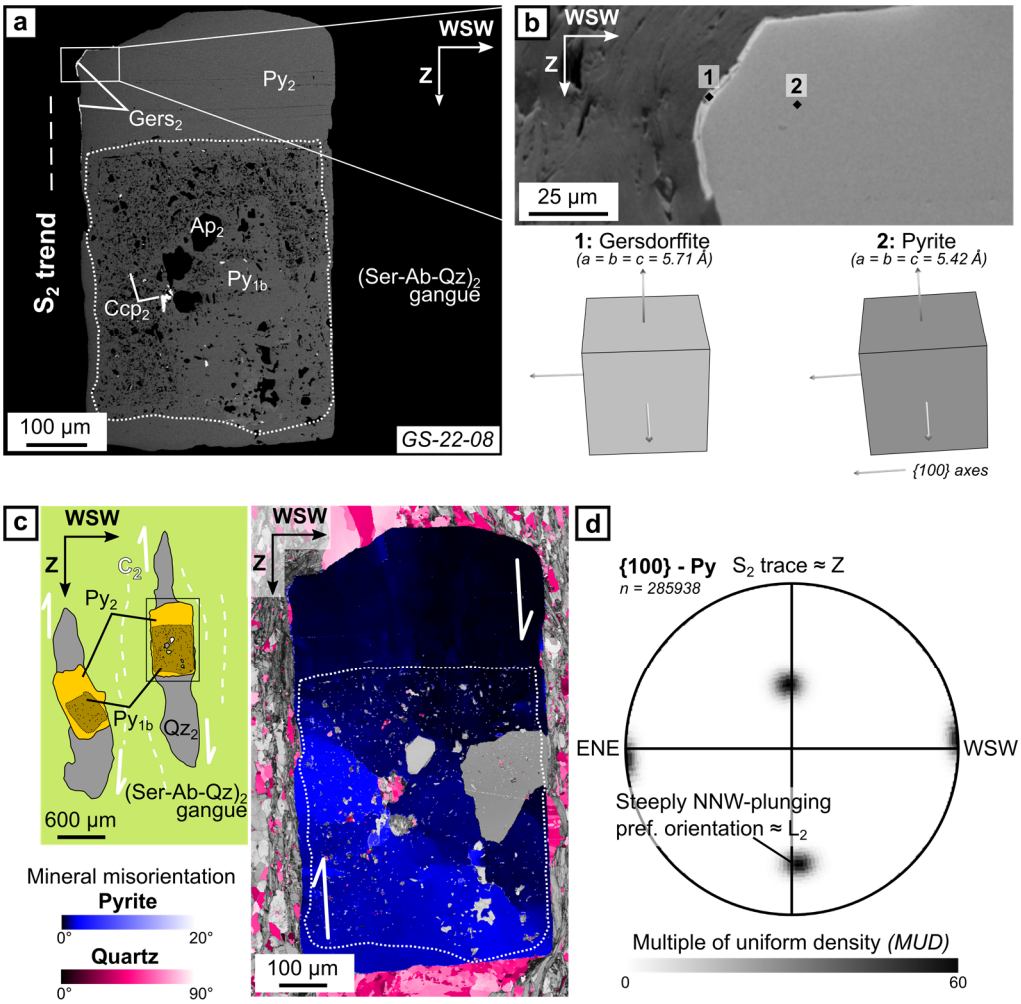

Figure 6: Electron back-scattered diffraction (EBSD) analysis of disseminated $Py_{1b/2}$ facies (sample GS-22-08). Mineral abbreviations are the same as in Figure 2. **a** BSE-SEM photograph of the investigated pyrite grain. **b** Zoom on the Py_2 overgrowth and intergrown gersdorffite coating and electron back-scattered patterns (EBSPs) of gersdorffite (1) and pyrite (2). **c** Orientation deviation angle map for pyrite and quartz considering a disseminated $Py_{1b/2}$ grain with E block-to-the-top, C_2-related asymmetrical quartz strain fringes (background: orientation contrast image considering all mineral phases). **d** EBSD pole figure representing the {100} axes of the coarse $Py_{1b/2}$ grain. *n* refers to the number of individual electron EBSPs used to construct the pole figure.

5.3.2. Mineralised quartz-pyrite veinlet (GS-34-05)

EBSD maps were produced for a Py_{1b}-Py_2-Ccp_2 assemblage in a D_{1bGSS}-related quartz-pyrite-dominated veinlet within the high-grade sample GS-34-05 (@6.45 g/t Au; Table 1; Fig. 7). The mineralised microstructure is completely dismembered along the S_2 main penetrative cleavage, making its margins hardly visible within the albite-sericite-quartz host rock. A zoom on the investigated area shows the textural relationship between Py_{1b} grain aggregates with associated Py_2 overgrowths and Ccp_2 infilling between 120°-triple junction annealed pyrite grains (Fig. 7a and b). Rare electrum associated with

Py_2 is visible in interstitial chalcopyrite (Fig. 7a and b). The orientation contrast background in Figure 7c shows a blurred aspect with lateral drift: this might result from a charging effect during EBSD data collection (e.g. Wright et al., 2015). Individual EBSPs indexing was nevertheless sufficient and the obtained EBSD map is considered to be reliable. The crystallographic orientation deviation angle between EBSPs measured in all pyrite grains ranges from 0 to 90°. Pyrite grain and subgrain boundaries are visible (Fig. 7c). As observed for sample GS-22-08 (subsection 5.3.1.; Fig. 6), the presence of Py_2 overgrowths around Py_{1b} cores is not associated with subgrain or grain boundaries (Fig. 7a, b and c).

Chalcopyrite crystallises in the tetragonal system in which the {001} crystallographic axis represents the *c* long axis. Although the interstitial chalcopyrite does not show any apparent preferential orientation at the microscopic scale (Fig. 7a, b and c), its {001} axis is mostly subvertical and oriented along the deposit-scale L_2 stretching lineation (Fig. 7d). This suggests that interstitial chalcopyrite either (i) formed during the D_{2GSS} deformation stage as well or (ii) is inherited and underwent a complete recrystallisation during the D_{2GSS} stage. The first option is more likely as there is no significant evidence for chalcopyrite formation during the D_{1GSS} stage (Fig. 2; Perret et al., 2020). Therefore, the presence of electrum inclusions in the interstitial chalcopyrite (Fig. 7a, b) and intergrown with sulphide inclusions in altered Py_{1b} cores (Fig. 4e and f) confirms that the D_{2GSS} event relates to the main visible gold mineralisation formed at the GSS gold deposit. Although these timing relationships between ore mineral generations and deformation stages were suggested from a conventional petrological-structural study (see Fig. 2; Perret et al., 2020), EBSD now provides robust evidence that confirms the mineral paragenesis.

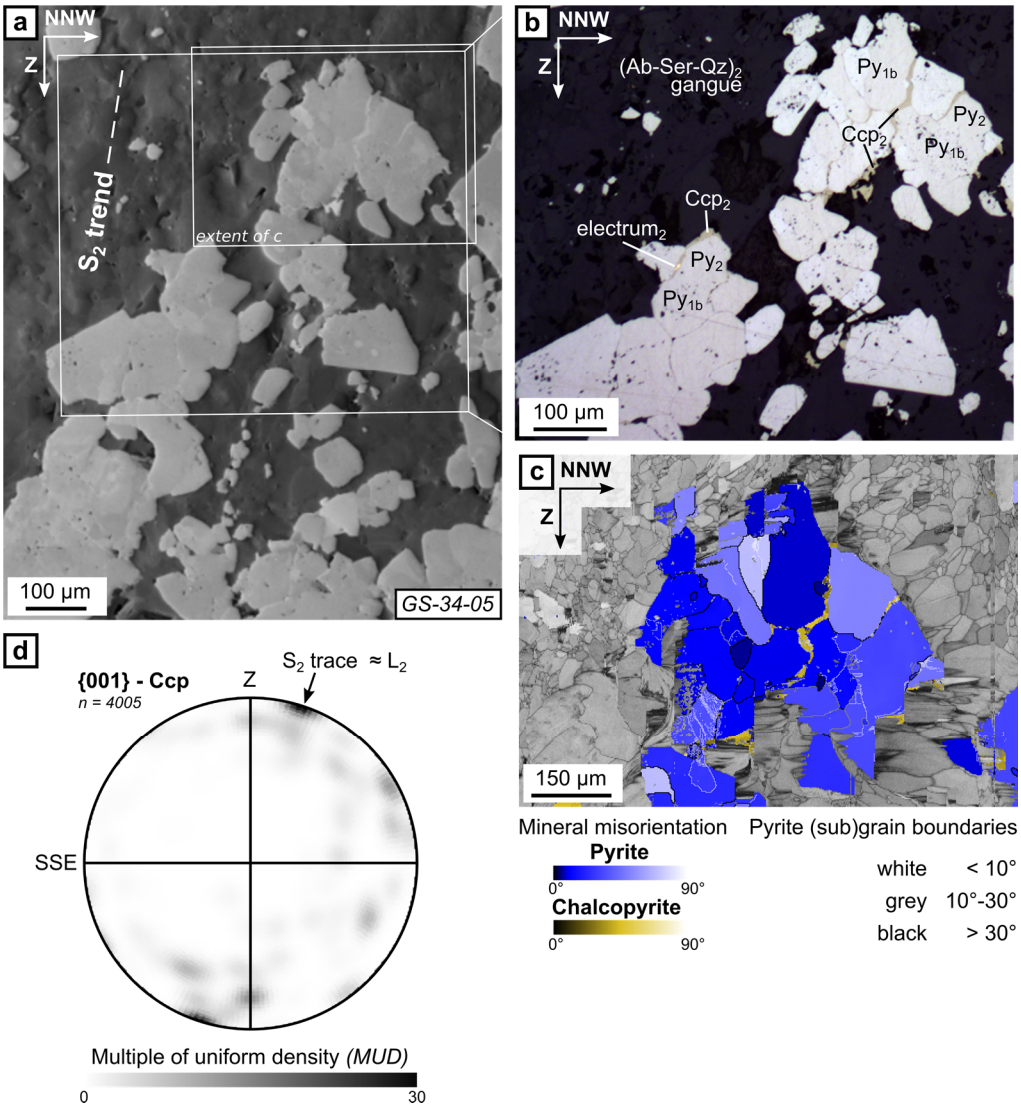

Figure 7: Electron back-scattered diffraction (EBSD) analysis of $Py_{1b/2}$ facies in quartz-pyrite-dominated veinlet (sample GS-34-05). Mineral abbreviations are the same as in Figure 2. **a** Orientation contrast image with (**b**) a zoom on the Py_{1b}-Py_2-(Ccp_2-electrum2) assemblage of interest (reflected light). **c** Orientation deviation image zoomed on pyrite and interstitial chalcopyrite assemblage (extent in **a**; background: orientation contrast image considering all mineral phases). **d** EBSD pole figure representing the {001} axes of interstitial Ccp_2, representing the distribution of the c long axis of chalcopyrite crystals in the tetragonal system. *n* refers to the number of individual electron EBSPs used to construct the pole figure.

5.4. LA-ICP-MS geochemical signature of pyrite generations

LA-ICP-MS data are summarised in Table 2 and are sorted by pyrite generations. Only the median and mean values of trace element concentrations and associated standard deviations are shown, with the complete dataset being made available in Supplementary Material 2. We focus below on the concentrations of some metals and metalloids of interest (Au, Ag, Te, Sb, Cu, Pb, As and Co) in each pyrite generation,

displayed in a box and whisker diagram (Fig. 8). We selected these specific elements as they are commonly associated with gold in sulphide minerals and help tracking ore-forming processes (see references in section 2.3.). While we carefully tried to remove signal from sulphide or metal alloy mineral inclusion during LA-ICP-MS data processing, we did not manage to systematically isolate the lattice-bound trace element composition in pyrite, resulting in obvious outliers in each statistical group. Comparisons are therefore made using the median value for trace element concentrations, unless otherwise stated, as the mean value may be overestimated due to nugget effect where micro-inclusions have been analysed. Similar results were obtained when analysing the data with or without these outliers, suggesting little to no influence of these rare micro-inclusions on the geochemical trends described below.

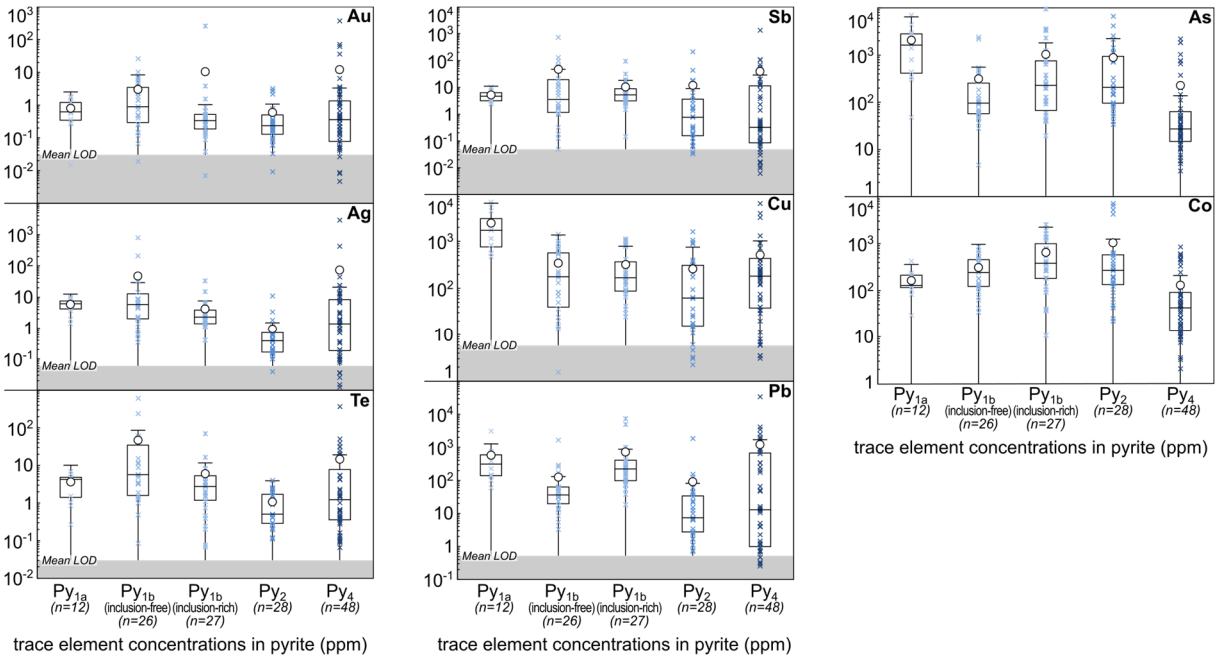

Figure 8: Box and whisker plots of some trace element concentrations of the various generations of pyrite from the Galat Sufar South gold deposit, northeastern Sudan. Analyses are grouped by pyrite generations. Py_{1b} free of mineral inclusion is distinguished from altered Py_{1b} grains with evidence of dissolution and with a Py_2 overgrowth rim. The number of analyses for each group of pyrite is given. Data below limit of detection (LOD) have been attributed the LOD/2 value. The median (line in the box), mean (white circle) and first and third quartile (box extent) values are shown as well as 1.5 times the interquartile range value (whiskers).

5.4.1. Py_{1a} and Py_{1b}

Py_{1a} and Py_{1b} generations display the highest Au, Ag and Te concentrations (up to 26.0, 793 and 238 ppm, respectively; Fig. 8). They can be distinguished by their Cu, Pb

and As concentrations which are higher for Py_{1a} than Py_{1b} (1740 *vs* 176 ppm, 304 *vs* 35.4 ppm and 1617 *vs* 95.9 ppm, respectively; Fig. 8). This is likely related to the increased amount of accessory sulphide minerals (chalcopyrite, galena, sphalerite, sulphosalt) in quartz-carbonate veinlets from D_{1aGSS} to D_{1bGSS} deformation stages (Fig. 2; Perret et al., 2020). D_{1aGSS}- and D_{1bGSS}-gold occurs as nano-inclusions or as structurally bound in pyrite lattice, as no gold micro-inclusion has been observed (subsection 5.1.) and no Au was measured for the corresponding ablation spots.

5.4.2. Py_2

At the grain scale, LA-ICP-MS elemental maps were made for a composite $Py_{1b/2}$ grain, previously investigated by EBSD (GS-22-08; Fig. 6). They highlight the relative depletion in Au, Ag and Te where Py_{1b} grains show evidence of dissolution, enclose numerous mineral inclusions and with a Py_2 overgrowth rim which is also depleted in these elements (Fig. 9). This trend is confirmed by the overall spot dataset (Fig. 8). Outliers with high Au concentrations (up to 260 ppm) may represent a nugget effect related to gold micro-inclusions (Fig. 4f) or gold associated with sulphide mineral inclusions in altered Py_{1b} cores such as chalcopyrite (Fig. 9). Ag and Te also appear to be preferentially incorporated in these mineral inclusions (Fig. 9). Sb, Cu and Pb show a different behaviour as Py_{1b} grains are slightly enriched where the core of the pyrite grain is altered (Figs. 8, 9). The Sb- and Cu-bearing mineral inclusions in altered cores are clearly visible in both petrographic analyses (Fig. 4e and f) and elemental maps (Fig. 9), and can be related to some outliers datapoints in Figure 8 (e.g. galena inclusions corresponding to samples showing Pb concentrations up to 7436 ppm). Similarly, where Py_{1b} grains are aggregated and annealed with interstitial chalcopyrite in a gold-bearing veinlet with dominant quartz and pyrite, metals are preferentially concentrated along pyrite subgrain boundaries and gold inclusions are formed in interstitial chalcopyrite (GS-34-05; Figs. 7b, 10). The remobilisation of Cu remains however limited as the Cu concentration is invariant whereas Au concentration decreases where Py_{1b} shows evidence

of dissolution (Fig. 8). On first hand, Py_2 overgrowths are free of mineral inclusions and exhibit lower concentrations of Sb, Cu and Pb regarding mineral inclusion-free Py_{1b} type (0.78 *vs* 3.60 ppm, 62.4 *vs* 176 ppm and 88.5 *vs* 122 ppm, respectively), similarly to Au, Ag and Te behaviour (Figs. 8, 9). On second hand, As and Co exhibit higher concentrations in Py_2 (207 and 270 ppm, respectively) than the portion of Py_{1b} free of mineral inclusions (95.9 and 245 ppm, respectively) (Fig. 8). Primary As and oscillatory zoning of Co in Py_{1b} grain are preserved despite its heavily altered aspect and the presence of a Py_2 rim (Fig. 9).

These data strongly suggest that Py_{1b} destabilisation, alteration and recrystallisation by annealing and Py_2 overgrowing are responsible for an overall release of Au-Ag-Te-(Sb-Cu-Pb). According to our observations, these elements seem to start migrating just before the *in situ* crystallisation of electrum-chalcopyrite-sulphosalt-(galena-arsenopyrite) minerals as inclusions in altered pyrite cores and interstitial sulphide assemblage forming along pyrite subgrain boundaries. This is in agreement with the previously published model for gold mobility, based on macroscopic to microscopic scale petrological-structural observations (Perret et al., 2020). This model suggests that the (D_{1aGSS})-D_{1bGSS} lattice-bound gold input event is followed by metal remobilisation and liberation of the main, free gold mineralisation during the D_{2GSS} deformation stage (Perret et al., 2020).

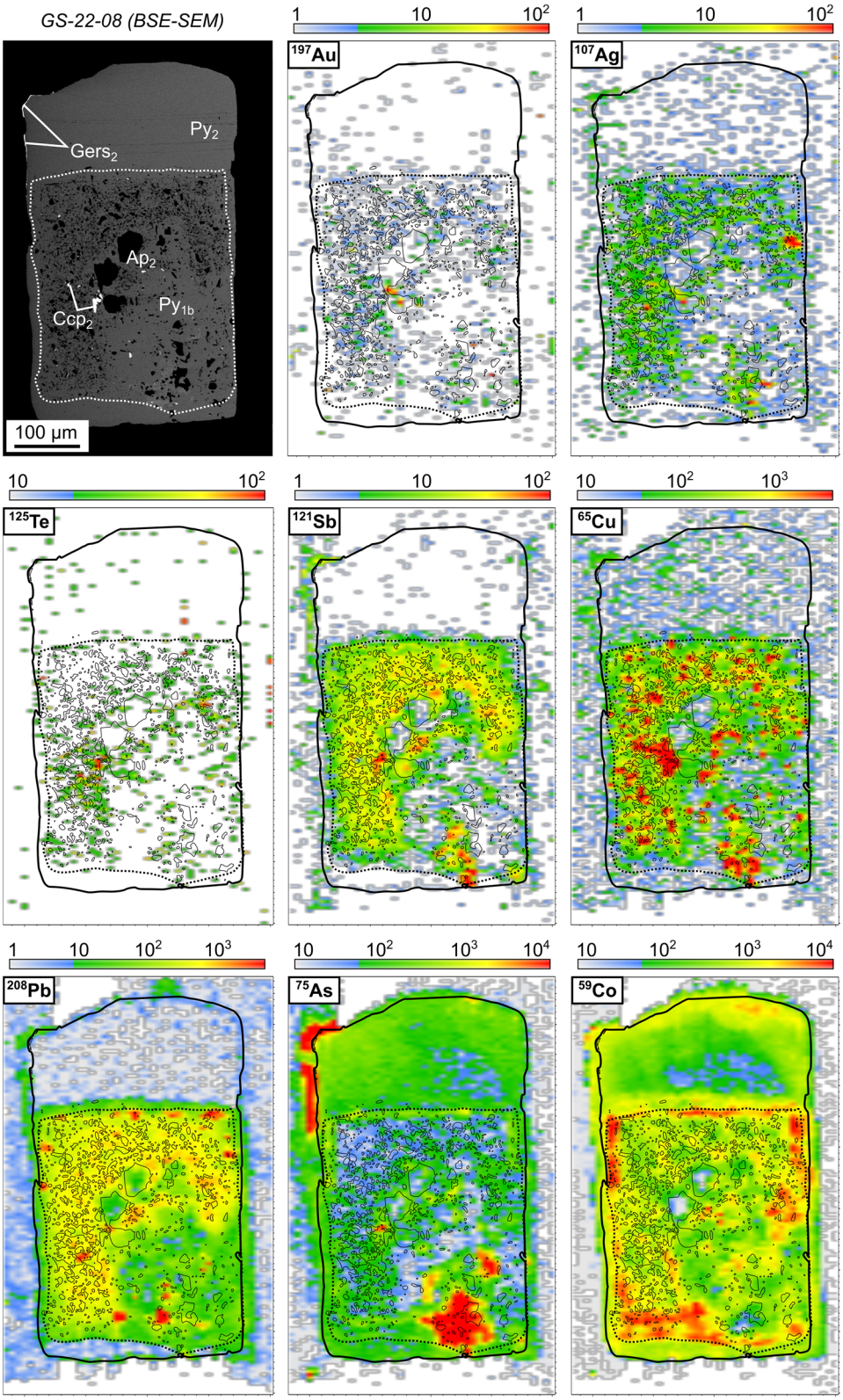

Figure 9: LA-ICP-MS trace element maps (Au, Ag, Te, Sb, Cu, Pb, As, Co) of a Py_{1b} altered core enclosing numerous mineral inclusions and with a Py_2 overgrowth (sample GS-22-08). The trace element concentration is semi-quantified (ppm) and illustrated by a colour log-scale. Mineral abbreviations are the same as in Figure 2.

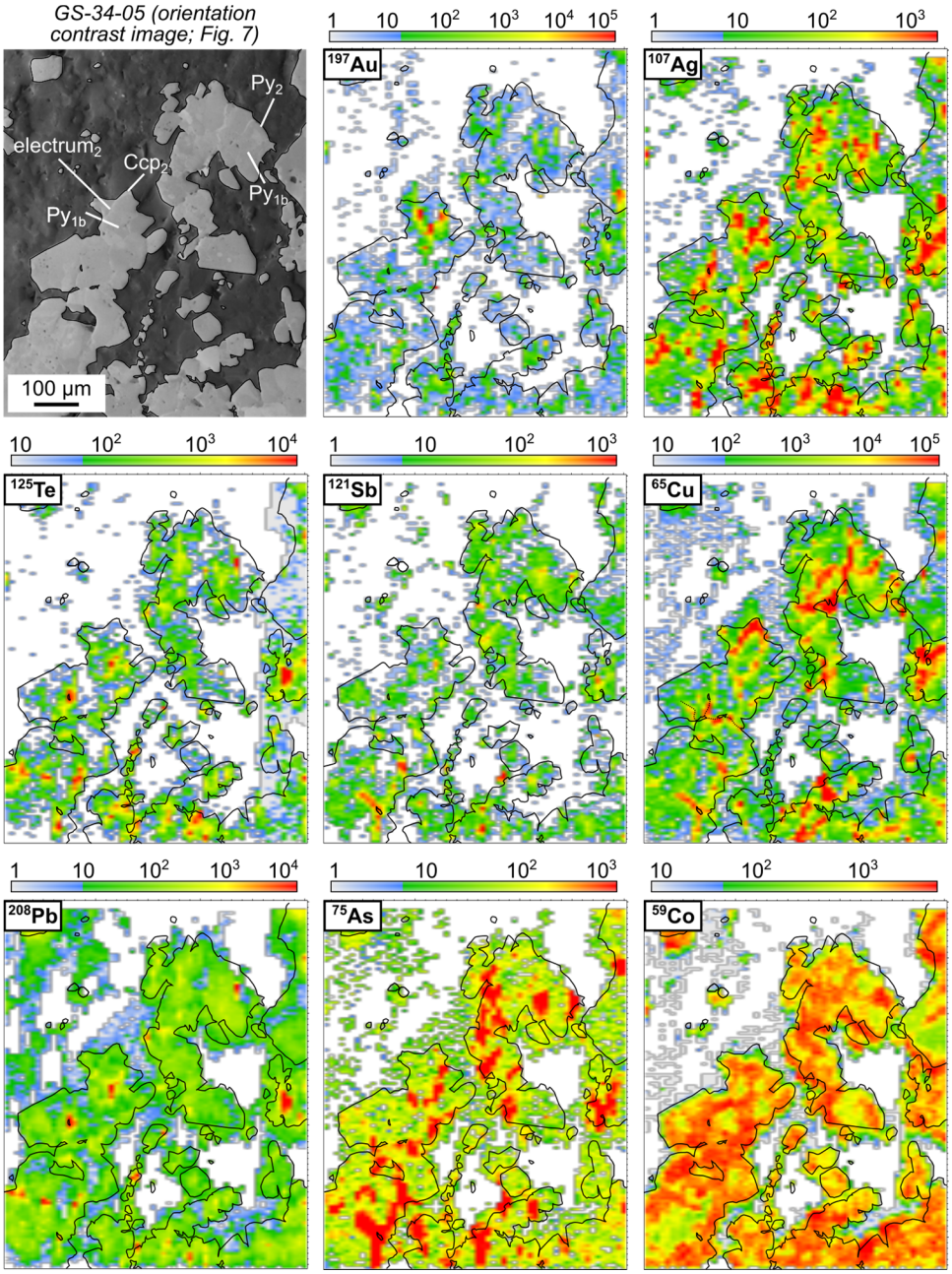

Figure 10: LA-ICP-MS trace element maps (Au, Ag, Te, Sb, Cu, Pb, As, Co) of a composite Py_{1b}-Py_2-Ccp_2-$electrum_2$ assemblage within a gold-bearing quartz-pyrite-(carbonate) veinlet (sample GS-34-05). The trace element concentration is semi-quantified (ppm) and illustrated by a colour log-scale. Mineral abbreviations are the same as in Figure 2.

5.4.3. Py_4

The Au, Ag, Te, Sb, Cu and Pb concentrations in Py_4 grains span a range of values that is similar to that measured for Py_{1a} to Py_2 generations, albeit with higher variability, illustrated by higher standard deviations (Fig. 8; Table 2). Outlier values for Au and As

concentrations may be linked to the presence of gold and sulphosalt micro-inclusions within pyrite grains (Figs. 4j and k, 8).

Unfortunately, rare studies focused on metal partitioning in hydrothermal systems and calculated partition coefficients for vapor-liquid fractionation (e.g. Pokrovski et al., 2008). Partition coefficients for metals between sulphide minerals remain unknown, but some studies attempted to interpret partitioning trends among coexisting base-metal-bearing sulphide minerals (e.g. Bortnikov et al., 2000; George et al., 2016, 2018), which leads to a *"predictive understanding of the fundamental crystal-structural controls on element partitioning into specific minerals"* (Cook et al., 2016). These studies investigated hydrothermal polymetallic deposits ranging from VMS, skarn, exhalative or porphyry-epithermal deposits formed in various thermodynamic conditions and coexisting sulphide minerals which differ from the ones characterised at the GSS gold deposit. Results are nevertheless consistent and we can approximate that, for minor and trace elements, Au preferentially gets enriched into pyrite, Co into sphalerite, Te-Ag-Bi into galena, As in both galena and sphalerite considering the D_{4GSS} sulphide mineral assemblage, apart from sulphosalts. The strong dispersion of the metal budget trapped by D_{4GSS}-related sulphide assemblage could therefore depend both on the composition of the *in situ* metallic stock it is sourced from, the partial remobilisation and partial or quantitative recrystallisation together with trace element partitioning between neoformed sulphide minerals. This would support the hypothesis stating that the D_{4GSS} gold event results from the remobilisation of former gold mineralisation at the GSS gold deposit, previously suggested from petrological-structural observations (Perret et al., 2020).

Elements	Si	S	V	Cr	Mn	Fe	Co	Ni	Cu	Zn	Ga	As	Se	Mo	Ag	Cd	In	Sn	Sb	Te	W	Au	Tl	Pb	Bi
Mean LOD	330	1000	0.21	1.3	0.44	58.0	0.19	4.3	5.8	1.24	0.06	1.04	4.5	0.19	0.06	0.16	0.02	0.26	0.05	0.40	0.06	0.03	0.01	0.50	0.02
	Py_{1a} *(n=12)*																								
Median	2463	545876	9.8	3.50	89.0	444134	129	109	1740	76.5	0.38	1617	8.2	0.93	6.2	0.58	0.02	0.18	4.7	4.3	0.18	0.62	0.08	304	0.33
Mean*	6691	542209	13.8	41.2	3675	440852	163	183	2453	1020	0.75	2042	10.5	1.9	5.8	4.7	0.03	0.38	5.2	3.6	0.48	0.79	0.13	568	0.47
SD*	8936	29562	17.1	102	11830	26123	100	207	2207	2362	1.2	2043	7.6	2.0	2.7	10.6	0.02	0.57	2.6	2.1	0.53	0.58	0.13	828	0.40
	Mineral inclusion-free Py_{1b} *(n=26)*																								
Median	637	542072	0.62	1.4	2.0	450294	245	348	176	9.8	0.04	95.9	7.3	0.11	5.9	0.08	0.02	0.16	3.6	5.6	0.15	0.89	0.04	35.4	0.61
Mean*	2958	542755	10.7	7.9	54.9	451890	309	378	344	101	0.47	313	12.3	0.36	48.0	0.98	0.02	0.19	47.1	46.0	3.5	3.0	1.4	122	1.0
SD*	6682	22017	33.4	19.7	218	22921	234	208	385	201	1.7	602	11.1	0.85	157	2.0	0.02	0.15	142	125	7.5	5.4	4.6	322	1.2
	Mineral inclusion-rich, altered Py_{1b} *(n=27)*																								
Median	3495	505019	8.1	13.8	148	479351	384	153	169	28.2	0.42	228	5.1	0.08	2.3	0.06	0.02	0.25	5.3	2.8	0.29	0.34	0.13	217	2.17
Mean*	4287	509377	22.5	29.6	311	477029	652	268	323	261	0.68	1032	6.4	0.42	4.2	0.77	0.02	0.64	10.5	5.9	4.8	10.4	0.86	709	1894
SD*	3109	33991	23.9	46.0	384	34204	662	355	354	711	0.61	2008	5.1	0.82	6.5	2.4	0.01	0.95	17.8	13.3	10.7	49.9	3.7	1635	9804
	Py_{2} *(n=28)*																								
Median	1095	542543	1.0	1.2	4.2	452346	270	418	62.4	5.0	0.09	207	7.0	0.16	0.38	0.08	0.01	0.17	0.78	0.50	0.16	0.24	0.02	7.1	0.25
Mean*	5766	533899 (	8.3	4.1	553	456691	1045	535	259	112	0.44	877	9.0	0.35	0.94	0.20	0.03	0.23	11.8	1.1	0.59	0.59	0.08	88.5	40.8
SD*	9144	34942	24.8	8.1	2560	32973	2003	510	397	269	1.2	1456	6.4	0.54	2.1	0.35	0.05	0.20	39.5	1.0	1.0	0.90	0.13	347	204
	Py_{4} *(n=48)*																								
Median	265	531593	0.21	0.54	1.8	450057	42.7	70.3	184	9.1	0.04	27.1	27.9	0.17	1.4	0.11	0.01	0.18	0.33	1.21	0.04	0.36	0.02	12.5	0.25
Mean*	6315	532650	7.5	0.92	38.0	456228	131	378	514	67.3	0.45	225	24.7	1.9	73.6	0.69	0.03	2.6	39.5	14.3	34.5	12.0	0.54	1192	107
SD*	18283	27277	38.5	0.87	126	24883	203	926	1142	200	1.2	504	18.7	5.1	417	2.4	0.07	13.2	193	53.2	203	55.1	1.6	4936	729

Concentrations are in ppm.

** Arithmetic means and standard deviations (SD) are calculated considering the LOD/2 value for <LOD values.*

Table 2: Summary of the LA-ICP-MS trace element concentrations (in ppm) of the various pyrite generations from the Galat Sufar South gold deposit, northeastern Sudan.

6. A holistic ore-forming model

6.1. Structural control on mineralisation

6.1.1. Insights into multiscale structural control on mineralisation

The coupling between EBSD and HRXCT results from this study with the petrological-structural study of Perret et al. (2020) suggests that structural control on mineralisation is consistently expressed at every scale at the GSS gold deposit (Fig. 11):

(i) The progressive nature of the ductile D_{1GSS}-D_{2GSS}-(D_{3GSS}) deformation episode is defined up to the crystallographic scale and observed shear sense remains the same at every scale;

(ii) Sulphide-rich ore shoots are oriented along the L_2 lineation from the deposit- to the microscopic scale, which corresponds to the dominant regional fabric. Structural control on mineralisation is therefore the same at every scale and we clearly illustrated that ore shoot geometry is fractal from the km-scale to the µm-scale.

Other studies attempted to couple regional- to macroscopic-scale 2D or 3D structural information with micro-characterisation of mineralised structures through HRXCT and/or EBSD, among other techniques (e.g. Kolb et al., 2003; Duclaux et al., 2013; Gazley et al., 2014a, 2014b; Sayab et al., 2020). Similarly to what we demonstrate in this study, this approach enables a better understanding of the mineralisation-related tectonic history, i.e. to what tectonic setting(s) is (are) the ore-forming event(s) genetically associated. This knowledge is very valuable, as it is crucial for greenfield exploration targeting and near-mine exploration (e.g. Groves et al., 2018; Cowan, 2020; Hronsky, 2020). For instance, at the GSS deposit, the gold mineralisation occurred during the ~ 750-700 Ma Atmur-Delgo suturing, expressed by D_{2GSS} deformation at the district scale (Schandelmeier et al., 1994; Perret et al., 2020). L_2-related structures are therefore pathfinders to GSS-like gold mineralisation throughout the Atmur-Delgo suture and nearby GSS gold deposit. Under-explored suture zones similar to the Atmur-Delgo suture

could also be considered as new exploration targets for vein-type gold deposits at the scale of the Arabian-Nubian shield.

Additionally, an accurate description of ore geometry, textures and paragenetic association at the microscopic scale helps discussing genetic models (e.g. Godel et al., 2010; Mateen et al., 2013; Vukmanovic et al., 2013; Dubosq et al., 2018; Spinks et al., 2021a, 2021b). It also allows for the evaluation of the feasibility of ore processing and adapt sheet flows (e.g. Reddy and Hough, 2013; Kyle and Ketcham, 2015; Sayab et al., 2016).

6.1.2. From field data to micro-analyses: representativeness and reliability on zooming in structural control

When studying deformed gold deposits, zooming from the district-scale structures up to microscopic sub-samples is a challenge. It may indeed be challenging to switch from 3D field observations and measurements to conventional 2D microstructural description of thin sections, leading to ambiguous interpretation of microtectonics (Sayab et al., 2014). The access to reconstructed 3D structural information at the microscopic and crystallographic scales *via* HRXCT and EBSD techniques is therefore of special interest for multiscale structural reconciliation.

However, it is worth noticing that 3D analyses, such as HRXCT and EBSD, are often performed on a limited number of samples, like in the present study, notably due to analytical costs. There may therefore be a lack of representativeness when zooming in which must be acknowledged. To limit this risk, it is mandatory to carry out in the first instance a very detailed petrographic study on available samples and to select the most representative ones on which 3D analyses will be performed. Finally, linking 3D structural information acquired from the field all the way to laboratory observations by ways of different methods helps better characterising the structural control on mineralisation (Fig. 11). It can be constrained from the tens of km- to the µm-scales,

while being cautious with the potential lack of representativeness of the microscopic-scale results. Finally, linking 3D structural information acquired from the field all the way to the laboratory observations by ways of different methods helps characterising in a more robust manner the structural control on mineralisation (Fig. 11). It can be constrained from the tens of km- to the µm-scales, while being aware of the potential lack of representativeness of the microscopic-scale results acquired.

6.2. Deformation-induced geochemical ore forming processes

6.2.1. Unravelling barren vs ore hydrothermal stages and ore targeting

Similarly to what has been widely documented for sulphide-bearing ore deposits (e.g. Sung et al., 2009; Zhao et al., 2011; Peterson and Mavrogenes, 2014; Velasquez et al., 2014; Genna and Gaboury, 2015; Belousov et al., 2016; Salvi et al., 2016; Augustin and Gaboury, 2018; Kerr et al., 2018; Gao et al., 2019; Wu et al., 2019a), the coupling between deposit-scale petrological-structural study, textural characterisation and LA-ICP-MS analyse of pyrite helps tracking gold endowment steps resulting in the formation of the GSS gold deposit (Fig. 11):

(i) Py_{1a} and Py_{1b} grains show the highest structurally-bound gold concentrations at the GSS gold deposit, accounting for <1 g/t Au grades along logged drill cores where Py_2 is absent. The (D_{1aGSS})-D_{1bGSS} deformation stages likely correspond to the first gold input to the system, occurring only as refractory gold, as suggested by former petrological-structural observations (Perret et al., 2020);

(ii) Where Py_2 occurs, the gold concentration decreases in altered Py_{1b} grains and microscopic-scale electrum inclusions are visible in pyrite cores and surrounding quartz, accounting for economic gold mineralisation (>1 g/t Au grades along logged drill cores). This observation shows that the D_{2GSS} deformation stage is likely responsible for gold

liberation from early Py_{1b}, in agreement with what was suggested from logging and conventional microscopy analysis (Perret et al., 2020);

(iii) Finally, the large span in trace element concentrations in Py_4 likely characterises partial remobilisation followed by partial or quantitative recrystallisation together with trace element partitioning between neoformed sulphide minerals. It confirms the discrete nature of the remobilisation of the D_{4GSS} deformation and gold episode that was inferred in a previous study (Perret et al., 2020).

LA-ICP-MS spot and map analyses therefore assess the mobility of lattice-bound trace elements in pyrite at the GSS gold deposit (Figs. 8, 9; Table 2). They confirm the relative contribution of the successive deformation-related hydrothermal episodes to the deposit-scale gold endowment. Ultimately, integrating such ore mineral geochemical data to the knowledge of the petrological-structural ore relationships and deposit-scale structural framework (Fig. 11) enables ore vectoring towards alteration haloes or mineralised structures, as already demonstrated in literature (e.g. Genna and Gaboury, 2015; Soltani Dehnavi et al., 2018; Soltani Dehnavi, 2019).

6.2.2. Insights into syn-metamorphic sulphide recrystallization and gold liberation

The coupling of LA-ICP-MS elemental maps (Figs. 9, 10, respectively) with EBSD maps (Figs. 6, 7, respectively) helps better constraining the influence of micro-deformation on elemental mobility in sulphide mineral assemblages through time at the GSS gold deposit.

At the microscopic scale, there is no mineral inclusion in Py_{1b} grains where Py_2 rim is absent. These mineral inclusions are thus not trapped during Py_{1b} growth. As such textures are characteristic of dissolution-precipitation mineral replacement (Putnis, 2002), it is more likely that the high-strain, ductile D_{2GSS} deformation stage is responsible for Py_{1b} destabilisation, alteration and recrystallisation by annealing and Py_2 overgrowing (Perret et al., 2020).the high-strain, ductile D_{2GSS} deformation stage is responsible for

Py_{1b} destabilisation, alteration and recrystallisation by annealing and Py_2 overgrowing (Perret et al., 2020). *In situ* trace element analyses support a remobilisation of Au-Ag-Te-(Sb-Cu-Pb) from Py_{1b} during this deformation stage. Likely, these elements only migrated over a few µm to cm distance before reprecipitating as electrum-chalcopyrite-sulphosalt-(galena-arsenopyrite) inclusions in altered pyrite cores and as interstitial sulphide assemblage along pyrite subgrain boundaries. LA-ICP-MS data confirm that the D_{2GSS} deformation stage is not related to an additional gold input, but rather to a release of lattice-bound gold together with polymetallic sulphide mineral formation (Perret et al., 2020).

A similar space-limited migration pattern for structurally compatible elements such as Cu, Pb or Zn, whereas other elements, like As, Co or Ni, remain immobile, have been demonstrated in the Naime Pyrite Member and at the Mt. Torrens Pb-Zn-Ag prospect, Kanmantoo Group, South Australia (Dakota Conn et al., 2019). Such trace element evolution pattern in pyrite is attributed to its recrystallisation under amphibolite facies metamorphism (Dakota Conn et al., 2019). The trace element concentrations in Py_2 thus suggest that D_{2GSS} deformation and mineralisation occurred under amphibolite facies metamorphic conditions at the GSS gold deposit, which is in agreement with the plastic deformation pressure-temperature field considered for pyrite (Barrie et al., 2009). Furthermore, multi-equilibria thermodynamic calculations confirmed that lower amphibolite-facies metamorphic conditions were reached during the D_{2GSS} deformation-mineralisation stage at the GSS gold deposit (Perret, 2021), which corresponds to regional peak metamorphism (Ahmed Suliman, 2000).

Combining deposit- to grain-scale 2D-3D structural information with ore textures and micro-chemical analyses of the ore-bearing minerals thus appears to be of prime importance when deciphering the deformation, metamorphic and geochemical ore formation-remobilisation and upgrading processes at the microscopic scale (Fig. 11; e.g. Huston et al., 1995; Morey et al., 2008; Gourcerol et al., 2018b; Pearce et al., 2018; Voute

et al., 2019; Cugerone et al., 2020; Combes et al., 2021). In that sense, more and more studies couple micro-textural or -structural ore characterisation *via* techniques such as HRXCT, 3D neutron tomography and EBSD with *in situ* geochemical analyses through hyperspectral X-ray computed tomography (e.g. Egan et al., 2015), X-ray fluorescence mapping (e.g. Fougerouse et al., 2016a), EMPA (e.g. Reddy and Hough, 2013; Wille et al., 2018), LA-ICP-MS (e.g. Dubosq et al., 2018), laser-induced breakdown spectroscopy (e.g. Cugerone et al., 2020) or nanoSIMS (e.g. Fougerouse et al., 2016b, 2021). To go further, constraining deformation-related ore-forming processes could even be extended up to the nanometric and sub-nanometric, atomic scales. This is possible thanks to the emergence of techniques such as the atom probe tomography that can image mineral defects, dislocations, *etc…* and better constrain micro-deformation processes (Reddy et al., 2020; Fougerouse et al., 2021). Systematically highlighting the relationships between microstructures and geochemical signatures of ore-related minerals would therefore represent a step forward towards a holistic laboratory approach for the study of deformed hydrothermal ore deposits.

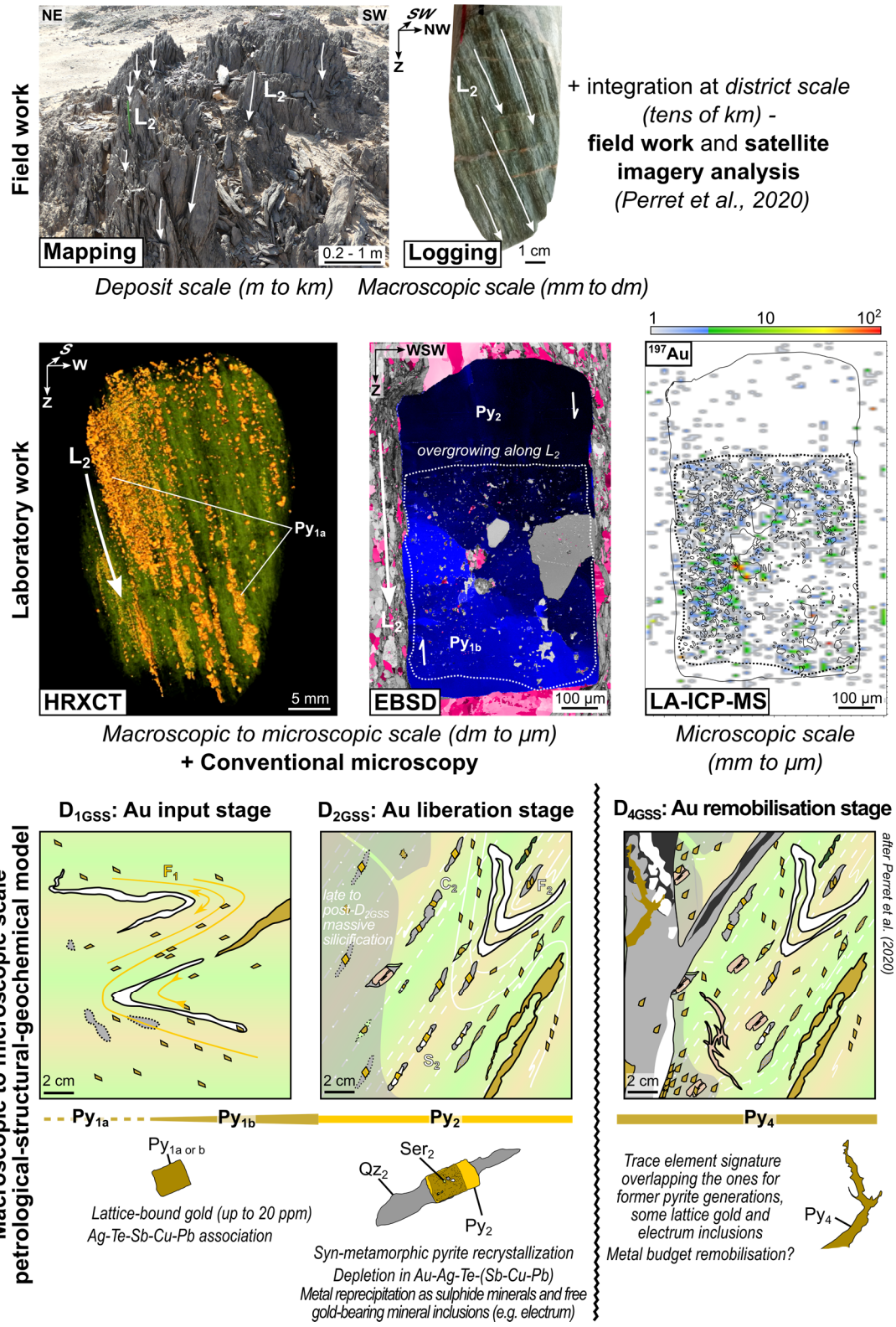

Figure 11: Insights from the suggested multiscale, multi-method approach for the understanding of the structural control defined by L_2 on gold mineralisation and deformation-induced geochemical ore-forming processes at the Galat Sufar South gold deposit, northeastern Sudan. Field and laboratory methods are separated, and their respective scale of investigation is indicated. Mineral abbreviations are the same as in Figure 2 for the petrological-structural cartoon.

7. Conclusions

The approach advocated here enables the characterisation of structural control on mineralisation and deformation-induced geochemical processes, which is critical in ore geology, especially when focusing on deformed ore deposits. It relies on (i) robust preliminary field and microscopy work, oriented sampling and conventional petrological-structural description of mineralisation from the district to the microscopic scales (GIS satellite imagery analysis, field and conventional microscopic observations) and (ii) coupling with multiple analytical methods in the laboratory. These are microstructural techniques such as high-resolution X-ray computed tomography (HRXCT) and electron back-scattered diffraction (EBSD) in addition to laser ablation inductively-coupled plasma mass spectrometry (LA-ICP-MS) on sulphide minerals.

Through the example of the Galat Sufar South gold deposit, Nubian shield, northeastern Sudan, we illustrate that this combined approach allows for the reconciliation of 3D structural records from the district scale up to the crystallographic scale. We unequivocally demonstrated that the structural control on mineralisation by the L_2 stretching lineation is indeed characterised at every scale, which enable to fully understand the geometry of the deposit and increase our level of confidence in attributing the formation of the Galat Sufar South gold deposit to hydrothermal fluid flows triggered during Atmur-Delgo suturing.

Furthermore, our approach enables the validation of micro-textural and -structural evolution of mineralisation-related sulphide mineral assemblages firstly inferred from conventional thin section investigation. The use of *in situ* geochemical methods, such as LA-ICP-MS on ore-related minerals, can help tracking geochemical changes associated with gold mineralising or remobilisation events coeval with syn-metamorphic deformation of ore-bearing mineral assemblages, characterised at the microscopic scale by EBSD. The trace element concentrations in the distinct pyrite generations distinguished at the Galat Sufar South gold deposit provide evidence for syn-deformation and -sulphide

recrystallisation metal mobility and gold liberation during the D_{2GSS} deformation stage. There, we clearly demonstrate the relationships between micro-deformation of sulphide minerals, gold mobility and lower-scale Atmur-Delgo suturing tectonics. The suggested approach therefore improves our understanding of the relationships between deformation, metamorphism, and geochemistry in ore-forming processes.

As a summary, our approach is therefore very promising for the study of deformed gold deposits and could be applied to any other sulphide-bearing, structurally controlled ore deposit type, in the wake of the increasing number of multiscale and -technique studies of ore deposits published the last decade. Such an approach leads leads to conclusive understanding of metallogenic processes but it is also key for mining industry, from greenfield exploration targeting to mining and ore processing.

Acknowledgements

The authors are grateful to the Orca Gold Inc. team and especially to Craig Hartshorne and Emmanuel Abanyin for their welcome on GSS camp and their substantial logistical support. Alexandre Flammang and John Moine (Lorraine University, France) as well as Christophe Nevado (Montpellier University, France) are warmly thanked for thin section preparation and careful re-polishing prior to EBSD analyses, respectively. Electron microscopy was carried out at the Service Commun de Microscopie Electronique et de Microanalyse X (Lorraine University, France). Blandine Gourcerol (BRGM, France) is acknowledged for introducing us with Matthew Leybourne (Queen's University, Canada), who is thanked for permission to carry out LA-ICP-MS analyses at Queen's Facility for Isotope Research. Marissa Valentino (Queen's University, Canada) is also thanked for her support with these analyses. An anonymous reviewer, D. Fougerouse and T. Torvela are warmly thanked for their comments that substantially helped improving the manuscript. This work is part of Julien Perret's PhD project which benefited of a CIFRE funding, reference CIFRE N°2017/1737, attributed by the French National Research and Technology Agency (ANRT).

References

Abdel-Rahman, E.M.A., 1993. Geochemical and geotectonic controls of the metallogenic evolution of selected ophiolite complexes from the Sudan. PhD Thesis. Berlin University.

Abdelsalam, M.G., Dawoud, A.S., 1991. The Kabus ophiolitic melange, Sudan, and its bearing on the western boundary of the Nubian Shield. Journal of the Geological Society 148, 83–92. https://doi.org/10.1144/gsjgs.148.1.0083

Abdelsalam, M.G., Stern, R.J., 1996a. Mapping Precambrian structures in the Sahara Desert with SIR-C/X-SAR radar: The Neoproterozoic Keraf Suture, NE Sudan. Journal of Geophysical Research: Planets 101, 23063–23076. https://doi.org/10.1029/96JE01391

Abdelsalam, M.G., Stern, R.J., 1996b. Sutures and shear zones in the Arabian-Nubian Shield. Journal of African Earth Sciences 23, 289–310. https://doi.org/10.1016/S0899-5362(97)00003-1

Abdelsalam, M.G., Stern, R.J., Copeland, P., Elfaki, E.M., Elhur, B., Ibrahim, F.M., 1998. The Neoproterozoic Keraf Suture in Ne Sudan: Sinistral Transpression Along the Eastern Margin of West Gondwana. The Journal of Geology 106, 133–148. https://doi.org/10.1086/516012

Abdelsalam, M.G., Stern, R.J., Schandelmeier, H., Sultan, M., 1995. Deformational History of the Neoproterozoic Keraf Zone in NE Sudan, Revealed by Shuttle Imaging Radar. The Journal of Geology 103, 475–491. https://doi.org/10.1086/629771

Adam, M.M.A., Lv, X., Abdel Rahman, A.A., Stern, R.J., Abdalrhman, A.A.A., Ullah, Z., 2020. In-situ sulfur isotope and trace element compositions of pyrite from the Neoproterozoic Haweit gold deposit, NE Sudan: Implications for the origin and source of the sulfur. Ore Geology Reviews 120, 103405. https://doi.org/10.1016/j.oregeorev.2020.103405

Ahmed Suliman, E.T.B., 2000. Keraf shear zone, NE Sudan: geodynamic characteristics of the Nile Craton - Nubian Shield boundary. PhD Thesis. Technischen Universität Berlin.

Allibone, A., Blakemore, H., Gane, J., Moore, J., MacKenzie, D., Craw, D., 2018. Contrasting Structural Styles of Orogenic Gold Deposits, Reefton Goldfield, New Zealand. Economic Geology 113, 1479–1497. https://doi.org/10.5382/econgeo.2018.4599

Allibone, A., Teasdale, J., Cameron, G., Etheridge, M., Uttley, P., Soboh, A., Appiah-Kubi, J., Adanu, A., Arthur, R., Mamphey, J., 2002. Timing and structural controls on gold mineralization at the Bogoso gold mine, Ghana, West Africa. Economic Geology 97, 949–969.

Almond, D.C., Ahmed, F., 1987. Ductile shear zones in the northern Red Sea Hills, Sudan and their implication for crustal collision. Geological Journal 22, 175–184. https://doi.org/10.1002/gj.3350220614

Ashley, P.M., Craw, D., 2004. Structural controls on hydrothermal alteration and gold-antimony mineralisation in the Hillgrove area, NSW, Australia. Mineralium Deposita 39, 223–239. https://doi.org/10.1007/s00126-003-0400-1

Augustin, J., Gaboury, D., 2019. Multi-stage and multi-sourced fluid and gold in the formation of orogenic gold deposits in the world-class Mana district of Burkina Faso – Revealed by LA-ICP-MS analysis of pyrites and arsenopyrites. Ore Geology Reviews 104, 495–521. https://doi.org/10.1016/j.oregeorev.2018.11.011

Bailo, T., Schandelmeier, H., Franz, G., Sun, C.-H., Stern, R.J., 2003. Plutonic and metamorphic rocks from the Keraf Suture (NE Sudan): a glimpse of Neoproterozoic tectonic evolution on the NE margin of W. Gondwana. Precambrian Research 123, 67–80.

Barrie, C.D., Boyle, A.P., Cook, N.J., Prior, D.J., 2010a. Pyrite deformation textures in the massive sulfide ore deposits of the Norwegian Caledonides. Tectonophysics 483, 269–286. https://doi.org/10.1016/j.tecto.2009.10.024

Barrie, C.D., Boyle, A.P., Salter, M., 2009. How low can you go?-Extending downwards the limits of plastic deformation in pyrite. Mineralogical Magazine 73, 895–913.

Barrie, C.D., Cook, N.J., Boyle, A.P., 2010b. Textural variation in the pyrite-rich ore deposits of the Røros district, Trondheim Region, Norway: implications for pyrite deformation mechanisms. Mineralium Deposita 45, 51–68. https://doi.org/10.1007/s00126-009-0261-3

Bayliss, P., 1977. Crystal structure refinement of a weakly anisotropic pyrite. American Mineralogist 62, 1168–1172.

Bayliss, P., 1968. The crystal structure of disordered gersdorffite. American Mineralogist: Journal of Earth and Planetary Materials 53, 290–293.

Belissont, R., Boiron, M.-C., Luais, B., Cathelineau, M., 2014. LA-ICP-MS analyses of minor and trace elements and bulk Ge isotopes in zoned Ge-rich sphalerites from the Noailhac – Saint-Salvy deposit (France): Insights into incorporation mechanisms and ore deposition processes. Geochimica et Cosmochimica Acta 126, 518–540. https://doi.org/10.1016/j.gca.2013.10.052

Belousov, I., Large, R.R., Meffre, S., Danyushevsky, L.V., Steadman, J., Beardsmore, T., 2016. Pyrite compositions from VHMS and orogenic Au deposits in the Yilgarn Craton, Western Australia: Implications for gold and copper exploration. Ore Geology Reviews 79, 474–499. https://doi.org/10.1016/j.oregeorev.2016.04.020

Berhe, S.M., 1990. Ophiolites in Northeast and East Africa: implications for Proterozoic crustal growth. Journal of the Geological Society 147, 41–57.

Blenkinsop, T.G., Doyle, M.G., 2014. Structural controls on gold mineralization on the margin of the Yilgarn craton, Albany–Fraser orogen: The Tropicana deposit, Western Australia. Journal of Structural Geology 67, 189–204. https://doi.org/10.1016/j.jsg.2014.01.013

Blenkinsop, T.G., Oliver, N.H.S., Dirks, P.G.H.M., Nugus, M., Tripp, G., Sanislav, I.V., 2020a. Structural Geology Applied to the Evaluation of Hydrothermal Gold Deposits. In: Rowland, J.V., Rhys, D.A. (Eds.), Applied Structural Geology of Ore-Forming Hydrothermal Systems, Reviews in Economic Geology. Society of Economic Geologists, Inc., 1–23.

Blenkinsop, T.G., Rowland, J.V., Baker, T., 2020b. Mechanical Regimes of Hydrothermal Gold Mineralization. In: Rowland, J.V., Rhys, D.A. (Eds.), Applied Structural Geology of Ore-Forming Hydrothermal Systems, Reviews in Economic Geology. Society of Economic Geologists, Inc., 205–214.

Bonnet, J., Mosser-Ruck, R., Caumon, M.-C., Rouer, O., Andre-Mayer, A.-S., Cauzid, J., Peiffert, C., 2016. Trace Element Distribution (Cu, Ga, Ge, Cd, and Fe) in Sphalerite From the Tennessee MVT Deposits, USA, By Combined EMPA, LA-ICP-MS, Raman Spectroscopy, and Crystallography. The Canadian Mineralogist 54, 1261–1284. https://doi.org/10.3749/canmin.1500104

Bortnikov, N.S., Cabri, L., Vikent ev, I.V., McMahon, G., Bogdanov, Y.A., 2000. Invisible gold in sulfides from recent submarine hydrothermal mounds. DOKLADY EARTH SCIENCES C/C OF DOKLADY-AKADEMIIA NAUK. INTERPERIODICA PUBLISHING, 863–866.

Boyle, A.P., Nelson, E., Hitzman, M., Churchill, J., Lopez-Pedrosa, M., Freitag, K., 2004. The use of electron backscatter diffraction and orientation contrast imaging as tools for sulphide textural studies: example from the Greens Creek deposit (Alaska). Mineralium Deposita 39, 103–113. https://doi.org/10.1007/s00126-003-0386-8

Bukovská, Z., Jeřábek, P., Morales, L.F.G., 2016. Major softening at brittle-ductile transition due to interplay between chemical and deformation processes: An insight from evolution of shear bands in the South Armorican Shear Zone. Journal of Geophysical Research: Solid Earth 121, 1158–1182. https://doi.org/10.1002/2015JB012319

Burke, K., Sengör, C., 1986. Tectonic escape in the evolution of the continental crust. In: Barazangi, M., Brown, L. (Eds.), Geodynamics Series. American Geophysical Union, Washington, D. C., 41–53. https://doi.org/10.1029/GD014p0041

Butler, I.B., Nesbitt, R.W., 1999. Trace element distributions in the chalcopyrite wall of a black smoker chimney: insights from laser ablation inductively coupled plasma mass spectrometry (LA–ICP–

MS). Earth and Planetary Science Letters 167, 335–345. https://doi.org/10.1016/S0012-821X(99)00038-2

Cavalcante, C., Lagoeiro, L., Fossen, H., Egydio-Silva, M., Morales, L.F.G., Ferreira, F., Conte, T., 2018. Temperature constraints on microfabric patterns in quartzofeldsphatic mylonites, Ribeira belt (SE Brazil). Journal of Structural Geology 115, 243–262. https://doi.org/10.1016/j.jsg.2018.07.013

Chauvet, A., 2019. Editorial for Special Issue "Structural Control of Mineral Deposits: Theory and Reality." Minerals 9, 171. https://doi.org/10.3390/min9030171

Chisambi, J., Von der Heyden, B., Tshibalanganda, M., Le Roux, S., 2020. Gold exploration in two and three dimensions: Improved and correlative insights from microscopy and X-ray computed tomography. Minerals 10, 476.

Combes, V., Eglinger, A., Andre-Mayer, A.-S., Teitler, Y., Heuret, A., Gibert, P., Béziat, D., 2021. Polyphase gold mineralisation at the Yaou deposit, French Guiana. Geological Society, London, Special Publications 516.

Cook, N., Ciobanu, C., George, L., Zhu, Z.-Y., Wade, B., Ehrig, K., 2016. Trace Element Analysis of Minerals in Magmatic-Hydrothermal Ores by Laser Ablation Inductively-Coupled Plasma Mass Spectrometry: Approaches and Opportunities. Minerals 6, 111. https://doi.org/10.3390/min6040111

Cook, N.J., Chryssoulis, S.L., 1990. Concentrations of invisible gold in the common sulfides. The Canadian Mineralogist 28, 1–16.

Cook, N.J., Ciobanu, C.L., Meria, D., Silcock, D., Wade, B., 2013. Arsenopyrite-pyrite association in an orogenic gold ore: Tracing mineralization history from textures and trace elements. Economic Geology 108, 1273–1283.

Cowan, E.J., 2020. Deposit-scale structural architecture of the Sigma-Lamaque gold deposit, Canada—insights from a newly proposed 3D method for assessing structural controls from drill hole data. Mineralium Deposita 55, 217–240. https://doi.org/10.1007/s00126-019-00949-6

Cox, S., Knackstedt, M., Braun, J., 2001. Principles of structural control on permeability and fluid flow in hydrothermal systems. In: Richards, J.P., Tosdal, R.M. (Eds.), Structural Controls on Ore Genesis, Reviews in Economic Geology. Society of Economic Geologists, Inc., 1–22.

Cox, S.F., 2016. Injection-Driven Swarm Seismicity and Permeability Enhancement: Implications for the Dynamics of Hydrothermal Ore Systems in High Fluid-Flux, Overpressured Faulting Regimes—An Invited Paper. Economic Geology 111, 559–587. https://doi.org/10.2113/econgeo.111.3.559

Cugerone, A., Cenki-Tok, B., Oliot, E., Muñoz, M., Barou, F., Motto-Ros, V., Le Goff, E., 2020. Redistribution of germanium during dynamic recrystallization of sphalerite. Geology 48, 236–241. https://doi.org/10.1130/G46791.1

Dakota Conn, C., Spry, P.G., Layton-Matthews, D., Voinot, A., Koenig, A., 2019. The effects of amphibolite facies metamorphism on the trace element composition of pyrite and pyrrhotite in the Cambrian Nairne Pyrite Member, Kanmantoo Group, South Australia. Ore Geology Reviews 114, 103128. https://doi.org/10.1016/j.oregeorev.2019.103128

Deditius, A.P., Reich, M., Kesler, S.E., Utsunomiya, S., Chryssoulis, S.L., Walshe, J., Ewing, R.C., 2014. The coupled geochemistry of Au and As in pyrite from hydrothermal ore deposits. Geochimica et Cosmochimica Acta 140, 644–670. https://doi.org/10.1016/j.gca.2014.05.045

Deditius, A.P., Utsunomiya, S., Ewing, R.C., Chryssoulis, S.L., Venter, D., Kesler, S.E., 2009. Decoupled geochemical behavior of As and Cu in hydrothermal systems. Geology 37, 707–710. https://doi.org/10.1130/G25781A.1

Denkler, T., Franz, G., Schandelmeier, H., Darbyshire, D.P.F., Harms, U., Pilot, J., 1993. Evolution of the south-western part of the Atmur-Delgo suture. Geoscientific Research in Northeast Africa. Balkema Rotterdam, 87–89.

Dhawan, N., Safarzadeh, M.S., Miller, J.D., Moats, M.S., Rajamani, R.K., Lin, C.-L., 2012. Recent advances in the application of X-ray computed tomography in the analysis of heap leaching systems. Minerals Engineering 35, 75–86. https://doi.org/10.1016/j.mineng.2012.03.033

Dubosq, R., Lawley, C.J.M., Rogowitz, A., Schneider, D.A., Jackson, S., 2018. Pyrite deformation and connections to gold mobility: Insight from micro-structural analysis and trace element mapping. Lithos 310–311, 86–104. https://doi.org/10.1016/j.lithos.2018.03.024

Duckworth, G., 2018. Feasibility study - NI 43-101 TECHNICAL REPORT - Block 14 gold project. NI 43-101 TECHNICAL REPORT. Lycopodium Minerals Pty Ltd.

Duclaux, G., Hough, R., Gazley, M., Fisher, L., Walshe, J., Cleverley, J., 2013. A multi-scale approach to hydrothermal gold systems: unravelling mineralisation processes at Plutonic Gold Mine. World Gold Conference, Brisbane. 26–29.

Egan, C.K., Jacques, S.D.M., Wilson, M.D., Veale, M.C., Seller, P., Beale, A.M., Pattrick, R.A.D., Withers, P.J., Cernik, R.J., 2015. 3D chemical imaging in the laboratory by hyperspectral X-ray computed tomography. Scientific Reports 5, 1–9. https://doi.org/10.1038/srep15979

Faleiros, F.M., da Cruz Campanha, G.A., da Silveira Bello, R.M., Fuzikawa, K., 2007. Fault–valve action and vein development during strike–slip faulting: An example from the Ribeira Shear Zone, Southeastern Brazil. Tectonophysics 438, 1–32.

Finch, E.G. Tomkins, A.G., 2017. Pyrite-Pyrrhotite Stability in a Metamorphic Aureole: Implications for Orogenic Gold Genesis. Economic Geology 112, 661–674. https://doi.org/10.2113/econgeo.112.3.661

Fougerouse, Denis, Micklethwaite, S., Tomkins, A.G., Mei, Y., Kilburn, M., Guagliardo, P., Fisher, L.A., Halfpenny, A., Gee, M., Paterson, D., Howard, D.L., 2016a. Gold remobilisation and formation of high grade ore shoots driven by dissolution-reprecipitation replacement and Ni substitution into auriferous arsenopyrite. Geochimica et Cosmochimica Acta 178, 143–159. https://doi.org/10.1016/j.gca.2016.01.040

Fougerouse, D., Micklethwaite, S., Halfpenny, A., Reddy, S.M., Cliff, J.B., Martin, L.A.J., Kilburn, M., Guagliardo, P., Ulrich, S., 2016b. The golden ark: arsenopyrite crystal plasticity and the retention of gold through high strain and metamorphism. Terra Nova 28, 181–187.

Fougerouse, Denis, Reddy, S.M., Saxey, D.W., Rickard, W.D., Van Riessen, A., Micklethwaite, S., 2016c. Nanoscale gold clusters in arsenopyrite controlled by growth rate not concentration: Evidence from atom probe microscopy. American Mineralogist 101, 1916–1919.

Fougerouse, D., Micklethwaite, S., Ulrich, S., Miller, J., Godel, B., Adams, D.T., McCuaig, T.C., 2017. Evidence for Two Stages of Mineralization in West Africa's Largest Gold Deposit: Obuasi, Ghana. Economic Geology 112, 3–22. https://doi.org/10.2113/econgeo.112.1.3

Fougerouse, D., Reddy, S.M., Aylmore, M., Yang, L., Guagliardo, P., Saxey, D.W., Rickard, W.D.A., Timms, N., 2021. A new kind of invisible gold in pyrite hosted in deformation-related dislocations. Geology. https://doi.org/10.1130/G49028.1

Frenzel, M., Hirsch, T., Gutzmer, J., 2016. Gallium, germanium, indium, and other trace and minor elements in sphalerite as a function of deposit type — A meta-analysis. Ore Geology Reviews 76, 52–78. https://doi.org/10.1016/j.oregeorev.2015.12.017

Frisch, W., Pohl, W., 1986. Petrochemistry of some mafic and ultramafic rocks from the Mozambique Belt, SE Kenya. Mitteilungen Der Osterreichischen Geologischen Gesellschaft 78, 97–114.

Fritz, H., Abdelsalam, M., Ali, K.A., Bingen, B., Collins, A.S., Fowler, A.R., Ghebreab, W., Hauzenberger, C.A., Johnson, P.R., Kusky, T.M., Macey, P., Muhongo, S., Stern, R.J., Viola, G., 2013. Orogen styles in the East African Orogen: A review of the Neoproterozoic to Cambrian tectonic evolution. Journal of African Earth Sciences 86, 65–106. https://doi.org/10.1016/j.jafrearsci.2013.06.004

Gaboury, D., Nabil, H., Ennaciri, A., Maacha, L., 2020. Structural setting and fluid composition of gold mineralization along the central segment of the Keraf suture, Neoproterozoic Nubian Shield,

Sudan: implications for the source of gold. International Geology Review 1–27. https://doi.org/10.1080/00206814.2020.1838336

Gaboury, D., Oré Sanchez, C., 2020. Electrochemical gold precipitation to explain extensive vertical and lateral mineralization in the world-class Poderosa-Pataz district, Peru. Terra Nova 32, 97–107. https://doi.org/10.1111/ter.12440

Gaillard, N., Williams-Jones, A.E., Clark, J.R., Salvi, S., Perrouty, S., Linnen, R.L., Olivo, G.R., 2020. The use of lithogeochemistry in delineating hydrothermal fluid pathways and vectoring towards gold mineralization in the Malartic district, Québec. Ore Geology Reviews 120, 103351. https://doi.org/10.1016/j.oregeorev.2020.103351

Galkin, S.V., Efimov, A.A., Krivoshchekov, S.N., Savitskiy, Y.V., Cherepanov, S.S., 2015. X-ray tomography in petrophysical studies of core samples from oil and gas fields. Russian Geology and Geophysics 56, 782–792.

Gamal El Dien, H., Arai, S., Doucet, L.-S., Li, Z.-X., Kil, Y., Fougerouse, D., Reddy, S.M., Saxey, D.W., Hamdy, M., 2019. Cr-spinel records metasomatism not petrogenesis of mantle rocks. Nature Communications 10, 5103. https://doi.org/10.1038/s41467-019-13117-1

Gao, F., Du, Yangsong, Pang, Z., Du, Yilun, Xin, F., Xie, J., 2019. LA-ICP-MS Trace-Element Analysis of Pyrite from the Huanxiangwa Gold Deposit, Xiong'ershan District, China: Implications for Ore Genesis. Minerals 9, 157. https://doi.org/10.3390/min9030157

Gazley, M., Duclaux, G., Fisher, L., Hough, R., 2014. Multiscale controls on gold mineralisation at Plutonic Gold Mine, Marymia Inlier, Western Australia. Australian Earth Sciences Convention, Newcastle. 7–10.

Gazley, M.F., Pearce, M.A., Fisher, L.A., Duclaux, G., Cleverley, J.S., Hough, R.M., 2014. Multi-scale advanced characterisation of gold mineralising systems. Presented at the AusIMM New Zealand Branch Annual Conference 2014, 263–270.

Genna, D., Gaboury, D., 2015. Deciphering the Hydrothermal Evolution of a VMS System by LA-ICP-MS Using Trace Elements in Pyrite: An Example from the Bracemac-McLeod Deposits, Abitibi, Canada, and Implications for Exploration. Economic Geology 110, 2087–2108. https://doi.org/10.2113/econgeo.110.8.2087

George, L.L., Cook, N.J., Ciobanu, C.L., 2016. Partitioning of trace elements in co-crystallized sphalerite–galena–chalcopyrite hydrothermal ores. Ore Geology Reviews 77, 97–116. https://doi.org/10.1016/j.oregeorev.2016.02.009

George, L.L., Cook, N.J., Crowe, B.B.P., Ciobanu, C.L., 2018. Trace elements in hydrothermal chalcopyrite. Mineralogical Magazine 82, 59–88. https://doi.org/10.1180/minmag.2017.081.021

Gill, S.B., Piercey, S.J., Layton-Matthews, D., 2016. Mineralogy and Metal Zoning of the Cambrian Zn-Pb-Cu-Ag-Au Lemarchant Volcanogenic Massive Sulfide (VMS) Deposit, Newfoundland. The Canadian Mineralogist 54, 1307–1344. https://doi.org/10.3749/canmin.1500069

Godel, B., 2013. High-Resolution X-Ray Computed Tomography and Its Application to Ore Deposits: From Data Acquisition to Quantitative Three-Dimensional Measurements with Case Studies from Ni-Cu-PGE Deposits. Economic Geology 108, 2005–2019. https://doi.org/10.2113/econgeo.108.8.2005

Godel, B., Barnes, S.J., Barnes, S.-J., Maier, W.D., 2010. Platinum ore in three dimensions: Insights from high-resolution X-ray computed tomography. Geology 38, 1127–1130.

Godel, B.M., Barnes, S.J., Barnes, S.-J., 2013. Deposition Mechanisms of Magmatic Sulphide Liquids: Evidence from High-Resolution X-Ray Computed Tomography and Trace Element Chemistry of Komatiite-hosted Disseminated Sulphides. Journal of Petrology 54, 1455–1481. https://doi.org/10.1093/petrology/egt018

Goswami, S., Mamtani, M.A., Rana, V., 2018. Quartz CPO and kinematic analysis in deformed rocks devoid of visible stretching lineations: An integrated AMS and EBSD investigation. Journal of Structural Geology 115, 270–283. https://doi.org/10.1016/j.jsg.2018.04.008

Gourcerol, B., Kontak, D.J., Petrus, J.A., Thurston, P.C., 2020. Application of LA ICP-MS analysis of arsenopyrite to gold metallogeny of the Meguma Terrane, Nova Scotia, Canada. Gondwana Research 81, 265–290. https://doi.org/10.1016/j.gr.2019.11.011

Gourcerol, B., Kontak, D.J., Thurston, P.C., Petrus, J.A., 2018a. Results of LA-ICP-MS sulfide mapping from Algoma-type BIF gold systems with implications for the nature of mineralizing fluids, metal sources, and deposit models. Mineralium Deposita 53, 871–894.

Gourcerol, B., Kontak, D.J., Thurston, P.C., Petrus, J.A., 2018b. Application of LA-ICP-MS sulfide analysis and methodology for deciphering elemental paragenesis and associations in addition to multi-stage processes in metamorphic gold settings. The Canadian Mineralogist 56, 39–64.

Grenholm, M., 2019. The global tectonic context of the ca. 2.27-1.96 Ga Birimian Orogen – Insights from comparative studies, with implications for supercontinent cycles. Earth-Science Reviews 193, 260–298. https://doi.org/10.1016/j.earscirev.2019.04.017

Grimshaw, M., Chapman, R.J., Pearce, M.A., 2017. Characterisation of the crystallography of gold using EBSD. Applied Earth Science 126, 60–61.

Groves, D.I., Santosh, M., Goldfarb, R.J., Zhang, L., 2018. Structural geometry of orogenic gold deposits: Implications for exploration of world-class and giant deposits. Geoscience Frontiers 9, 1163–1177. https://doi.org/10.1016/j.gsf.2018.01.006

Halfpenny, A., Hough, R., Nugus, M., 2013. Crystallography of Natural and Synthetic Gold Alloy Microstructures. Materials Science Forum 753, 477–480. https://doi.org/10.4028/www.scientific.net/MSF.753.477

Hanna, R.D., Ketcham, R.A., 2017. X-ray computed tomography of planetary materials: A primer and review of recent studies. Geochemistry 77, 547–572. https://doi.org/10.1016/j.chemer.2017.01.006

Harms, U., Darbyshire, D.P.F., Denkler, T., Hengst, M., Schandelmeier, H., 1994. Evolution of the Neoproterozoic Delgo suture zone and crustal growth in northern Sudan: geochemical and radiogenic isotope constraints. Geologische Rundschau 83, 591–603.

Hazarika, P., Mishra, B., Chinnasamy, S.S., Bernhardt, H.-J., 2013. Multi-stage growth and invisible gold distribution in pyrite from the Kundarkocha sediment-hosted gold deposit, eastern India. Ore Geology Reviews 55, 134–145.

Hough, R.M., Noble, R.R.P., Reich, M., 2011. Natural gold nanoparticles. Ore Geology Reviews 42, 55–61. https://doi.org/10.1016/j.oregeorev.2011.07.003

Howell, E.R., Blakey, R.C., 2013. Sedimentological constraints on the evolution of the Cordilleran arc: New insights from the Sonsela Member, Upper Triassic Chinle Formation, Petrified Forest National Park (Arizona, USA). Geological Society of America Bulletin 125, 1349–1368. https://doi.org/10.1130/B30714.1

Hronsky, J.M.A., 2020. Deposit-scale structural controls on orogenic gold deposits: an integrated, physical process–based hypothesis and practical targeting implications. Mineralium Deposita 55, 197–216. https://doi.org/10.1007/s00126-019-00918-z

Huston, D.L., Sie, S.H., Suter, G.F., Cooke, D.R., Both, R.A., 1995. Trace elements in sulfide minerals from eastern Australian volcanic-hosted massive sulfide deposits; Part I, Proton microprobe analyses of pyrite, chalcopyrite, and sphalerite, and Part II, Selenium levels in pyrite; comparison with delta 34 S values and implications for the source of sulfur in volcanogenic hydrothermal systems. Economic Geology 90, 1167–1196. https://doi.org/10.2113/gsecongeo.90.5.1167

Jochum, K.P., Willbold, M., Raczek, I., Stoll, B., Herwig, K., 2005. Chemical Characterisation of the USGS Reference Glasses GSA-1G, GSC-1G, GSD-1G, GSE-1G, BCR-2G, BHVO-2G and BIR-1G Using EPMA, ID-TIMS, ID-ICP-MS and LA-ICP-MS. Geostandards and Geoanalytical Research 29, 285–302.

Johnson, P.R., Andresen, A., Collins, A.S., Fowler, A.R., Fritz, H., Ghebreab, W., Kusky, T., Stern, R.J., 2011. Late Cryogenian–Ediacaran history of the Arabian–Nubian Shield: A review of depositional,

plutonic, structural, and tectonic events in the closing stages of the northern East African Orogen. Journal of African Earth Sciences 61, 167–232. https://doi.org/10.1016/j.jafrearsci.2011.07.003

Johnson, P.R., Woldehaimanot, B., 2003. Development of the Arabian-Nubian Shield: perspectives on accretion and deformation in the northern East African Orogen and the assembly of Gondwana. Geological Society, London, Special Publications 206, 289–325. https://doi.org/10.1144/GSL.SP.2003.206.01.15

Johnson, P.R., Zoheir, B.A., Ghebreab, W., Stern, R.J., Barrie, C.T., Hammer, R.D., 2017. Gold-bearing volcanogenic massive sulfides and orogenic-gold deposits in the Nubian Shield. South African Journal of Geology 120, 63–76.

Kadel-Harder, I.M., Spry, P.G., Layton-Matthews, D., Voinot, A., von der Handt, A., McCombs, A.L., 2020. Paragenetic relationships between low- and high-grade gold mineralization in the Cripple Creek Au-Te deposit, Colorado: Trace element studies of pyrite. Ore Geology Reviews 127, 103847. https://doi.org/10.1016/j.oregeorev.2020.103847

Kahl, W.-A., Dilissen, N., Hidas, K., Garrido, C.J., LÓPEZ-SÁNCHEZ-VIZCAÍNO, V., ROMÁN-ALPISTE, M., 2017. 3-D microstructure of olivine in complex geological materials reconstructed by correlative X-ray-CT and EBSD analyses. Journal of Microscopy 268, 193–207.

Keith, M., Häckel, F., Haase, K.M., Schwarz-Schampera, U., Klemd, R., 2016. Trace element systematics of pyrite from submarine hydrothermal vents. Ore Geology Reviews 72, 728–745. https://doi.org/10.1016/j.oregeorev.2015.07.012

Keith, M., Smith, D.J., Jenkin, G.R.T., Holwell, D.A., Dye, M.D., 2018. A review of Te and Se systematics in hydrothermal pyrite from precious metal deposits: Insights into ore-forming processes. Ore Geology Reviews 96, 269–282. https://doi.org/10.1016/j.oregeorev.2017.07.023

Kerr, M.J., Hanley, J.J., Kontak, D.J., Morrison, G.G., Petrus, J., Fayek, M., Zajacz, Z., 2018. Evidence of upgrading of gold tenor in an orogenic quartz-carbonate vein system by late magmatic-hydrothermal fluids at the Madrid Deposit, Hope Bay Greenstone Belt, Nunavut, Canada. Geochimica et Cosmochimica Acta 241, 180–218. https://doi.org/10.1016/j.gca.2018.08.030

Kolb, J., Kisters, A.F.M., Meyer, F.M., Siemes, H., 2003. Polyphase deformation of mylonites from the Renco gold mine (Zimbabwe): identi®ed by crystallographic preferred orientation of quartz. Journal of Structural Geology 10.

Kontak, D., Hanley, J.J., Gourcerol, B., Petrus, J., Malcom, K., Kerr, M., Kelly, C., Letourneau, M., Mcdivitt, J., Neyedley, K., 2018. Protracted and complex fluid histories the norm in orogenic-type gold deposits as revealed by LA ICP-MS sulfide mapping. Proceedings of the Resources for Future Generations 2018 Meeting. Presented at the Resources for Future Generations, Vancouver.

Kusky, T.M., Abdelsalam, M., Tucker, R.D., Stern, R.J., 2003. Evolution of the East African and related orogens, and the assembly of Gondwana. Precambrian Research 123, 81–85. https://doi.org/10.1016/S0301-9268(03)00062-7

Kyle, J.R., Ketcham, R.A., 2015. Application of high resolution X-ray computed tomography to mineral deposit origin, evaluation, and processing. Ore Geology Reviews 65, 821–839. https://doi.org/10.1016/j.oregeorev.2014.09.034

Kyle, J.R., Ketcham, R.A., 2003. IN SITU DISTRIBUTION OF GOLD IN ORES USING HIGH-RESOLUTION X-RAY COMPUTED TOMOGRAPHY. Economic Geology 98, 1697–1701.

Large, R.R., Bull, S.W., Maslennikov, V.V., 2011. A Carbonaceous Sedimentary Source-Rock Model for Carlin-Type and Orogenic Gold Deposits. Economic Geology 106, 331–358. https://doi.org/10.2113/econgeo.106.3.331

Large, R.R., Danyushevsky, L., Hollit, C., Maslennikov, V., Meffre, S., Gilbert, S., Bull, S., Scott, R., Emsbo, P., Thomas, H., Singh, B., Foster, J., 2009. Gold and Trace Element Zonation in Pyrite Using a Laser Imaging Technique: Implications for the Timing of Gold in Orogenic and Carlin-Style Sediment-Hosted Deposits. Economic Geology 104, 635–668. https://doi.org/10.2113/gsecongeo.104.5.635

Large, R.R., Maslennikov, V.V., 2020. Invisible Gold Paragenesis and Geochemistry in Pyrite from Orogenic and Sediment-Hosted Gold Deposits. Minerals 10, 339. https://doi.org/10.3390/min10040339

Large, R.R., Maslennikov, V.V., Robert, F., Danyushevsky, L.V., Chang, Z., 2007. Multistage Sedimentary and Metamorphic Origin of Pyrite and Gold in the Giant Sukhoi Log Deposit, Lena Gold Province, Russia. Economic Geology 102, 1233–1267. https://doi.org/10.2113/gsecongeo.102.7.1233

Li, W., Cook, N.J., Xie, G.-Q., Mao, J.-W., Ciobanu, C.L., Li, J.-W., Zhang, Z.-Y., 2019. Textures and trace element signatures of pyrite and arsenopyrite from the Gutaishan Au–Sb deposit, South China. Mineralium Deposita 54, 591–610. https://doi.org/10.1007/s00126-018-0826-0

Maslennikov, V.V., Maslennikova, S.P., Large, R.R., Danyushevsky, L.V., 2009. Study of Trace Element Zonation in Vent Chimneys from the Silurian Yaman-Kasy Volcanic-Hosted Massive Sulfide Deposit (Southern Urals, Russia) Using Laser Ablation-Inductively Coupled Plasma Mass Spectrometry (LA-ICPMS). Economic Geology 104, 1111–1141. https://doi.org/10.2113/gsecongeo.104.8.1111

Masson, F.-X., Beaudoin, G., Laurendeau, D., 2020. Quantification of the morphology of gold grains in 3D using X-ray microscopy and SEM photogrammetry. Journal of Sedimentary Research 90, 286–296. https://doi.org/10.2110/jsr.2020.16

Masurel, Q., Thébaud, N., Miller, J., Ulrich, S., Hein, K.A.A., Cameron, G., Béziat, D., Bruguier, O., Davis, J.A., 2017. Sadiola Hill: A World-Class Carbonate-Hosted Gold Deposit in Mali, West Africa. Economic Geology 112, 23–47. https://doi.org/10.2113/econgeo.112.1.23

Mateen, T., Rehman, H.U., Yamamoto, H., 2013. EBSD study of Quartz c-axis orientations in the silicified host rocks of the Kasuga gold deposit, Southwest Japan. Journal of Mineralogical and Petrological Sciences 108, 278–287. https://doi.org/10.2465/jmps.130118b

McCaffrey, K., Lonergan, Lidia, Wilkinson, J., Lonergan, Leonard (Eds.), 1999. Fractures, fluid flow and mineralization, Special Publications. Geological Society of London.

Meng, Y.-M., Jébrak, M., Sasseville, C., Huang, X.-W., 2020. Geochemical and mineralogical diagnosis on gold ores: A case study from the Cadillac–Larder Lake Fault Zone, Abitibi, Canada. Ore Geology Reviews 103840.

Miller, J.D., Lin, C.L., Garcia, C., Arias, H., 2003. Ultimate recovery in heap leaching operations as established from mineral exposure analysis by X-ray microtomography. International Journal of Mineral Processing 72, 331–340. https://doi.org/10.1016/S0301-7516(03)00091-7

Monteiro, R.N., Fyfe, W.S., Chemale, F., 2004. The impact of the linkage between grade distribution and petrofabric on the understanding of structurally controlled mineral deposits: Ouro Fino Gold Mine, Brazil. Journal of Structural Geology 26, 1195–1214. https://doi.org/10.1016/j.jsg.2003.11.023

Morey, A.A., Tomkins, A.G., Bierlein, F.P., Weinberg, R.F., Davidson, G.J., 2008. Bimodal distribution of gold in pyrite and arsenopyrite: Examples from the Archean Boorara and Bardoc shear systems, Yilgarn craton, Western Australia. Economic Geology 103, 599–614.

Morlot, C., Pignatelli, I., Giuliani, G., Sterpenich, J., Boiron, M.C., Ohnenstetter, D., Andriamamonjy, A., Raoul, J., Chatagner, P.Y., 2016. La tomographie de rayons X et ses applications en géologie: exemples de l'émeraude trapiche et du grenat démantoïde. Revue de Gemmologie AFG 198, 13–18.

Mosley, P.N., 1993. Geological evolution of the late Proterozoic "Mozambique Belt" of Kenya. Tectonophysics 221, 223–250.

Paton, C., Hellstrom, J., Paul, B., Woodhead, J., Hergt, J., 2011. Iolite: Freeware for the visualisation and processing of mass spectrometric data. Journal of Analytical Atomic Spectrometry 26, 2508–2518.

Pearce, M.A., Godel, B.M., Fisher, L.A., Schoneveld, L.E., Cleverley, J.S., Oliver, N.H.S., Nugus, M., 2018. Microscale data to macroscale processes: a review of microcharacterization applied to mineral systems. Geological Society, London, Special Publications 453, 7–39. https://doi.org/10.1144/SP453.3

Perret, J., 2021. Répartition spatio-temporelle du système métallogénique de l'or panafricain au sein du bouclier arabo-nubien: étude multiscalaire le long de la suture de Keraf (Soudan). PhD Thesis. Université de Lorraine.

Perret, J., Eglinger, A., André-Mayer, A.-S., Aillères, L., Feneyrol, J., Hartshorne, C., Abanyin, E., Bosc, R., 2020. Subvertical, linear and progressive deformation related to gold mineralization at the Galat Sufar South deposit, Nubian Shield, NE Sudan. Journal of Structural Geology 135. https://doi.org/10.1016/j.jsg.2020.104032

Perret, J., Feneyrol, J., Eglinger, A., André-Mayer, A.-S., Berthier, C., Ennaciri, A., Bosc, R., 2021. Tectonic record and gold mineralization in the central part of the Neoproterozoic Keraf suture, Gabgaba district, NE Sudan. Journal of African Earth Sciences 181, 104248. https://doi.org/10.1016/j.jafrearsci.2021.104248

Peterson, E.C., Mavrogenes, J.A., 2014. Linking high-grade gold mineralization to earthquake-induced fault-valve processes in the Porgera gold deposit, Papua New Guinea. Geology 42, 383–386. https://doi.org/10.1130/G35286.1

Petrella, L., Thébaud, N., Fougerouse, D., Evans, K., Quadir, Z., Laflamme, C., 2020a. Colloidal gold transport: a key to high-grade gold mineralization? Mineralium Deposita 55, 1247–1254. https://doi.org/10.1007/s00126-020-00965-x

Petrella, L., Thébaud, N., LaFlamme, C., Miller, J., McFarlane, C., Occhipinti, S., Turner, S., Perazzo, S., 2020b. Contemporaneous formation of vein-hosted and stratabound gold mineralization at the world-class Dead Bullock Soak mining camp, Australia. Mineralium Deposita 55, 845–862. https://doi.org/10.1007/s00126-019-00902-7

Petrus, J.A., Chew, D.M., Leybourne, M.I., Kamber, B.S., 2017. A new approach to laser-ablation inductively-coupled-plasma mass-spectrometry (LA-ICP-MS) using the flexible map interrogation tool 'Monocle.' Chemical Geology 463, 76–93. https://doi.org/10.1016/j.chemgeo.2017.04.027

Piazolo, S., Jessell, M.W., Prior, D.J., Bons, P.D., 2004. The integration of experimental in-situ EBSD observations and numerical simulations: a novel technique of microstructural process analysis: INTEGRATION OF EXPERIMENTAL EBSD DATA AND NUMERICAL MODELLING. Journal of Microscopy 213, 273–284. https://doi.org/10.1111/j.0022-2720.2004.01304.x

Pokrovski, G.S., Borisova, A.Yu., Harrichoury, J.-C., 2008. The effect of sulfur on vapor–liquid fractionation of metals in hydrothermal systems. Earth and Planetary Science Letters 266, 345–362. https://doi.org/10.1016/j.epsl.2007.11.023

Pokrovski, G.S., Kokh, M.A., Proux, O., Hazemann, J.-L., Bazarkina, E.F., Testemale, D., Escoda, C., Boiron, M.-C., Blanchard, M., Aigouy, T., Gouy, S., de Parseval, P., Thibaut, M., 2019. The nature and partitioning of invisible gold in the pyrite-fluid system. Ore Geology Reviews 109, 545–563. https://doi.org/10.1016/j.oregeorev.2019.04.024

Prichard, H.M., Barnes, S.J., Godel, B., 2018. A mechanism for chromite growth in ophiolite complexes: evidence from 3D high-resolution X-ray computed tomography images of chromite grains in Harold's Grave chromitite in the Shetland ophiolite. Mineralogical Magazine 82, 457–470. https://doi.org/10.1180/minmag.2017.081.018

Putnis, A., 2002. Mineral replacement reactions: from macroscopic observations to microscopic mechanisms. Mineralogical Magazine 66, 689–708.

Reddy, S.M., Hough, R.M., 2013. Microstructural evolution and trace element mobility in Witwatersrand pyrite. Contributions to Mineralogy and Petrology 166, 1269–1284. https://doi.org/10.1007/s00410-013-0925-y

Reddy, S.M., Saxey, D.W., Rickard, W.D.A., Fougerouse, D., Montalvo, S.D., Verberne, R., Riessen, A., 2020. Atom Probe Tomography: Development and Application to the Geosciences. Geostandards and Geoanalytical Research 44, 5–50. https://doi.org/10.1111/ggr.12313

Rehman, H.U., Mainprice, D., Barou, F., Yamamoto, H., Okamoto, K., 2016. EBSD-measured crystal preferred orientation of eclogites from the Sanbagawa metamorphic belt, central Shikoku, SW Japan. European Journal of Mineralogy 28, 1155–1168.

Reich, M., Kesler, S.E., Utsunomiya, S., Palenik, C.S., Chryssoulis, S.L., Ewing, R.C., 2005. Solubility of gold in arsenian pyrite. Geochimica et Cosmochimica Acta 69, 2781–2796. https://doi.org/10.1016/j.gca.2005.01.011

Reich, M., Large, R., Deditius, A.P., 2017. New advances in trace element geochemistry of ore minerals and accessory phases. Ore Geology Reviews 81, 1215–1217. https://doi.org/10.1016/j.oregeorev.2016.10.020

Richard, A., Morlot, C., Créon, L., Beaudoin, N., Balistky, V.S., Pentelei, S., Dyja-Person, V., Giuliani, G., Pignatelli, I., Legros, H., Sterpenich, J., Pironon, J., 2019. Advances in 3D imaging and volumetric reconstruction of fluid and melt inclusions by high resolution X-ray computed tomography. Chemical Geology 508, 3–14. https://doi.org/10.1016/j.chemgeo.2018.06.012

Richards, J.P., Tosdal, R.M. (Eds.), 2001. Structural Controls on Ore Genesis, Reviews in Economic Geology. Society of Economic Geologists, Inc.

Ridley, J., 1993. The relations between mean rock stress and fluid flow in the crust: With reference to vein- and lode-style gold deposits. Ore Geology Reviews 8, 23–37. https://doi.org/10.1016/0169-1368(93)90026-U

Ries, A.C., Vearncombe, J.R., Price, R.C., Shackleton, R.M., 1992. Geochronology and geochemistry of the rocks associated with a late Proterozoic ophiolite in West Pokot, NW Kenya. Journal of African Earth Sciences 14, 25–35.

Robert, F., Poulsen, K.H., 2001. Vein Formation and Deformation in Greenstone Gold Deposits. In: Richards, J.P., Tosdal, R.M. (Eds.), Structural Controls on Ore Genesis, Reviews in Economic Geology. Society of Economic Geologists, Inc., 111–155.

Román, N., Reich, M., Leisen, M., Morata, D., Barra, F., Deditius, A.P., 2019. Geochemical and micro-textural fingerprints of boiling in pyrite. Geochimica et Cosmochimica Acta 246, 60–85. https://doi.org/10.1016/j.gca.2018.11.034

Rosière, C.A., Garcia, O.L., Siemes, H., Schaeben, H., 2013. Domainal fabrics of hematite in schistose, shear zone-hosted high-grade Fe ores: The product of the interplay between deformation and mineralization. Journal of Structural Geology 55, 150–166. https://doi.org/10.1016/j.jsg.2013.07.017

Rosière, C.A., Siemes, H., Quade, H., Brokmeier, H.-G., Jansen, E.M., 2001. Microstructures, textures and deformation mechanisms in hematite. Journal of Structural Geology 23, 1429–1440. https://doi.org/10.1016/S0191-8141(01)00009-8

Rowland, J.V., Rhys, D.A. (Eds.), 2020. Applied Structural Geology of Ore-Forming Hydrothermal Systems, Reviews in Economic Geology. Society of Economic Geologists, Inc.

Salvi, S., Velásquez, G., Miller, J.M., Béziat, D., Siebenaller, L., Bourassa, Y., 2016. The Pampe gold deposit (Ghana): Constraints on sulfide evolution during gold mineralization. Ore Geology Reviews 78, 673–686. https://doi.org/10.1016/j.oregeorev.2015.11.006

Sayab, M., Molnár, F., Aerden, D., Niiranen, T., Kuva, J., Välimaa, J., 2020. A succession of near-orthogonal horizontal tectonic shortenings in the Paleoproterozoic Central Lapland Greenstone Belt of Fennoscandia: constraints from the world-class Suurikuusikko gold deposit. Mineralium Deposita 55, 1605–1624. https://doi.org/10.1007/s00126-019-00910-7

Sayab, M., Suuronen, J.-P., Hölttä, P., Aerden, D., Lahtinen, R., Kallonen, A.P., 2015. High-resolution X-ray computed microtomography: A holistic approach to metamorphic fabric analyses. Geology 43, 55–58. https://doi.org/10.1130/G36250.1

Sayab, M., Suuronen, J.-P., Hölttä, P., Lahtinen, R., Karkkainen, N., Kallonen, A.P., 2014. X-ray computed micro-tomography: a holistic approach to metamorphic fabric analyses and associated mineralization. EIGHTH SYMPOSIUM ON STRUCTURE, COMPOSITION AND EVOLUTION

OF THE LITHOSPHERE IN FENNOSCANDIA PROGRAMME AND EXTENDED ABSTRACTS. 91.

Sayab, M., Suuronen, J.-P., Molnár, F., Villanova, J., Kallonen, A., O'Brien, H., Lahtinen, R., Lehtonen, M., 2016. Three-dimensional textural and quantitative analyses of orogenic gold at the nanoscale. Geology 44, 739–742. https://doi.org/10.1130/G38074.1

Schandelmeier, H., Wipfler, E., Küster, D., Sultan, M., Becker, R., Stern, R.J., Abdelsalam, M.G., 1994. Atmur-Delgo suture: A Neoproterozoic oceanic basin extending into the interior of northeast Africa. Geology 22, 563. https://doi.org/10.1130/0091-7613(1994)022<0563:ADSANO>2.3.CO;2

Sibson, R.H., 2020a. Dual-Driven Fault Failure in the Lower Seismogenic Zone. Bulletin of the Seismological Society of America 110, 850–862. https://doi.org/10.1785/0120190190

Sibson, R.H., 2020b. Preparation zones for large crustal earthquakes consequent on fault-valve action. Earth, Planets and Space 72. https://doi.org/10.1186/s40623-020-01153-x

Sibson, R.H., 2001. Seismogenic framework for hydrothermal transport and ore deposition. In: Richards, J.P., Tosdal, R.M. (Eds.), Structural Controls on Ore Genesis, Reviews in Economic Geology. Society of Economic Geologists, Inc., 25–50.

Sibson, R.H., 1990. Conditions for fault-valve behaviour. Geological Society, London, Special Publications 54, 15–28.

Soltani Dehnavi, A., 2019. Micro-Geochemical Research in Mineral Exploration, Case Study of the Massive Sulfides of the Bathurst Mining Camp, Canada. In: Doronzo, D., Schingaro, E., Armstrong-Altrin, Z., Zoheir, B. (Eds.), Petrogenesis and Exploration of the Earth's Interior, Advances in Science, Technology & Innovation (IEREK Interdisciplinary Series for Sustainable Development). Springer Berlin Heidelberg, Berlin, Heidelberg, 257–260. https://doi.org/10.1007/978-3-030-01575-6_62

Soltani Dehnavi, A., McFarlane, C.R.M., Lentz, D.R., Walker, J.A., 2018. Assessment of pyrite composition by LA-ICP-MS techniques from massive sulfide deposits of the Bathurst Mining Camp, Canada: From textural and chemical evolution to its application as a vectoring tool for the exploration of VMS deposits. Ore Geology Reviews 92, 656–671. https://doi.org/10.1016/j.oregeorev.2017.10.010

Spinks, S.C., Pearce, M.A., Liu, W., Kunzmann, M., Ryan, C.G., Moorhead, G.F., Kirkham, R., Blaikie, T., Sheldon, H.A., Schaubs, P.M., Rickard, W.D.A., 2021a. Carbonate Replacement as the Principal Ore Formation Process in the Proterozoic McArthur River (HYC) Sediment-Hosted Zn-Pb Deposit, Australia. Economic Geology 116, 693–718.

Spinks, S.C., Pearce, M.A., Le Vaillant, M., Fox, D., Tyler, I.M., Godel, B., Stromberg, J., Mead, E., White, A.J.R., 2021b. The Neoarchean Conglomerate-Hosted Gold of the West Pilbara Craton, Western Australia. Economic Geology 116, 629–650. https://doi.org/10.5382/econgeo.4790

https://doi.org/10.5382/econgeo.4793

Stern, R.J., 1994. Arc Assembly and Continental Collision in the Neoproterozoic East African Orogen: Implications for the Consolidation of Gondwanaland. Annual Review of Earth and Planetary Sciences 22, 319–351. https://doi.org/10.1146/annurev.ea.22.050194.001535

Stern, R.J., Johnson, P., 2010. Continental lithosphere of the Arabian Plate: A geologic, petrologic, and geophysical synthesis. Earth-Science Reviews 101, 29–67. https://doi.org/10.1016/j.earscirev.2010.01.002

Sung, Y.-H., Brugger, J., Ciobanu, C.L., Pring, A., Skinner, W., Nugus, M., 2009. Invisible gold in arsenian pyrite and arsenopyrite from a multistage Archaean gold deposit: Sunrise Dam, Eastern Goldfields Province, Western Australia. Mineralium Deposita 44, 765–791. https://doi.org/10.1007/s00126-009-0244-4

Suuronen, J.-P., Sayab, M., 2018. 3D nanopetrography and chemical imaging of datable zircons by synchrotron multimodal X-ray tomography. Scientific Reports 8, 1–13. https://doi.org/10.1038/s41598-018-22891-9

Tardani, D., Reich, M., Deditius, A.P., Chryssoulis, S., Sánchez-Alfaro, P., Wrage, J., Roberts, M.P., 2017. Copper–arsenic decoupling in an active geothermal system: A link between pyrite and fluid composition. Geochimica et Cosmochimica Acta 204, 179–204. https://doi.org/10.1016/j.gca.2017.01.044

Thiele, S.T., Micklethwaite, S., Bourke, P., Verrall, M., Kovesi, P., 2015. Insights into the mechanics of en-échelon sigmoidal vein formation using ultra-high resolution photogrammetry and computed tomography. Journal of Structural Geology 77, 27–44. https://doi.org/10.1016/j.jsg.2015.05.006

Tomkins, A.G., Mavrogenes, J.A., 2001. Redistribution of Gold within Arsenopyrite and Lollingite during Pro- and Retrograde Metamorphism: Application to Timing of Mineralization. Economic Geology 96, 525–534. https://doi.org/10.2113/gsecongeo.96.3.525

Upton, P., Craw, D., 2014. Modelling of structural and lithological controls on mobility of fluids and gold in orogenic belts, New Zealand. Geological Society, London, Special Publications 402, 231–253. https://doi.org/10.1144/SP402.1

Vasseur, R., Boivin, S., Lathuilière, B., Lazar, I., Durlet, C., Martindale, R.-C., Bodin, S., Elhmidi, K., 2019. Lower Jurassic corals from Morocco with skeletal structures convergent with those of Paleozoic rugosan corals. Palaeontologia Electronica 22. https://doi.org/10.26879/874

Vearncombe, J.R., 1983. A dismembered ophiolite from the Mozambique belt, west Pokot, Kenya. Journal of African Earth Sciences 1, 133–143.

Velasquez, G., Beziat, D., Salvi, S., Siebenaller, L., Borisova, A.Y., Pokrovski, G.S., De Parseval, P., 2014. Formation and Deformation of Pyrite and Implications for Gold Mineralization in the El Callao District, Venezuela. Economic Geology 109, 457–486. https://doi.org/10.2113/econgeo.109.2.457

Voisey, C.R., Willis, D., Tomkins, A.G., Wilson, C.J.L., Micklethwaite, S., Salvemini, F., Bougoure, J., Rickard, W.D.A., 2020. Aseismic Refinement of Orogenic Gold Systems. Economic Geology 115, 33–50. https://doi.org/10.5382/econgeo.4692

Vonlanthen, P., Kunze, K., Burlini, L., Grobety, B., 2006. Seismic properties of the upper mantle beneath Lanzarote (Canary Islands): model predictions based on texture measurements by EBSD. Tectonophysics 428, 65–85.

Voute, F., Hagemann, S.G., Evans, N.J., Villanes, C., 2019. Sulfur isotopes, trace element, and textural analyses of pyrite, arsenopyrite and base metal sulfides associated with gold mineralization in the Pataz-Parcoy district, Peru: implication for paragenesis, fluid source, and gold deposition mechanisms. Mineralium Deposita 54, 1077–1100. https://doi.org/10.1007/s00126-018-0857-6

Vukmanovic, Z., Barnes, S.J., Reddy, S.M., Godel, B., Fiorentini, M.L., 2013. Morphology and microstructure of chromite crystals in chromitites from the Merensky Reef (Bushveld Complex, South Africa). Contributions to Mineralogy and Petrology 165, 1031–1050. https://doi.org/10.1007/s00410-012-0846-1

Wallis, D., Parsons, A.J., Hansen, L.N., 2019. Quantifying geometrically necessary dislocations in quartz using HR-EBSD: Application to chessboard subgrain boundaries. Journal of Structural Geology 125, 235–247. https://doi.org/10.1016/j.jsg.2017.12.012

Wang, Y., Han, X., Petersen, S., Frische, M., Qiu, Z., Li, Huaiming, Li, Honglin, Wu, Z., Cui, R., 2017. Mineralogy and trace element geochemistry of sulfide minerals from the Wocan Hydrothermal Field on the slow-spreading Carlsberg Ridge, Indian Ocean. Ore Geology Reviews 84, 1–19. https://doi.org/10.1016/j.oregeorev.2016.12.020

Weatherley, D.K., Henley, R.W., 2013. Flash vaporization during earthquakes evidenced by gold deposits. Nature Geoscience 6, 294–298. https://doi.org/10.1038/ngeo1759

Wille, G., Lerouge, C., Schmidt, U., 2018. A multimodal microcharacterisation of trace-element zonation and crystallographic orientation in natural cassiterite by combining cathodoluminescence, EBSD, EPMA and contribution of confocal Raman-in-SEM imaging: MULTIMODAL CHARACTERISATION OF ZONATION IN CASSITERITE. Journal of Microscopy 270, 309–317. https://doi.org/10.1111/jmi.12684

Wilson, S.A., Ridley, W.I., Koenig, A.E., 2002. Development of sulfide calibration standards for the laser ablation inductively-coupled plasma mass spectrometry technique. Journal of Analytical Atomic Spectrometry 17, 406–409. https://doi.org/10.1039/B108787H

Winderbaum, L., Ciobanu, C.L., Cook, N.J., Paul, M., Metcalfe, A., Gilbert, S., 2012. Multivariate Analysis of an LA-ICP-MS Trace Element Dataset for Pyrite. Mathematical Geosciences 44, 823–842. https://doi.org/10.1007/s11004-012-9418-1

Wohlgemuth-Ueberwasser, C.C., Viljoen, F., Petersen, S., Vorster, C., 2015. Distribution and solubility limits of trace elements in hydrothermal black smoker sulfides: An in-situ LA-ICP-MS study. Geochimica et Cosmochimica Acta 159, 16–41. https://doi.org/10.1016/j.gca.2015.03.020

Wright, S.I., Nowell, M.M., Lindeman, S.P., Camus, P.P., De Graef, M., Jackson, M.A., 2015. Introduction and comparison of new EBSD post-processing methodologies. Ultramicroscopy 159, 81–94. https://doi.org/10.1016/j.ultramic.2015.08.001

Wu, Y.-F., Evans, K., Li, J.-W., Fougerouse, D., Large, R.R., Guagliardo, P., 2019a. Metal remobilization and ore-fluid perturbation during episodic replacement of auriferous pyrite from an epizonal orogenic gold deposit. Geochimica et Cosmochimica Acta 245, 98–117. https://doi.org/10.1016/j.gca.2018.10.031

Wu, Y.-F., Fougerouse, D., Evans, K., Reddy, S.M., Saxey, D.W., Guagliardo, P., Li, J.-W., 2019b. Gold, arsenic, and copper zoning in pyrite: A record of fluid chemistry and growth kinetics. Geology 47, 641–644. https://doi.org/10.1130/G46114.1

Xing, Y., Brugger, J., Tomkins, A., Shvarov, Y., 2019. Arsenic evolution as a tool for understanding formation of pyritic gold ores. Geology 47, 335–338. https://doi.org/10.1130/G45708.1

Yang, L., Zhao, R., Wang, Q., Liu, X., Carranza, E.J.M., 2018. Fault geometry and fluid-rock reaction: Combined controls on mineralization in the Xinli gold deposit, Jiaodong Peninsula, China. Journal of Structural Geology 111, 14–26. https://doi.org/10.1016/j.jsg.2018.03.009

Yao, X., Xia, F., Deditius, A.P., Brugger, J., Etschmann, B.E., Pearce, M.A., Pring, A., 2020. The mechanism and kinetics of the transformation from marcasite to pyrite: in situ and ex situ experiments and geological implications. Contributions to Mineralogy and Petrology 175, 27. https://doi.org/10.1007/s00410-020-1665-4

Yao, Y., Takazawa, E., Chatterjee, S., Richard, A., Morlot, C., Créon, L., Al–Busaidi, S., Michibayashi, K., Oman Drilling Project Science Team, 2020. High resolution X–ray computed tomography and scanning electron microscopy studies of multiphase solid inclusions in Oman podiform chromitite: implications for post–entrapment modification. Journal of Mineralogical and Petrological Sciences 191008. https://doi.org/10.2465/jmps.191008

Ye, L., Cook, N.J., Ciobanu, C.L., Yuping, L., Qian, Z., Tiegeng, L., Wei, G., Yulong, Y., Danyushevskiy, L., 2011. Trace and minor elements in sphalerite from base metal deposits in South China: A LA-ICPMS study. Ore Geology Reviews 39, 188–217. https://doi.org/10.1016/j.oregeorev.2011.03.001

Žák, J., Verner, K., Týcová, P., 2008. Grain-scale processes in actively deforming magma mushes: New insights from electron backscatter diffraction (EBSD) analysis of biotite schlieren in the Jizera granite, Bohemian Massif. Lithos 106, 309–322.

Zhao, H.-X., Frimmel, H.E., Jiang, S.-Y., Dai, B.-Z., 2011. LA-ICP-MS trace element analysis of pyrite from the Xiaoqinling gold district, China: Implications for ore genesis. Ore Geology Reviews 43, 142–153. https://doi.org/10.1016/j.oregeorev.2011.07.006

Supplementary Materials

Supplementary Material 1: Video file for the HRXCT-assisted 3D reconstruction of the internal structure of the oriented sample billet GS-34-07. The colour scale is the same as that of Figure 5. The video file is available from Julien Perret upon request at julien.perret15@laposte.net.

Supplementary Material 2: Extensive dataset of LA-ICP-MS trace element concentrations (in ppm) of the various pyrite generations from the Galat Sufar South gold deposit, northeastern Sudan.

ID	Py	Text.	Si	S	V	Cr	Mn	Fe	Co	Ni	Cu	Zn	Ga	As	Se	Mo	Ag	Cd	In	Sn	Sb	Te	W	Au	Tl	Pb	Bi
GS-22-10																											
z1_1	2		3680	498049	0.33	2.0	13.9	495596	139	1390	1063	10.6	0.13	38.7	5.2	1.1	0.10	0.12	0.19	<0.16	0.04	<0.42	0.29	2.7	0.09	2.5	2.6
z1_2	1b	1*	9002	488306	39.5	8.2	118	489215	36.6	9.5	282	846	1.0	102	4.6	0.45	2.3	0.98	0.07	3.8	2.0	5.5	6.5	0.52	0.16	151	1.9
z1_3	2		1212	543009	<0.34	<5.2	4.0	454041	634	160	874	2.2	0.10	57.1	<21.5	<0.26	0.15	<0.37	<0.02	<0.54	0.20	<0.84	0.71	0.18	<0.12	0.71	0.13
z1_4	1b	1*	1164	462782	5.3	<0.92	270	532462	366	23.0	993	53.2	0.32	92.0	<3.7	0.48	4.6	<0.07	<0.004	0.13	7.2	<0.15	0.28	0.12	0.33	835	5.1
z2_1	2		4182	513629	2.4	1.9	903	480409	183	259	93.7	247	0.30	72.1	5.8	0.36	0.14	0.20	0.01	0.32	0.07	<0.24	1.1	0.56	<0.007	2.8	4.1
z2_2	2		447	536948	3.8	<0.96	7.8	461839	197	41.5	312	8.0	<0.02	174	7.0	<0.07	0.19	<0.10	0.02	0.88	0.13	<0.23	<0.14	0.78	0.09	2.7	0.90
z2_3	1b	1*	3446	498653	1.0	<0.81	419	486491	182	87.8	1128	3514	0.22	52.7	4.6	1.1	6.0	3.6	0.04	<0.25	2.7	3.0	1.6	0.34	0.09	4932	19.7
z2_4	1b	1*	7321	469187	1.9	1.1	110	519766	293	19.3	1065	799	0.50	40.3	<2.3	<0.05	6.8	0.16	0.02	0.19	5.3	1.5	0.22	0.13	0.28	1014	34.4
z3_1	2		<482	521266	0.65	<1.3	246	477636	64.3	44.0	64.3	3.3	0.06	327	8.2	<0.40	0.44	<0.16	<0.04	<0.34	0.79	1.5	2.9	<0.02	<0.01	31.9	3.1
z3_2	1b	1*	1988	505019	8.0	<0.94	1032	486252	384	23.9	228	5.7	0.38	3583	5.1	0.62	3.9	0.36	<0.03	0.31	3.8	3.7	13.0	0.45	0.10	126	77.9
z3_3	2		662	527121	1.5	1.0	85.5	469297	122	89.7	15.9	3.8	<0.02	863	11.0	1.6	0.44	<0.11	<0.007	0.13	1.7	2.3	1.0	0.06	<0.008	37.0	3.0
z6_1	2		943	547733	0.80	<1.2	71.2	448240	278	63.9	36.7	1068	0.15	1414	<8.5	0.26	1.1	1.7	<0.05	<0.43	1.8	1.9	0.69	0.08	0.02	43.4	8.4
z6_2	1b	1*	968	489097	<0.32	1.2	29.8	458528	103	11.1	24.5	4.4	<0.02	197	7.0	<0.08	0.39	<0.12	<0.04	<0.30	0.15	1.1	0.08	0.09	0.07	18.3	50948
z6_3	1b	1*	3997	482307	2.0	11.0	128	512334	121	17.8	76.0	17.0	0.59	58.6	<3.0	<0.38	4.6	<0.11	0.02	<0.40	1.5	0.74	0.10	<0.01	0.22	682	4.2
z6_4	2		978	510880	1.2	<0.64	259	482226	157	154	1607	978	0.13	2523	3.4	<0.36	1.8	<0.08	0.01	0.20	8.2	2.3	0.11	0.14	0.31	126	28.0
GS-38-12																											
z1_1	4	4	280	532039	0.14	<0.60	0.90	466533	583	502	5.8	9.6	<0.06	5.8	39.1	<0.05	0.10	<0.07	<0.02	<0.15	0.10	0.30	<0.02	0.05	<0.005	0.47	<0.02
z1_2	4	4	<673	577199	0.37	<2.0	3.0	416064	538	914	144	8.9	0.31	6.9	68.5	<0.17	<0.20	<0.24	<0.02	<0.41	0.43	<0.55	<0.08	0.05	0.48	0.34	5050
z2_1	4	4	<237	531147	0.24	<0.70	<0.29	466935	447	484	907	6.1	<0.02	5.0	44.7	3.3	10.5	<0.08	0.22	0.20	1.4	<0.20	<0.03	0.38	0.02	0.69	0.06
z2_2	4	4	<391	535843	<0.35	<0.77	0.85	463063	473	186	33.7	300	1.6	14.6	49.1	0.45	0.83	0.22	<0.46	<0.20	4.5	0.50	<0.05	0.03	0.12	0.25	0.07
z3_1	4	4	<447	573885	0.45	<1.2	<0.39	419234	848	5739	214	1.8	<0.13	23.4	48.4	<0.10	<0.03	<0.15	<0.01	<0.36	0.08	1.5	<0.05	<0.01	<0.01	0.93	<0.09
z3_2	4	4	<344	555964	<0.18	<0.88	0.46	434872	398	2210	6452	2.2	0.45	19.5	45.5	<0.08	6.5	<0.11	0.03	1.1	0.53	4.2	0.05	0.66	<0.008	13.1	7.0
z3_3	4	4	<237	537662	<0.16	<0.57	0.77	459928	601	1749	6.1	1.3	<0.02	10.0	37.1	<0.06	<0.07	<0.08	0.02	<0.18	0.02	<0.79	<0.03	<0.009	<0.006	0.30	0.07
z4_1	4	4	<342	551091	3.5	<1.3	<0.53	448474	242	98.8	<7.0	3.2	<0.10	3.5	36.1	1.5	0.08	<0.15	<0.07	<0.44	0.61	1.8	<0.05	36.1	<0.01	2.3	0.04
z4_2	4	4	341	527482	0.26	<0.63	<0.29	469978	329	1633	177	2.8	0.04	5.7	46.1	<0.05	0.12	<0.08	<0.02	1.5	0.01	<0.18	<0.03	0.08	<0.005	0.72	0.03
z4_3	4	4	<415	523404	0.23	<0.62	2.1	474876	451	1075	147	2.1	<0.09	10.5	28.2	<0.32	0.32	<0.10	0.01	0.24	<0.09	<0.23	<0.16	0.14	0.02	0.68	0.21
z4_4	4	4	<254	541609	<0.36	<1.1	0.82	457238	113	780	161	6.9	0.04	7.6	71.7	0.11	1.5	<0.12	<0.07	0.16	0.39	<0.26	0.18	0.10	<0.008	3.9	<0.03
GS-36-04																											
z1_1	4	4	<394	529679	<0.19	<1.4	<0.54	465531	21.8	91.6	293	22.0	0.03	52.2	9.3	<0.09	422	0.49	0.03	0.12	20.2	367	<0.04	0.47	0.01	3482	3.8
z1_2	4	4	255	502639	0.14	2.1	8.5	496756	17.2	21.6	255	12.4	0.02	20.9	8.2	0.07	<0.05	0.10	0.02	0.12	0.15	<0.13	<0.02	0.08	0.01	1.1	0.05

Supplementary Material 2 ***(continued)***

ID	Py	Text.	Si	S	V	Cr	Mn	Fe	Co	Ni	Cu	Zn	Ga	As	Se	Mo	Ag	Cd	In	Sn	Sb	Te	W	Au	Tl	Pb	Bi
GS-22-10																											
z1_1	2		3680	498049	0.33	2.0	13.9	495596	139	1390	1063	10.6	0.13	38.7	5.2	1.1	0.10	0.12	0.19	<0.16	0.04	<0.42	0.29	2.7	0.09	2.5	2.6
z1_2	1b	1*	9002	488306	39.5	8.2	118	489215	36.6	9.5	282	846	1.0	102	4.6	0.45	2.3	0.98	0.07	3.8	2.0	5.5	6.5	0.52	0.16	151	1.9
z1_3	2		1212	543009	<0.34	<5.2	4.0	454041	634	160	874	2.2	0.10	57.1	<21.5	<0.26	0.15	<0.37	<0.02	<0.54	0.20	<0.84	0.71	0.18	<0.12	0.71	0.13
z1_4	1b	1*	1164	462782	5.3	<0.92	270	532462	366	23.0	993	53.2	0.32	92.0	<3.7	0.48	4.6	<0.07	<0.004	0.13	7.2	<0.15	0.28	0.12	0.33	835	5.1
z2_1	2		4182	513629	2.4	1.9	903	480409	183	259	93.7	247	0.30	72.1	5.8	0.36	0.14	0.20	0.01	0.32	0.07	<0.24	1.1	0.56	<0.007	2.8	4.1
z2_2	2		447	536948	3.8	<0.96	7.8	461839	197	41.5	312	8.0	<0.02	174	7.0	<0.07	0.19	<0.10	0.02	0.88	0.13	<0.23	<0.14	0.78	0.09	2.7	0.90
z2_3	1b	1*	3446	498653	1.0	<0.81	419	486491	182	87.8	1128	3514	0.22	52.7	4.6	1.1	6.0	3.6	0.04	<0.25	2.7	3.0	1.6	0.34	0.09	4932	19.7
z2_4	1b	1*	7321	469187	1.9	1.1	110	519766	293	19.3	1065	799	0.50	40.3	<2.3	<0.05	6.8	0.16	0.02	0.19	5.3	1.5	0.22	0.13	0.28	1014	34.4
z3_1	2		<482	521266	0.65	<1.3	246	477636	64.3	44.0	64.3	3.3	0.06	327	8.2	<0.40	0.44	<0.16	<0.04	<0.34	0.79	1.5	2.9	<0.02	<0.01	31.9	3.1
z3_2	1b	1*	1988	505019	8.0	<0.94	1032	486252	384	23.9	228	5.7	0.38	3583	5.1	0.62	3.9	0.36	<0.03	0.31	3.8	3.7	13.0	0.45	0.10	126	77.9
z3_3	2		662	527121	1.5	1.0	85.5	469297	122	89.7	15.9	3.8	<0.02	863	11.0	1.6	0.44	<0.11	<0.007	0.13	1.7	2.3	1.0	0.06	<0.008	37.0	3.0
z6_1	2		943	547733	0.80	<1.2	71.2	448240	278	63.9	36.7	1068	0.15	1414	<8.5	0.26	1.1	1.7	<0.05	<0.43	1.8	1.9	0.69	0.08	0.02	43.4	8.4
z6_2	1b	1*	968	489097	<0.32	1.2	29.8	458528	103	11.1	24.5	4.4	<0.02	197	7.0	<0.08	0.39	<0.12	<0.04	<0.30	0.15	1.1	0.08	0.09	0.07	18.3	50948
z6_3	1b	1*	3997	482307	2.0	11.0	128	512334	121	17.8	76.0	17.0	0.59	58.6	<3.0	<0.38	4.6	<0.11	0.02	<0.40	1.5	0.74	0.10	<0.01	0.22	682	4.2
z6_4	2		978	510880	1.2	<0.64	259	482226	157	154	1607	978	0.13	2523	3.4	<0.36	1.8	<0.08	0.01	0.20	8.2	2.3	0.11	0.14	0.31	126	28.0
GS-38-12																											
z1_1	4	4	280	532039	0.14	<0.60	0.90	466533	583	502	5.8	9.6	<0.06	5.8	39.1	<0.05	0.10	<0.07	<0.02	<0.15	0.10	0.30	<0.02	0.05	<0.005	0.47	<0.02
z1_2	4	4	<673	577199	0.37	<2.0	3.0	416064	538	914	144	8.9	0.31	6.9	68.5	<0.17	<0.20	<0.24	<0.02	<0.41	0.43	<0.55	<0.08	0.05	0.48	0.34	5050
z2_1	4	4	<237	531147	0.24	<0.70	<0.29	466935	447	484	907	6.1	<0.02	5.0	44.7	3.3	10.5	<0.08	0.22	0.20	1.4	<0.20	<0.03	0.38	0.02	0.69	0.06
z2_2	4	4	<391	535843	<0.35	<0.77	0.85	463063	473	186	33.7	300	1.6	14.6	49.1	0.45	0.83	0.22	<0.46	<0.20	4.5	0.50	<0.05	0.03	0.12	0.25	0.07
z3_1	4	4	<447	573885	0.45	<1.2	<0.39	419234	848	5739	214	1.8	<0.13	23.4	48.4	<0.10	<0.03	<0.15	<0.01	<0.36	0.08	1.5	<0.05	<0.01	<0.01	0.93	<0.09
z3_2	4	4	<344	555964	<0.18	<0.88	0.46	434872	398	2210	6452	2.2	0.45	19.5	45.5	<0.08	6.5	<0.11	0.03	1.1	0.53	4.2	0.05	0.66	<0.008	13.1	7.0
z3_3	4	4	<237	537662	<0.16	<0.57	0.77	459928	601	1749	6.1	1.3	<0.02	10.0	37.1	<0.06	<0.07	<0.08	0.02	<0.18	0.02	<0.79	<0.03	<0.009	<0.006	0.30	0.07
z4_1	4	4	<342	551091	3.5	<1.3	<0.53	448474	242	98.8	<7.0	3.2	<0.10	3.5	36.1	1.5	0.08	<0.15	<0.07	<0.44	0.61	1.8	<0.05	36.1	<0.01	2.3	0.04
z4_2	4	4	341	527482	0.26	<0.63	<0.29	469978	329	1633	177	2.8	0.04	5.7	46.1	<0.05	0.12	<0.08	<0.02	1.5	0.01	<0.18	<0.03	0.08	<0.005	0.72	0.03
z4_3	4	4	<415	523404	0.23	<0.62	2.1	474876	451	1075	147	2.1	<0.09	10.5	28.2	<0.32	0.32	<0.10	0.01	0.24	<0.09	<0.23	<0.16	0.14	0.02	0.68	0.21
z4_4	4	4	<254	541609	<0.36	<1.1	0.82	457238	113	780	161	6.9	0.04	7.6	71.7	0.11	1.5	<0.12	<0.07	0.16	0.39	<0.26	0.18	0.10	<0.008	3.9	<0.03
GS-36-04																											
z1_1	4	4	<394	529679	<0.19	<1.4	<0.54	465531	21.8	91.6	293	22.0	0.03	52.2	9.3	<0.09	422	0.49	0.03	0.12	20.2	367	<0.04	0.47	0.01	3482	3.8
z1_2	4	4	255	502639	0.14	2.1	8.5	496756	17.2	21.6	255	12.4	0.02	20.9	8.2	0.07	<0.05	0.10	0.02	0.12	0.15	<0.13	<0.02	0.08	0.01	1.1	0.05
z1_3	4	4	17819	489816	0.26	<1.3	144	490660	65.0	10.8	194	9.4	1.4	760	7.3	10.1	1.8	0.26	0.02	0.41	13.6	5.3	2.3	0.43	1.1	65.9	0.06
z1_4	4	4	16089	526535	1.3	1.1	39.7	452709	140	32.0	1323	20.9	1.3	648	<7.7	30.6	6.5	<0.12	<0.04	0.86	42.5	15.3	5.9	1.1	4.0	203	0.98

Supplementary Material 2 ***(continued)***

ID	Py	Text.	Si	S	V	Cr	Mn	Fe	Co	Ni	Cu	Zn	Ga	As	Se	Mo	Ag	Cd	In	Sn	Sb	Te	W	Au	Tl	Pb	Bi
z2_2	4	4	72482	526985	<0.70	<4.1	20.1	397370	26.8	<18.8	546	64.8	2.2	1842	<8.7	4.3	7.8	0.65	<0.03	<0.60	56.3	24.7	0.27	1.2	8.5	336	0.63
z2_3	4	4	96646	462665	<0.63	<3.6	<1.3	440389	19.2	<16.8	<22.2	4.6	<0.08	146	<7.9	1.9	6.9	<0.43	<0.03	0.65	11.3	5.5	<0.14	0.27	0.57	46.6	0.45
z2_4	4	4	33706	481366	0.17	<1.8	0.86	483519	32.3	<5.5	61.4	3.1	<0.16	373	9.3	2.1	19.7	<0.15	<0.01	0.38	12.3	19.4	0.08	0.34	0.74	872	1.0
z3_1	4	6	197	509955	0.38	4.5	0.89	488946	2.0	357	471	9.5	0.08	28.2	7.6	<0.04	0.32	0.13	0.02	0.55	0.29	0.61	0.04	0.05	0.27	12.0	0.12
z3_2	4	6	347	549858	<0.25	<0.96	1.7	449094	25.8	19.1	226	5.3	0.07	35.0	11.5	0.36	<0.17	<0.10	<0.03	<0.23	0.10	0.35	0.16	374	0.04	0.72	0.05
z3_3	4	6	258	510184	0.15	<0.81	2.5	488034	3.5	162	28.8	23.6	<0.01	32.2	7.0	0.14	1.7	0.13	<0.04	<0.20	2.3	1.6	0.05	0.27	0.03	1255	0.22
z3_4	4	6	<332	517113	<0.22	1.5	2.9	480532	13.3	53.2	190	14.9	<0.08	44.9	6.9	0.12	3.3	0.32	0.02	<0.27	20.0	4.3	<0.03	0.91	0.04	1995	0.25
z4_1	4	6	364	550306	<0.33	<1.1	3.7	448858	12.7	153	249	7.4	0.04	33.8	11.0	<0.46	0.70	0.13	<0.03	<0.27	<0.07	<0.27	0.23	0.05	<0.008	<21.1	<0.05
z4_2	4	6	250	528697	0.21	<0.58	1.8	470904	3.2	40.7	20.0	45.7	<0.01	13.0	6.8	0.26	0.68	0.53	<0.02	<0.14	0.31	0.36	<0.02	0.18	0.03	14.5	0.03
GS-55-02																											
z1_1	1b	1*	1300	503180	12.4	13.8	94.7	492358	720	330	41.7	29.8	0.23	43.3	<2.9	<0.04	1.2	<0.06	<0.004	0.74	3.5	<0.14	0.31	0.04	0.13	245	1.2
z1_2	1b	1*	5925	462924	57.3	34.6	1491	527382	261	146	176	43.0	1.8	40.7	2.9	0.08	3.5	<0.05	0.02	0.59	9.7	1.8	1.4	0.33	0.30	632	0.71
z1_3	1b	1*	3966	502766	6.7	25.5	104	489323	2554	477	142	12.6	0.34	377	15.5	<0.04	1.4	<0.06	0.01	0.15	3.0	2.8	0.07	0.32	0.08	72.6	1.6
z2_1	2		6389	530434	<0.21	<0.56	0.48	454658	7132	379	4.6	5.3	0.02	891	23.1	<0.04	0.18	<0.07	<0.004	<0.19	17.1	0.30	0.29	0.25	0.02	3.4	0.27
z2_2	1b	1*	1721	515656	7.0	8.5	91.4	479351	1217	748	116	12.0	0.19	315	7.5	<0.04	2.4	0.15	<0.02	0.37	19.1	2.0	0.04	0.24	0.08	236	4.7
z2_3	2		9133	445258	41.8	31.5	13586	520609	5206	1096	274	156	<0.57	4133	24.7	<0.43	1.1	<0.64	<0.04	<1.5	208	2.4	<0.98	0.55	0.59	153	2.7
z2_4	1b	1*	13080	477532	82.4	30.6	246	498294	415	225	858	19.5	0.71	19.4	5.1	0.17	2.9	<0.07	<0.02	3.0	5.2	0.46	0.29	0.19	0.10	264	0.27
z3_1	1b	1*	1306	490151	8.1	8.9	148	504942	785	1428	65.3	71.4	0.17	714	12.5	<0.12	1.1	<0.18	0.01	0.24	31.6	2.8	<0.01	0.27	0.21	53.6	1.7
z3_2	1b	1*	3814	491427	20.4	21.8	228	502234	687	219	203	82.6	0.79	795	10.0	<0.03	2.3	0.18	0.01	0.41	4.5	2.9	0.06	0.41	0.07	164	2.2
z3_3	1b	1*	5171	462369	43.3	28.9	201	517084	545	1221	169	19.4	0.67	128	22.5	1.4	3.5	<0.04	0.01	2.7	13.6	6.3	15.6	0.52	0.17	427	5.2
z3_4	2		518	486802	1.8	1.8	40.6	509339	365	1686	27.0	3.8	0.15	97.8	20.6	<0.02	0.27	<0.03	<0.002	0.10	0.31	0.19	<0.01	0.06	0.01	6.4	1082
z3_5	2		403	476831	1.4	1.7	45.9	515845	4205	559	954	3.0	0.07	1092	18.9	<0.09	0.62	<0.03	<0.002	<0.12	16.5	1.6	<0.01	0.20	0.01	15.3	1.3
z3_6	2		22026	469507	9.9	5.7	174	498488	6376	817	18.0	313	2.1	2145	19.7	<0.38	0.99	<0.06	<0.003	0.14	42.9	2.6	<0.02	2.1	0.08	21.4	3.0
z4_1	1b	1*	3495	519689	16.9	16.6	292	474677	753	286	210	27.0	0.70	39.3	13.8	<0.06	1.4	<0.08	0.01	0.25	2.4	<0.79	<0.03	0.15	0.03	183	0.26
z4_2	1b	1*	1525	521409	7.2	22.7	122	475464	268	187	29.2	12.8	0.42	633	3.4	<0.44	0.40	<0.07	<0.004	0.33	2.7	0.20	<0.02	0.19	0.05	109	0.47
GS-22-06																											
z1_1	1a	2	3585	555236	12.0	91.9	123	426539	120	83.7	6159	2666	0.46	4422	9.3	4.6	7.2	17.0	<0.05	0.41	9.4	4.0	1.4	1.8	0.29	772	0.36
z1_2	1a	2	7172	545436	12.6	4.8	54.7	441633	81.2	113	1736	60.4	1.0	2991	<3.8	6.5	8.6	0.95	0.05	0.17	7.5	5.9	1.3	0.57	0.09	546	0.92
z1_3	1a	2	905	562014	0.52	<1.5	12.7	429209	120	85.6	472	25.0	<0.03	6977	7.9	0.17	3.7	<0.17	<0.009	<0.35	5.3	3.6	<0.05	1.2	0.02	148	0.25
z1_4	1a	2	14140	587872	<0.30	5.8	225	386427	236	775	1743	8135	<0.05	340	<14.5	<0.17	1.9	34.9	<0.06	<0.57	3.3	1.1	<0.08	<0.03	<0.02	59.1	0.24
z2_1	1a	2	970	541919	6.7	1.7	106	447797	104	124	6845	148	0.41	1398	12.1	3.6	7.2	0.99	0.04	0.46	10.3	1.5	0.44	0.27	0.19	542	0.32
z2_2	1a	2	<361	524651	7.6	2.4	72.4	473523	122	112	551	11.4	0.07	794	6.3	1.0	4.4	<0.11	0.04	0.18	2.4	0.85	0.14	0.64	0.04	99.1	0.09
z2_3	1a	1	482	509261	0.25	<0.77	11.2	487605	29.3	76.1	2312	10.1	<0.06	48.2	3.6	0.77	9.9	<0.09	0.01	<0.25	2.4	4.8	0.06	0.36	0.04	137	0.85

Supplementary Material 2 ***(continued)***

ID	Py	Text.	Si	S	V	Cr	Mn	Fe	Co	Ni	Cu	Zn	Ga	As	Se	Mo	Ag	Cd	In	Sn	Sb	Te	W	Au	Tl	Pb	Bi
z2_4	1a	1	29350	474111	33.9	<1.5	41202	451534	213	66.6	2596	92.6	4.3	303	<8.4	0.70	1.4	0.58	0.09	2.2	2.9	<0.53	1.2	1.7	0.43	135	0.23
z2_5	1a	2	1341	539855	3.5	4.6	56.3	450475	157	107	4469	53.6	0.35	2744	8.6	2.2	6.8	0.24	<0.008	<0.29	4.7	4.5	0.10	1.2	0.19	688	0.33
z3_1	1a	1	16139	546316	15.5	25.0	269	432230	136	100	1150	28.8	0.50	436	19.3	0.41	5.7	0.68	<0.04	<0.16	4.7	4.7	0.06	0.29	0.12	3079	1.5
z4_1	1a	1	4952	571632	59.2	355	1905	416613	214	147	829	571	1.7	2218	27.2	1.4	9.0	<0.22	0.02		5.9	4.8	0.85	0.60	0.06	377	0.41
z4_2	1a	1	1081	548208	13.7	<0.72	64.1	446635	420	403	569	432	0.22	1837	18.7	0.81	4.3	0.59	0.02	<0.27	3.5	6.8	0.21	0.79	0.03	231	0.22
GS-36-05																											
z1_1	4	1	11910	490420	260	2.4	73.1	414355	64.1	9.7	480	75.1	2.4	1031	5.9	15.7	13.9	2.1	0.32	89.1	107	31.0	1391	3.6	6.4	341	0.79
z1_2	4	5	335	479603	1.3	<0.40	82.4	517107	11.5	68.2	546	102	0.39	199	4.1	0.49	23.9	1.7	0.03	0.18	102	31.8	0.62	3.0	0.26	1762	1.3
z1_3	4	5	388	501208	3.1	0.60	307	497735	7.5	23.2	75.2	4.9	0.13	60.2	3.2	0.13	0.94	<0.06	<0.004	0.20	3.7	2.1	0.04	0.49	0.06	174	0.10
z1_4	4	5	1942	502236	9.6	0.95	812	492524	8.4	39.5	146	47.9	0.87	110	<3.9	<0.44	13.5	0.31	0.02	0.78	45.1	20.8	0.44	1.8	0.15	2012	1.2
z1_5	4	5	259	522701	1.3	2.1	125	475183	17.5	<1.6	119	43.3	<0.01	748	4.8	0.09	12.3	0.20	<0.004	0.15	32.8	17.6	0.08	2.0	0.21	727	0.79
z1_6	4	5	<192	528035	0.51	<0.93	33.5	470950	15.2	2.4	193	6.4	0.03	73.5	6.2	0.47	13.3	<0.09	<0.005	<0.20	8.1	15.6	0.04	2.2	0.16	642	0.55
z1_7	4	5	1185	507158	0.87	<0.73	76.7	449087	9.8	2.8	3949	1084	0.28	1827	20.1	0.11	44.1	15.3	<0.03		1340	50.3	0.12	61.9	0.22	34069	12.1
z1_8	4	1	33641	506921	66.8	<1.4	48.4	437795	50.7	10.6	235	68.0	7.8	2189	<5.2	6.9	23.6	1.6	0.15	22.6	68.0	39.2	252	3.3	2.1	4148	1.3
z1_9	4	5	<369	550189	0.16	<0.87	1.8	449439	10.4	28.3	39.4	2.8	<0.02	10.9	7.0	0.45	1.2	<0.11	0.03	0.17	0.49	1.4	0.55	0.43	0.02	252	0.16
GS-22-07																											
z1_1	4	1	2471	555467	<0.13	<0.84	<0.37	441804	13.7	132	6.9	2.5	<0.06	46.8	43.9	0.18	2.0	<0.13	<0.007	0.28	0.10	<0.79	0.04	0.05	<0.02	4.1	1.7
z1_2	4	1	<504	561778	<0.11	<1.4	<0.49	437996	19.1	155	<6.2	<0.83	<0.03	18.5	32.3	<0.09	<0.02	<0.15	<0.10	<0.30	0.03	<0.32	<0.04	<0.02	<0.008	0.30	0.11
z1_3	4	1	<434	556387	<0.19	<0.88	<0.32	443371	9.8	140	<7.0	1.4	0.03	29.8	49.3	4.8	0.19	0.20	<0.008	<0.36	<0.02	0.42	<0.04	0.05	<0.008	1.2	0.06
z1_4	4	1	263	521424	<0.22	<0.78	0.64	476731	10.0	103	126	2.4	<0.09	44.7	27.0	0.11	10.2	<0.12	0.01	0.18	0.27	14.5	<0.03	1.1	<0.007	1236	5.7
z2_1	4	4	366	565225	0.23	2.0	4.4	430375	48.8	316	717	12.2	<0.04	18.2	29.4	<0.06	2869	<0.10	0.11	0.32	<0.03	<0.21	0.06	6.5	0.01	5.0	0.60
z2_2	4	4	569	546720	0.38	3.0	6.3	449272	49.4	82.3	3227	7.0	0.06	14.9	31.6	0.68	0.16	0.12	0.01	0.20	0.07	1.0	0.30	0.89	0.08	0.96	0.06
z2_3	4	4	<250	555891	<0.15	<0.92	1.7	443379	56.2	192	400	15.0	<0.02	26.1	35.3	<0.08	0.12	0.29	0.02	<0.18	0.09	0.59	<0.03	0.17	0.03	0.47	<0.03
z2_4	4	4	320	560748	0.21	2.5	<0.46	436793	80.1	65.8	928	73.4	<0.02	13.0	34.6	3.1	1.9	0.25	0.01	0.23	0.35	1.6	<0.03	0.52	0.01	928	5.1
z2_6	4	4	<192	563473	<0.10	<0.96	4.6	435906	44.9	37.6	462	10.9	<0.02	19.4	35.3	<0.05	1.3	0.22	0.01	0.13	<0.01	<0.19	0.11	2.2	<0.005	1.2	0.10
z3_1	4	4	283	557532	0.17	<0.94	0.45	441937	35.6	29.4	55.8	5.0	<0.08	18.2	27.4	0.28	<0.07	<0.11	0.01	<0.20	0.26	0.45	<0.03	70.8	0.02	1.5	0.34
z3_2	4	4	<406	556384	<0.13	<0.95	0.86	440435	57.5	66.6	424	4.8	<0.02	51.9	45.9	<0.42	3.0	0.18	0.01	<0.25	<0.10	2.3	<0.03	0.22	0.02	2509	14.5
z3_3	4	4	1016	547981	0.94	<0.94	2.1	450676	40.5	154	40.1	4.7	0.15	17.0	28.7	<0.29	0.36	<0.12	<0.006	<0.24	0.13	0.66	0.05	0.15	0.01	16.2	0.75
z3_4	4	4	<225	561529	<0.25	<0.75	0.31	437732	84.1	72.5	342	150	0.03	41.7	40.4	<0.06	2.9	<0.10	<0.005	<0.14	<0.18	0.40	<0.03	0.21	<0.006	0.75	0.26
z3_5	4	4	5569	521072	4.7	<1.1	7.5	473008	48.5	34.3	8.0	33.6	1.2	24.7	29.8	<0.06	0.98	<0.11	<0.02	0.53	0.22	1.6	0.54	0.12	0.11	50.4	0.48
z3_6	4	4	<534	574005	<0.22	<1.8	<0.60	424876	76.5	64.7	34.7	882	<0.13	19.3	28.7	0.67	0.20	6.2	<0.04	0.07	<0.02	0.68	<0.05	<0.08	<0.01	4.0	0.55
GS-38-08																											
z1_1	1b	3	496	536278	<0.10	<0.67	0.33	462539	402	196	15.4	5.4	<0.01	49.7	<4.2	<0.21	0.62	<0.08	<0.004	0.19	0.18	<0.17	0.09	<0.04	<0.005	12.7	0.12

Supplementary Material 2 ***(continued)***

ID	Py	Text.	Si	S	V	Cr	Mn	Fe	Co	Ni	Cu	Zn	Ga	As	Se	Mo	Ag	Cd	In	Sn	Sb	Te	W	Au	Tl	Pb	Bi
z1_2	1b	3	<465	560205	<0.20	<1.4	1.3	439054	140	473	67.8	2.4	<0.03	44.3	7.5	<0.47	0.43	<0.16	0.05	<0.13	0.05	0.99	<0.16	0.07	0.02	3.3	0.06
z1_3	1b	3	1791	544267	<0.16	<1.3	179	452727	62.3	510	49.8	56.7	<0.03	56.7	7.1	<0.09	4.6	0.33	<0.03	<0.33	20.9	5.7	<0.04	0.26	<0.08	258	1.8
z1_4	1b	3	<318	516828	0.13	<0.92	<0.29	482429	242	436	<3.1	3.5	<0.08	36.4	7.8	<0.28	1.4	<0.11	0.01	<0.10	0.32	1.3	0.04	0.47	<0.06	5.4	0.25
z1_5	1b	3	659	499364	0.93	1.0	43.4	499364	71.6	28.9	81.1	2.4	<0.06	281	<1.9	<0.05	5.0	<0.09	<0.005	<0.14	57.9	1.9	<0.02	0.25	2.7	30.7	0.09
z1_6	1b	3	28081	532539	<0.15	<0.95	<0.66	438266	94.3	320	13.7	532	<0.03	64.5	<13.0	<0.47	8.1	5.2	<0.04	<0.38	1.6	8.7	<0.05	0.90	0.02	62.2	0.78
z1_7	1b	3	<353	523476	0.16	<0.92	0.52	475713	42.0	536	13.3	3.1	<0.02	60.6	9.6	<0.33	41.1	<0.14	<0.03	<0.33	1.5	55.4	<0.04	6.8	<0.007	36.6	0.61
z2_1	1b	1	1527	550328	18.5	7.6	0.77	434737	712	305	131	3.6	0.03	2181	4.0	3.9	2.4	0.14	0.01	0.55	57.4	3.3	32.7	0.88	1.1	45.1	0.11
z2_2	2		12410	544672	26.2	7.3	4.0	441254	579	400	15.0	24.8	1.3	207	8.6	0.27	0.68	<0.10	0.01	0.30	2.5	1.2	4.3	0.03	0.20	12.5	0.15
z2_4	2		16348	554161	1.1	<1.4	1.5	428551	317	490	17.5	10.0	0.32	80.4	3.1	<0.09	0.37	<0.16	0.01	<0.31	3.3	0.50	<0.04	0.17	0.16	7.4	0.05
z2_5	2		41298	547775	126	32.6	11.2	409300	321	437	24.5	45.6	6.0	33.9	<9.7	<0.83	0.61	<0.29	<0.02	0.55	0.76	0.99	2.6	0.16	0.27	6.7	0.33
z2_6	1b	1*	1416	597368	2.1	<2.8	<0.84	397095	90.9	79.4	88.6	1116	0.13	2302	<13.8	<0.17	14.8	12.4	0.02	<0.40	93.2	70.2	<0.08	3.8	19.3	218	4.2
z2_7	2		<704	608066	<0.26	<2.3	<0.72	391219	193	467	<6.6	2.3	<0.04	51.0	<11.2	<0.15	0.17	<0.25	<0.01	<0.35	0.12	<0.51	<0.06	0.18	<0.01	0.76	<0.06
z3_1	1b	3	<476	577748	<0.27	<1.4	<0.42	421394	143	487	36.2	3.5	<0.10	139	5.2	<0.09	2.0	<0.16	0.09	0.22	1.1	4.8	<0.04	0.72	0.02	34.1	0.43
z3_10	1b	3	2070	552498	6.5	1.2	3.3	443770	459	197	24.2	757	0.23	95.0	<6.5	<0.06	14.2	5.6	0.01	0.28	10.5	5.7	0.04	0.49	0.19	60.4	0.66
z3_2	1b	3	864	567769	7.8	2.1	2.2	430039	33.9	344	227	30.0	0.28	61.5	5.6	<0.05	0.34	<0.10	<0.04	0.21	0.97	1.3	2.6	2.2	0.01	13.8	0.24
z3_3	1b	3	431	556544	0.51	0.86	0.65	441426	249	235	530	6.5	<0.02	431	<5.4	<0.07	8.9	<0.12	<0.02	<0.22	66.3	11.1	0.07	1.8	3.3	43.9	0.39
z3_4	1b	3	<246	537394	<0.13	<0.65	2.1	460808	302	354	909	84.4	<0.01	96.7	8.6	0.35	2.1	1.2	0.03	0.16	15.6	3.2	0.21	0.15	<0.004	14.3	0.28
z3_5	1b	3	<261	578466	<0.15	1.6	0.47	419143	109	490	711	376	<0.02	482	6.7	0.11	5.6	6.7	<0.03	0.16	128	3.5	<0.03	0.40	0.09	62.9	0.97
z3_6	1b	3	<279	572158	0.74	1.1	1.2	426861	131	217	82.9	5.0	0.03	391	5.0	0.10	6.2	<0.11	0.05	<0.17	95.2	1.5	<0.03	0.49	3.3	32.1	0.18
z3_7	1b	3	<225	571654	0.21	<0.68	<0.21	427533	330	238	20.1	6.9	<0.02	106	<16.9	0.14	0.58	<0.10	<0.005	<0.25	4.8	1.5	0.39	2.4	0.11	23.3	0.71
z3_8	1b	3	1168	529067	9.9	6.0	1108	463270	181	158	779	497	0.15	2404	<4.3	<0.21	31.6	3.9	0.05	0.13	725	12.0	1.2	1.4	23.2	293	2.2
z3_9	1b	3	8472	562465	6.5	4.7	6.6	426216	456	291	183	44.5	0.43	118	7.1	<0.08	4.4	<0.53	<0.007	<0.24	12.3	5.5	0.78	0.12	0.31	1659	4.7
GS-34-05																											
z1_1	1b	2	320	529787	0.19	2.7	1.9	468622	120	668	414	11.1	0.07	4.7	31.1	0.38	0.88	<0.09	0.04	<0.32	0.12	0.48	0.08	1.4	0.17	8.5	0.16
z1_2	1b	2	406	531283	0.37	3.0	15.1	465634	177	1083	1015	35.9	0.04	183	17.5	<0.05	46.7	<0.58	0.03	<0.24	1.9	60.2	0.53	4.8	0.02	22.6	0.62
z1_3	1b	2	616	527955	7.3	5.2	3.4	466316	384	491	697	8.6	0.11	27.8	40.2	0.29	8.7	0.11	0.01	<0.20	2.4	48.2	9.2	3.8	0.05	55.4	2.7
z3_1	1b	2	2042	499204	3.7	3.0	0.92	496142	503	351	1429	13.3	<0.51	88.8	25.6	<0.09	6.8	<0.11	<0.01	<0.20	0.95	15.3	2.1	0.14	0.04	17.7	0.17
z3_2	1b	2	1246	520319	19.5	55.9	30.5	477100	492	166	169	6.6	0.81	99.1	30.9	<0.07	8.6	<0.08	<0.008	<0.15	6.3	55.1	0.35	5.6	0.14	173	1.0
z6_1	1b	2	1356	548146	7.2	5.7	11.4	447862	705	509	558	6.7	0.14	46.8	25.1	<0.11	34.2	<0.14	<0.04	0.24	1.7	41.0	14.5	6.2	<0.01	29.7	1.3
z6_2	1b	2	21320	546010	172	88.7	9.9	427708	636	476	572	125	8.8	533	26.7	0.42	793	0.53	0.08	0.68	8.1	611	13.7	26.0	0.30	49.4	3.7
z6_3	1b	2	2738	539878	15.6	9.4	3.2	454461	856	265	209	11.2	0.67	70.1	23.3	2.4	209	0.45	0.04	<0.92	2.4	238	12.8	10.3	0.03	119	2.3
GS-22-08																											
z1_1	2		15890	542077	7.7	4.9	3.5	440501	518	754	6.0	15.3	0.61	152	6.6	<0.09	0.10	0.21	<0.01	<0.28	0.18	0.50	0.20	0.22	0.03	6.7	0.21

Supplementary Material 2 ***(continued)***

ID	Py	Text.	Si	S	V	Cr	Mn	Fe	Co	Ni	Cu	Zn	Ga	As	Se	Mo	Ag	Cd	In	Sn	Sb	Te	W	Au	Tl	Pb	Bi
z1_2	1b	1*	6609	513629	50.7	137	589	474346	1326	166	815	64.8	1.7	248	10.8	0.16	2.7	0.78	0.04	<0.55	7.1	8.2	1.7	0.86	0.21	372	8.0
z1_3	2		376	536646	<0.15	<2.0	<0.45	461620	263	875	60.4	1.8	<0.03	143	9.7	<0.10	0.21	<0.14	<0.01	<0.25	0.06	1.1	<0.05	0.36	<0.01	1.7	0.23
z1_4	1b	1*	7906	510677	59.3	118	665	474385	1624	153	415	29.4	1.7	238	5.3	<0.07	1.6	<0.08	<0.03	0.46	8.3	4.3	11.6	0.39	0.35	269	2.2
z1_5	2		414	548642	<0.27	1.2	2.4	448269	628	1462	312	3.8	<0.03	252	7.1	<0.09	0.16	<0.12	<0.01	<0.57	0.09	0.49	<0.04	0.09	0.04	1.7	0.04
z1_6	1b	1*	7508	524839	45.1	191	414	461769	1877	271	788	39.0	1.8	228	4.9	<0.06	1.8	<0.07	0.01	<0.30	8.5	16.3	2.3	0.47	0.21	311	3.5
z5_1	2		288	532330	0.14	<0.71	0.67	465189	144	1623	208	4.8	<0.02	203	7.4	0.10	0.28	<0.06	<0.05	<0.12	0.17	0.30	0.18	0.34	0.05	1.1	0.14
z5_2	1b	1*	5198	530599	30.3	35.7	1213	454799	1343	240	128	28.2	1.3	1224	7.1	<0.14	1.2	<0.17	0.02	<0.45	4.4	1.6	14.0	260	0.13	91.0	0.83
z5_3	2		1810	545926	<0.26	<1.0	0.87	450651	576	511	295	3.2	<0.03	207	6.2	<0.77	0.55	<0.11	<0.04	<0.18	0.35	0.41	0.13	0.49	<0.008	9.9	0.62
z5_4	1b	1*	2244	510603	34.5	48.9	14.2	437780	1380	568	85.5	18.5	0.25	204	7.8	1.2	1.9	<0.08	<0.03	1.1	12.0	8.1	52.5	0.44	0.05	77.1	2.2
z5_5	2		322	555035	0.16	<0.93	2.0	443351	425	745	3.0	2.7	0.08	91.7	7.4	<0.07	0.12	<0.08	0.06	<0.18	<0.07	<0.22	0.05	0.26	0.06	1.1	0.03
z5_6	1b	1*	9107	530100	60.7	13.8	350	457707	186	122	91.9	21.8	1.9	108	<2.9	<0.06	1.5	<0.08	0.03	0.22	6.3	5.1	4.5	0.25	0.16	98.9	0.81
GS-38-05																											
z2_1	2		2458	565909	<0.45	<1.3	4.0	430441	25.0	56.6	371	2.7	0.25	705	<9.1	0.13	0.39	0.69	<0.05	<0.28	1.6	0.42	<0.21	0.31	<0.04	23.7	0.07
z2_2	1b	2*	1522	554636	1.2	3.8	17.8	433754	37.7	86.0	320	8.2	0.08	9493	<4.3	<0.07	3.8	0.60	0.03	0.50	5.4	3.8	<0.40	9.5	<0.05	93.2	0.15
z2_3	2		772	566914	1.9	3.1	2.3	432099	22.1	23.0	<4.5	<4.6	0.06	144	10.5	<1.1	0.04	<0.16	0.04	<0.39	0.28	<0.43	<0.06	0.10	<0.01	6.2	0.01
z2_4	1b	2*	2661	571612	<0.20	<2.5	<0.46	422345	10.5	25.5	35.9	<5.3	<0.05	3263	3.7	<1.3	1.4	<0.19	<0.02	<0.45	3.3	<0.49	<0.07	0.64	0.10	37.7	0.04
z8_1	1b	2*	2393	566653	4.8	13.8	4.4	419648	40.2	59.0	137	137	0.41	3333	<4.1	4.0	33.3	0.74	<0.04	<0.26	17.3	6.2	3.4	1.5	0.22	7436	0.51
z8_2	2		9027	557829	1.9	6.1	4.4	431681	90.3	145	10.8	3.6	<0.17	1134	<8.6	2.4	0.75	<0.16	<0.06	<0.70	1.3	0.89	0.39	0.30	0.01	60.2	0.06
z8_3	2		8510	586036	0.98	3.9	13.9	396493	47.4	158	174	90.9	0.09	6576	2.1	0.86	10.8	<0.56	<0.05	<0.38	18.4	4.0	0.69	3.2	0.09	1847	0.13
z8_4	2		362	549685	0.06	<0.91	0.40	448507	42.3	88.3	400	106	0.03	748	1.4	0.10	3.3	0.80	0.23	0.29	4.8	2.1	<0.03	2.7	<0.005	44.5	0.19

Concentrations are in ppm.

*Pyrite-bearing structures and pyrite textures are: 1 = disseminated; 2 = dismembered veinlet; 3 = pyrite-dominated veinlet; 4 = polymetallic breccia; 5 = pyrite stringer; 6 = quartz-dominated breccia; * = altered.*